Towards Forecasting Capability in Solar Energetic Particle Modeling

by

Dmitry Borovikov

A dissertation submitted in partial fulfillment
of the requirements for the degree of
Doctor of Philosophy
(Atmospheric, Oceanic and Space Sciences and Scientific Computing)
in The University of Michigan
2017

Doctoral Committee:

Professor Tamas I. Gombosi, Co-Chair
Research Scientist Igor V. Sokolov, Co-Chair
Professor Quentin F. Stout
Research Associate Professor Ward B. Manchester IV

Dmitry Borovikov

dborovik@umich.edu

ORCID iD: 0000-0002-0151-7437

TABLE OF CONTENTS

LIST OF FIGURES

Figure

LIST OF ABBREVIATIONS

AMPS Adaptive Mesh Particle Simulator

AMR Adaptive Mesh Refined

AR Active Region

ARMS Adaptively Refined MHD Solver

AU Astronomical Unit

AWSoM Alfvén Wave Turbulence based Solar atmosphere Model

AWSoM-R Alfvén Wave Turbulence based Solar atmosphere Model in Real time

BATS-R-US Block-Adaptive-Tree Solar-wind Roe-type Upwind Scheme

CME Coronal Mass Ejection

DSA Diffusive Shock Acceleration

EEGGL Eruptive Event Generator based on Gibson-Low magnetic configuration

IH Inner Heliosphere

IMF Interplanetary Magnetic Field

M-FLAMPA Multiple-Field-Line-Advection Model for Particle Acceleration

MHD Magnetohydrodynamic

SC Solar Corona

SEP Solar Energetic Particle

SWMF Space Weather Modeling Framework

ABSTRACT

Solar Energetic Particles (SEPs) are an important aspect of space weather. SEP events posses a high destructive potential, since they may cause disruptions of communication systems on Earth and be fatal to crew members onboard spacecrafts and, in extreme cases, harmful to people onboard high altitude flights. However, currently the research community lacks efficient tools to predict such hazardous threat and its potential impacts. Such a tool is a first step for humanity to improve its preparedness for SEP events and ultimately to be able to mitigate their effects. The main goal of this project is to develop a computational tool that will have the forecasting capability and can be the basis for operational system that will provide live information on the current potential threats posed by SEP based on the observations of the Sun. The complexity of the problem is reflected in the level of sophistication of the product of development. The tool comprises several numerical models, which are designed to simulate different physical aspects of SEPs. The background conditions in the interplanetary medium, the magnetic field in particular, play a defining role in the transport and acceleration of SEPs, and are simulated with the state-of-the-art MHD solver, Block-Adaptive-Tree Solar-wind Roe-type Upwind Scheme (BATS-R-US). The newly developed particle code, Multiple-Field-Line-Advection Model for Particle Acceleration (M-FLAMPA), simulates the actual transport and acceleration of SEPs and is coupled to the MHD code. The special property of SEPs, the tendency to follow magnetic lines of force, is fully taken advantage of in the computational model, which substitutes a complicated 3-D model with a multitude of 1-D models. This approach significantly simplifies computations and improves the time performance of the overall model. Another aspect of SEP physics, the production of energetic particles during

solar flares is also explored.

CHAPTER I

Introduction

1.1 Overview

For our technologically advanced civilization, space plays an increasingly important role. The idea of interplanetary travel and even establishing colonies on Moon and Mars slowly but steadily transitions from science fiction into the realm of plausibility. However fascinating as the perspectives could sound, our ability to predict dangers that we may encounter along the way needs to be significantly improved. The dangers themselves, however, are not unknown to us. One of them comes from our Sun in the form of SEPs. Triggered by extreme solar events, SEP fluxes may reach values that are damaging to the electronics onboard spacecraft and potentially fatal to the crews. Precedents of SEPs events of such ominous scale have been recorded in the recent history.

During the Apollo program, at a time when astronauts repeatedly visited the Moon, a huge SEP event accompanied the major August 1972 solar storm. The integrated SEP flux produced by this storm could have been fatal for Moon walking astronauts since the radiation dose from energetic particles penetrating their spacesuits would have exceeded the lethal level ($\sim$400 rems in a short period of time). Luckily, during this event the Apollo16 astronauts were already safely back on the Earth, while the crew of Apollo 17 was still preparing for their mission. An SEP

event during the historic "giant leap for mankind" lunar landing could have been fatal. NASA, and the entire world, was lucky that the Sun "cooperated" with this endeavor.

However, when planning interplanetary human missions, one cannot rely on luck. A mission to Mars and back will take several years, and there is a significant risk to have one or more extreme SEP events that "may expose the crew to doses that lead to acute radiation effects." The fact that we cannot predict SEP events makes a human mission to Mars a "high-risk adventure" (*Hellweg and Baumstark-Khan*, 2007; *Jäkel*, 2004).

Let us come back to the Earth and consider the harmful effects of SEP events on assets at low Earth orbit (LEO). The terrestrial magnetic field provides some shielding for the International Space Station (ISS) as well as the majority of unmanned missions from SEPs. However, extreme SEP events, such as that of 20 January 2005, have hard energy spectra and they are particularly rich in hundreds of MeV to several GeV protons. A significant fraction of a flux of high-energy particles, which have a high penetrating capability, can reach LEO, thus producing significant radiation hazard for human spaceflight. Comparing with the direct threat to human life and health, the SEP effect on unmanned satellites on LEO may seem to be not so important. However, the possible loss of entire satellites with their expensive computers, sensors, and other elements of electronics is not limited to the cost (typically hundreds of millions of dollars) of the satellite itself. Many satellites are integrated into vitally important systems of defense, rescue, navigation, communication, weather, so the disruption of such system may have catastrophic consequences.

Even closer to the Earth is the ozone (O_3) layer in the stratosphere. This layer protects the Earth against harmful solar UV and EUV emissions, and the depletion of the ozone layer would increase the number of skin cancer cases in the human population. The higher energy SEPs can reach the stratosphere. In particular, the SEP

event in August 1972 reduced the ozone concentration near the North geomagnetic pole by $> 20\%$, this reduction lasted for $\sim$20 days, i.e. well after the end of the SEP event (*Heath et al.*, 1977). The reason is that very large SEP events can increase the ionization degree in the stratosphere by more than a factor of 100 over quiet times (see *Makhmutov et al.*, 2009). The increased ionization initiates a chain of chemical reactions that produce so-called "odd nitrogen" molecules, (e.g. NO, which cannot be created from even nitrogen molecule, N_2). Molecules like NO catalyze the ozone decay, and each odd nitrogen molecule can "kill" millions of O_3 molecules.

Among other threats, SEP events and their increased radiation hazard make the flight routes over the North Pole more challenging, because of the increased risk of radiation exposure and interference with communication in high frequency range (HF) (*Morris*, 2007).

We see that some effects of extreme SEP events are only important at higher latitudes near the geomagnetic poles, approximately in the same regions where auroras are often observed. However, during relatively infrequent but more powerful events, such as the Carrington event of 1859, the aurora had been observed as far from geomagnetic poles as at Hawaii, Miami or Jerusalem (*Cliver*, 2006; *Green et al.*, 2006; *Green and Boardsen*, 2006; *Shea et al.*, 2006; *Shea and Smart*, 2006). For such events, the area in which the ozone layer is depleted may also extend well beyond the polar region and this would last longer. Air traffic may be interrupted all over the world. We know that such unique events may happen, for example, *Riley* (2012) estimates that there is a 12% probability of a super storm (of the order of the Carrington event of 1859) occurring within the next decade. But we do not know, how it would affect the modern technology.

These are the main reasons why SEP events are considered as one of the most important aspects of space weather. This explains the need for predictive technology that is capable of providing a reliable quantitative forecast of SEP events and their

impacts.

1.2 Outline

The goal of the research is to develop a computational framework embracing several coupled physical and numerical models, which could quantitatively simulate the SEP production during the gradual events with ultimately achieving a capability to predict the SEP flux and spectrum (or, at least, the probability of dangerously high flux and related radiation hazard).

We provide the review of SEP production (see Chapter II) as well as the basic physical processes that govern the transport and acceleration of SEP from the perspective of dynamics of a single particle (Chapter III) and of the macroscopic kinetic evolution of the entire SEP particle population (Chapter IV). We discuss the dependence of SEP evolution on the ambient plasma parameters and magnetic field. In particular, we emphasize particles' tendency to follow magnetic field lines, particle acceleration at a shock wave front and scattering on irregularities of the magnetic field. The relevant models are reviewed.

To perform an accurate forecasting simulation, one needs to simulate a full 3-D structure of the interplanetary magnetic field prior to Coronal Mass Ejection (CME), which determines the magnetic connectivity and allows simulating the SEP transport along the magnetic field lines toward 1 AU. One also needs to know the 3-D distribution of the solar wind parameters. This ambient solution affects the CME and shock wave travel time to 1 AU, hence, the time of SEP enhancement in the course of the shock wave passage. The pre-eruptive structure of the SC should also be known, since it controls the possibility for the shock wave formation at small heliocentric distances, which results in efficient Diffusive Shock Acceleration (DSA), as well as the magnetic connectivity of the AR, at which CME originates, to the upper SC. To simulate the ambient solution in the SC and Inner Heliosphere (IH), the Alfvén Wave Turbulence

based Solar atmosphere Model (AWSoM) is used. In order to simulate an ongoing CME and to reach the predictive capability, the model should run faster than the Real-time, therefore, the Alfvén Wave Turbulence based Solar atmosphere Model in Real time (AWSoM-R) model with this feature is utilized. The CME-driven shock wave should be simulated starting from the lower altitude. Relevant models and tools are described in Chapter V.

As before, computational efficiency is the major requirement. One of the ways to meet it is to reduce a global 3-D problem of particle propagation and acceleration to a set of independent 1-D problems along individual magnetic field lines. Our new computational technology, M-FLAMPA, which is the primary product of this dissertation project, performs such reduction and is discussed together with other computational models in Chapter VI.

Additionally, we present results of the simulation of SEP production during solar flares in Chapter VII.

CHAPTER II

SEP Production

2.1 Overview

The impact that SEP events have at Earth is defined by such parameters as composition, energy spectrum, duration of event, etc. Although all of those can experience significant changes over the time and distance that particles need to travel, the state of SEP population at the onset of the event has strong influence on its subsequent evolution. Therefore, the mechanism of SEP production plays a key role in shaping the event and its effects.

First observations of "solar cosmic rays", as SEP were referred to at the time, dated back to 1942 (see *Forbush*, 1946) and were immediately linked to solar flares that preceded these particles events. This hypothesized connection was further strengthened by observations that followed, and solar flares were considered to be the primary source of SEPs (*Meyer et al.*, 1956). As number of observed events increased, it became apparent that features of events, such as the aforementioned composition, duration, etc., exhibit a wide variability (*Wild et al.*, 1963). The discovery of CMEs prompted formulation of a new hypothesis that SEPs are produced by interplanetary shocks that often accompany flares rather than by flares themselves (*Kahler et al.*, 1978; *Gosling*, 1993).

The debate ultimately resulted in the commonly adopted paradigm (e.g. *Ruffolo*

et al., 1998; *Reames*, 1999, 2002; *Cliver*, 2009) that states that SEP events can be divided into two distinct classes: (1) impulsive, and (2) gradual events. The former are caused by solar flares, while the latter are associated with CMEs. Gradual events are prolonged in time and more extended in longitudinal range compared to the impulsive events. Also, SEP composition was found to be a good indicator of nature of events (*Cane et al.*, 2006), e.g. flare associated events have Fe/O abundance of $\sim$1 and are electron-rich, while those associated with CME-driven shocks have Fe/O abundance of $\sim$0.1 and are proton-rich.

It should be noted that the pattern above was originally discovered for particles of energies that are limited by $<$30 MeV. Such particles are easily detected by instruments outside the Earth's magnetosphere. For this reason, many models focus on this particular part of the particle population. However, the particles that pose the largest threat are those that exceed this energy, and for them the aforementioned pattern is much less clear. Based on compositional and other data, many large SEP events show signatures of both gradual and impulsive events and, thus, don't fully agree with the simple bi-modal paradigm (e.g. *Cohen et al.*, 1999; *Mazur et al.*, 1999). *Cohen et al.* (2008) explain the discrepancy by simultaneous but separate acting processes of flare and shock acceleration, while *Tylka et al.* (2005) suggest that there is no true separation of events into two distinct categories: seed suprathermal particle population originates in flares and is then accelerated by CME-driven interplanetary shocks. In both of these explanations, signatures of both types of events naturally arise in large SEP events. These events are frequently associated with so-called Ground Level Events (GLEs), as most energetic particles have the potential to penetrate Earth's magnetosphere and ionosphere (*Shea and Smart*, 1990, 1994, 2012; *Gopalswamy et al.*, 2014). Relevant data are provided by measurements performed with neutron monitors. Analysis of properties of GLEs and those of associated solar flares and CMEs (e.g. *Kahler et al.*, 2012; *Gopalswamy et al.*, 2012) confirms that

SEP production is likely to involve both types of events. Further observations, e.g. by AMS-02 instrument (*Aguilar et al.*, 2015), will provide valuable insights into this problem.

2.2 Production of SEP at Flare Sites

Particle acceleration during solar flare events has received great attention in recent years, in particular, production of energetic electrons, which will be the main focus of the discussion of SEP production at flare sites. A significant portion of energy released during a flare is transformed into hard X- or γ-radiation as accelerated electrons interact with a dense background (*Hudson and Ryan*, 1995; *Vilmer et al.*, 2011; *White et al.*, 2011; *Kontar et al.*, 2011). As this type of radiation is a signature of Bremsstrahlung, these observations are a clear indication of a highly energetic electron population present in the system. Radiation spectra registered by various spacecrafts allow us to infer the electrons' distribution function. A well-known power law, $f(E) \propto E^{-1.5}$, is commonly found throughout many data sets (*Holman et al.*, 2003), implying that an efficient process drives electron acceleration during solar flare events.

During a solar flare, magnetic free energy is released via reconnection and energy is transferred from magnetic field to plasma.

Although the existence of such process is undoubted, its nature is poorly understood. The primary difficulty is the lack of in situ observations of the acceleration regions. The electron population may evolve and change properties before it emits bremsstrahlung, and therefore affecting the observed radiation spectrum (*Agueda et al.*, 2009; *Holman et al.*, 2011). Researchers are faced with a problem of distinguishing which observed features are caused by the acceleration process rather than acquired later.

Several candidates for SEP acceleration mechanism at flare sites have been sug-

gested. One of the models, which is similar to the SEP acceleration by CMEs (see below in the present Chapter), states that particles are accelerated at the termination shocks of flares. These standing fast magneto-sonic shocks are formed due to the plasma outflow from the reconnection sites (reconnection jet) encountering arcades of closed loop of magnetic field. Such structures are commonly observed in Magneto-hydrodynamic (MHD) simulations of solar flares (e.g. *Forbes*, 1986; *Workman et al.*, 2011). Since these termination shocks serve as magnetic mirrors, a significant fraction of particles reflect from them and gain energy in the process. The phenomenon is known as first order Fermi acceleration (*Fermi*, 1949), it is discussed in more details in Chapter III. Fermi acceleration is frequently referenced in discussions of rapidly moving interplanetary shocks, so particle's energy would seem to remain the same on reflection from a standing shock. However, it should be taken into account that the latter statement holds in the so-called de Hoffmann-Teller frame of reference (*de Hoffmann and Teller*, 1950), where vectors of magnetic field and plasma velocity are parallel. This frame moves perpendicular to the shock's normal, therefore, a particle that reflects from the shock is likely to gain additional momentum in that direction. Exceptions are the particles with very oblique incident angles and moving towards de Hoffmann-Teller frame. On the micro level, a particle spends some amount of time within the shock front, while moving along the direction of electric field. For this reason, this particular type of acceleration if often called the *drift shock acceleration* (*Ball and Melrose*, 2001; *Mann et al.*, 2009). As demonstrated in numerical simulations (see e.g. *Guo and Giacalone*, 2012), both protons and electrons are efficiently accelerated with thermal electrons being accelerated up to tens of keV provided that a sufficiently strong magnetic turbulence assists in the process. Although the mechanism may not fully explain extreme events, it fits in the hypothesis that SEP particles originate at flares sites and then further re-accelerated by CMEs (*Petrosian*, 2016).

Drake et al. (2006a) proposed a mechanism that accounts for a frequently observed

feature: high variability in time of the radiation spectra (*Holman et al.*, 2011). This is likely an indication of the acceleration mechanism being intermittent in nature. The model is based on the dynamics of plasmoids formed in flare current sheets and the response of the electrons moving within them. Plasmoids, often referred to as magnetic islands, are flux ropes, formed between pairs of reconnection regions (X-points, X-lines, or nulls), that subsequently move, contract, and possibly coalesce within the sheet. On the kinetic scale, plasmoid electrons experience Fermi acceleration due to the contraction of the field lines on which they reside, increasing their energy of motion parallel to the magnetic field. In regions where the local magnetic field strength rises with time, the energy of electron motion perpendicular to the field increases due to betatron acceleration. Both effects are discussed in Chapter III.

The island-contraction mechanism for electron acceleration has been extensively studied in recent years. In Chapter VII, we present an extension of the study by *Guidoni et al.* (2016), which utilized the physical properties of an MHD simulation of a coronal mass ejection/eruptive flare to estimate electron energy gains in individual islands in the flare current sheet. Results are provided in Chapter VII.

The evolution of a single plasmoid does not produce a big impact on the electron population, and therefore cannot ultimately explain the observed energetic radiation. The key idea is that reconnection occurs at many locations during a solar flare (*Sheeley et al.*, 2004; *Drake et al.*, 2006b; *Fermo et al.*, 2010; *Karpen et al.*, 2012), yielding a large number of plasmoids. Apart from simple contraction, these plasmoids can coalesce together as considered by *Drake et al.* (2013). Interaction and merger of many plasmoids might eventually lead to a large energy gain by the electron population. In this work, however, we only consider the effect of acceleration in a single magnetic island.

2.3 Diffusive Shock Acceleration (DSA) of SEP

CMEs, a form of solar eruptions, are a major player in the Sun-Earth connection and provide a major contribution to the SEP production. As solar flares, CMEs are associated with a major restructuring of the coronal magnetic field and the ejection of solar material ($\sim 10^{12-13}$ kg) and magnetic flux ($\sim 10^{13-15}$ Wb) into interplanetary space (e.g. *Roussev and Sokolov*, 2006). The shock wave driven by the ejecta can accelerate charged particles to ultra-relativistic energies as the result of Fermi acceleration processes (*Fermi*, 1949). The DSA is a mechanism that naturally produces the observed power-law spectra of energetic particles. A particle that crosses a shock front from the upstream flow gains a small amount of energy, which is proportional to its current energy. Due to turbulence, this particle may be scattered back to the upstream plasma and be once again overtaken by the shock, acquiring more energy in the process. This pattern may be repeated several times until a particle is finally swept downstream by the macroscopic plasma flow. DSA was first proposed by *Krymsky* (1977); *Axford et al.* (1977); *Bell* (1978a,b); *Blandford and Ostriker* (1978) to explain an origin of galactic cosmic rays, however, for the past four decades, this mechanism has been studied extensively in the context of co-rotating and traveling interplanetary shocks and has been demonstrated to be well supported both by theory (e.g. *Lee*, 1997; *Ng et al.*, 1999, 2003; *Zank et al.*, 2000) and observations (e.g. *Cliver et al.*, 2004; *Kahler*, 1994; *Tylka et al.*, 1999, 2005).

The most efficient particle acceleration takes place near the Sun at heliocentric distances of $2 - 15\,R_{\odot}$, where magnetic fields are the strongest, and the fastest particles can escape upstream of the shock, then propagating along the lines of the interplanetary magnetic field and reaching the Earth shortly after the initiation of the CME (≤ 1 hr).

As is the case with the solar flares, the theory of DSA is being debated within the community (*Reames*, 1999, 2002; *Tylka*, 2001), since very little is known from

observations about the dynamical properties of CME-driven shock waves in the inner corona soon after the onset of an eruption. The main argument against the shock origin is that near the Sun the ambient Alfvén speed is so large, due to the strong magnetic fields there, that a strongly super-magnetosonic shock wave is difficult to anticipate (*Gopalswamy et al.*, 2001). How soon after the onset of a CME the shock wave forms, and how it evolves in time depends largely on how this shock wave is driven by the erupting coronal magnetic fields.

To address the issue of shock origin during CMEs, it is required that real magnetic data are incorporated into a global model of the solar corona, as this had been done in, for example, *Roussev et al.* (2004). As proposed by *Tylka et al.* (2005), the shock geometry plays a significant role in the spectral and compositional variability of SEPs above ∼30 MeV/nuc. Therefore, in order to explain the observed signatures of gradual SEP events, global models of solar eruptions are required to explain the time-dependent changes in the strength and geometry of shocks during these events. The CME-driven shock continues to accelerate particles, and the shock passage at 1 AU is often accompanied by an enhancement of the energetic-particle flux. To simulate this effect, the shock wave evolution should be continuously traced while it propagates to 1 AU.

CHAPTER III

Single Particle Dynamics

3.1 Adiabatic Particle Motion

Those SEPs that escape acceleration regions embark on a long journey. As they traverse the vast distance that separates the Sun and the Earth (or any other object of interest), they keep interacting with the background plasma. Any particle may acquire or lose energy, or be scattered on the irregularities of the magnetic field, etc. To better understand the SEP-related phenomena, one needs to closely consider the dynamics of a single particle.

Behavior of SEP in strong magnetic fields reveals a consistent pattern. Unlike the majority of background particles, an energetic particle doesn't virtually exhibit a cross-field motion. This feature is consistent with observational data. In other words, SEPs tend to follow magnetic field lines. This observation allows reducing 3-D equations of particle dynamics to effectively 1-D form. Such reduction lays a path to a significant simplification of the problem of SEP modeling.

The problem of magnetic field aligned transport of a charged particle is well-known. It considers a particle that gyrates about a field line at such high frequency that any characteristic time scale of the enclosing system vastly exceeds the time of a single gyration. Under these circumstances one may take advantage of *adiabaticity* of particle's gyromotion. A comprehensive summary of the approach can be found

in, for example, *Northrop* (1963).

The concept of *adiabatic invariant* is closely related to any periodic motion, which occurs at a much higher rate than that of the evolution of its surroundings. The value of invariant is $\oint \mathbf{p} \cdot d\mathbf{q}$ and is preserved as long as the stated condition holds (*Landau and Lifshitz*, 1969). The integral is taken over a single period, $\mathbf{p}$ and $\mathbf{q}$ are the particle's generalized momentum and coordinates. The invariant corresponding to the particle's gyration about a magnetic field line, commonly referred to as the particle's magnetic moment, μ_m, is:

$$\mu_m = \frac{q\omega_g \rho_g^2}{2c} = \frac{W_g}{B}. \tag{3.1}$$

Here ω_g is the gyrofrequency, ρ_g is the particle's gyroradius, q is its electric charge, W_g is the kinetic energy of gyration, B is the magnitude of the magnetic field, and c is the speed of light. As the particle moves through the magnetized plasma, the value of the local magnetic field may increase or decrease. Conservation of the magnetic moment implies that the gyration energy, W_g, simultaneously increases or decreases, respectively. In a static magnetic field, the total particle energy, W, is preserved, so the energy of parallel motion , $W_\parallel$, decreases or increases to compensate for the change in W_g. If $W_\parallel$ decreases to zero, this leads to the phenomenon of magnetic mirroring: the particle has to bounce back. In a time-dependent magnetic field, on the other hand, an increase in the field strength leads to an increase in the gyration energy; however, the parallel energy does not decrease. The increase in total energy in this case is due to the associated induced electric field. This phenomenon is known as betatron acceleration.

Conservation of particle's magnetic moment allows a special treatment of Newton's equation of motion. The particle's trajectory, $\mathbf{r}(t)$, is split into two components, $\mathbf{r}(t) = \mathbf{r}_c(t) + \mathbf{r}_g(t)$, such that $< \mathbf{r}_c(t) >_g = \mathbf{r}_c(t)$ and $< \mathbf{r}_g(t) >_g = 0$. Here, the average

is taken over a period of gyration, T_g:

$$< * >_g = \frac{1}{T_g} \int_{t-T_g/2}^{t+T_g/2} (*)\, dt \tag{3.2}$$

This split is interpreted as: (1) $\mathbf{r}_g(t)$ represents rapid gyrations about the field line, while (2) $\mathbf{r}_c(t)$ is the trajectory of the particle's guiding center of gyrations. Thus averaged equation of particle's motion, disregarding terms of higher order in $\frac{m}{q}$, becomes (*Northrop*, 1963):

$$\ddot{\mathbf{r}}_c = \frac{q}{m} \left(\mathbf{E} \left(\mathbf{r}_c \right) + \dot{\mathbf{r}}_c \times \mathbf{B} \left(\mathbf{r}_c \right) \right) - \frac{\mu_m}{m} \nabla B \left(\mathbf{r}_c \right) \tag{3.3}$$

Hereafter in this chapter, electric, $\mathbf{E}$, and magnetic field, $\mathbf{B}$, are taken at the location of particle's guiding center.

Further, the particle's cross-field motion, its velocity perpendicular to the field line, $\mathbf{v}_\perp$, is largely determined by the local electro-magnetic fields and is essentially a combination of drifts:

$$\mathbf{v}_{c,\perp} = \dot{\mathbf{r}}_{c,\perp} = \mathbf{v}_{\mathbf{E}\times\mathbf{B}} + \frac{\mu_m}{q} \frac{\mathbf{b} \times \nabla B}{B} + \frac{m}{q} \frac{\mathbf{b} \times \dot{\mathbf{v}}_c}{B} \tag{3.4}$$

Hereafter, $\mathbf{b}$ is a unit vector along the direction of the magnetic field vector $\mathbf{B}$. The first term is the so-called $\mathbf{E} \times \mathbf{B}$-drift, results from the combined action of the electric and magnetic fields, $\mathbf{v}_{\mathbf{E}\times\mathbf{B}} = \frac{\mathbf{E}\times\mathbf{B}}{B^2}$, the second term is the gradient drift, the third terms includes the curvature drift. The latter two are mostly particle's reactions to spatial changes of the local magnetic field, the last term also represents other types of drifts. Both of these terms are usually small for practical purposes as demonstrated in below in this Chapter. The role of $\mathbf{E} \times \mathbf{B}$-drift is also discussed there. The motion

along the direction of the local magnetic field is governed by:

$$\dot{v}_{c,\parallel} = -\frac{\mu_m}{m}\frac{\partial B}{\partial s} + \mathbf{v}_{\mathbf{E}\times\mathbf{B}} \cdot \frac{d\mathbf{b}}{dt} + \frac{q}{m}E_{\parallel}, \tag{3.5}$$

with time derivative taken along the trajectory of a particle, s is the coordinate along the field line, $E_{\parallel}$ is the component of electric field parallel to the field line. The total kinetic energy of a particle averaged over the gyration period is

$$W = \frac{mv_{c,\parallel}^2}{2} + \frac{mv_{\mathbf{E}\times\mathbf{B}}^2}{2} + \mu_m B \tag{3.6}$$

Again, terms of higher order in $\frac{m}{q}$ are ignored. From Eqs. 3.4, 3.5 and 3.6, it can be demonstrated that the rate of change of particle's kinetic energy is

$$\dot{W} = \mu_m \frac{\partial B}{\partial t} + q\mathbf{E} \cdot \mathbf{v}_c \tag{3.7}$$

Note, the first term on the right hand side represent the aforementioned betatron effect.

3.2 Fermi Acceleration

Fermi (1949) described the following effect. Assume that a slowly changing large scale (compared to particle's gyroradius) magnetic irregularity moves with velocity $\mathbf{u}$. In the co-moving frame of reference the magnetic field is almost static and there is no electric field. If a charged particle encounters this irregularity, it will be reflected along the direction of $\mathbf{u}$. The process has a simple mechanical analogy of a ball reflecting from a moving wall. In the co-moving frame, this particle on interaction with the irregularity doesn't change its kinetic energy, since only the magnetic component of Lorentz force is exerted on it. However, this is not the case in the initial frame of reference, since there is an electric field $\mathbf{E} = -\mathbf{u} \times \mathbf{B}$. The particle gains energy if it

is overtaken by the irregularity, and loses energy if it overtakes the irregularity. This change in energy is known as the Fermi effect (or first order Fermi effect). It may demonstrated from Eqs. 3.3 (*Northrop*, 1963) that in the initial frame

$$\frac{dW}{dt} = -\mu_m u_\parallel \frac{\partial B}{\partial s} + m\left(u_\parallel - v_\parallel\right)^2 \mathbf{u}_\perp \cdot \frac{\partial \mathbf{b}}{\partial s}, \tag{3.8}$$

where $u_\parallel$ and $\mathbf{u}_\perp$ are the components of the irregularity's velocity parallel and perpendicular to the field line respectively. The first term on left hand side represents the Fermi effect of type A: a particle is reflected from a volume with stronger field, i.e. magnetic mirror. The second term is the Fermi effect of type B: a particle is diverted to the opposite direction by a curved line of force. It should be noted that in both cases a drift motion plays a key role in the effect. For both types of acceleration there is a component of drift, either gradient, or curvature, along the direction of electric field. Again, despite their key role in the Fermi effect, either of the two drifts has a relatively small effect on particle's displacement from the field line (see below in this Chapter). In application one still may treat particle as if its guiding center stayed on the same field line.

Note, for the Fermi acceleration of type A, the betatron effect plays the role of intermediate stage before the energy is transferred to the parallel motion. The particular interplay between the betatron effect and Fermi acceleration depends on the geometry of the irregularity and its evolution (e.g. *Somov and Bogachev*, 2003)

Another approach to the Fermi effect is to consider that a particle is temporarily trapped within a magnetic loop for the time corresponding to the particle's drift within the magnetic irregularity. While the particle resides within a magnetic trap, its *parallel action*, J, represents another adiabatic invariant and is conserved, provided particles close their orbits within a trap much more rapidly than the ambient magnetic field changes.

$$J = \oint m v_{c,\parallel} ds, \tag{3.9}$$

where the integral of the parallel momentum $mv_{\parallel}$ is taken along the field line coordinate s over one step of the spiral that particle follows. Since $J \sim p_{\parallel} L$, where L is the characteristic linear size of the magnetic trap, the contraction (expansion) of this trap leads to increase (decrease) in parallel momentum and, hence, in energy of parallel motion.

A particular application of this effects is particle acceleration in contracting plasmoids in reconnection current sheet as discussed in *Drake et al.* (2006a). In the case of the magnetic configuration considered in that work, the plasmoid contracts after formation, thus reducing the length of the particle's path.

These simple considerations of conservation of adiabatic invariants show that the magnetic field evolution strongly affects the motion of individual particles. If the local plasma conditions within a magnetic trap, e.g. a plasmoid, experience a significant change during its evolution, the energies of the particles trapped within also change significantly. This process is revisited in Chapter VII.

3.3 Validity of Field-Aligned Transport

As mentioned above, drifts in Eq. 3.4, except $\mathbf{E} \times \mathbf{B}$-drift, though important in the context of energy gain, have a negligible effect on particles' displacement relative to the field lines. The following estimate confirms this assertion. For the magnetic field of Parker's spiral the magnitude of these drifts, $v_{\rm drift}$, has order of W/qBL, where L is the characteristic scale of the system. This translates to $v_{\rm drift}/v \sim \rho_g/L$, which is small for the particles in the consideration.

Thus, the only drift that stays in the consideration is $\mathbf{E} \times \mathbf{B}$-drift. Under ideal MHD its contribution to the particle's motion has a simple and straight-forward

interpretation. Since $\mathbf{E} = -\mathbf{u} \times \mathbf{B}$, where $\mathbf{u}$ is the local bulk velocity of plasma, then $\mathbf{v_{E \times B}} = \mathbf{u} - \mathbf{bb}cdot\mathbf{u} = \mathbf{u}_\perp$. In other words, the drift is equal to the component of plasma velocity perpendicular to the local magnetic field. Thus, it forces a particle to advect *together* with the field line it resides on and ensures the overall validity of the assumption of the field-aligned motion.

3.4 Particle Dynamics in the Co-Moving Frame

Finally, the equations of field aligned transport may be reformulated in the frame of reference moving with a field line. Again, we assume that particles don't travel across field lines. In this frame particle's 1-D velocity is

$$v_\parallel = \frac{ds}{dt} \tag{3.10}$$

$$\frac{dp_\parallel}{dt} = -\mu_m \frac{\partial B}{\partial s} + m\mathbf{b} \cdot \frac{d\mathbf{u}}{dt} + m\frac{du_\parallel}{dt} = -\mu_m \frac{\partial B}{\partial s} - \mathbf{u} \cdot \frac{d\mathbf{b}}{dt} \tag{3.11}$$

The time derivative along the particle's trajectory is related to the substantial derivative, i.e. along the trajectory of a fluid element, as

$$\frac{d*}{dt} = \frac{D*}{Dt} - \frac{p_\parallel}{m}\frac{\partial *}{\partial s} \tag{3.12}$$

Also, the stretching of the field line, i.e. distance between fluid elements, changes as

$$\frac{D \ln \delta_s}{Dt} = \mathbf{bb} : \nabla \mathbf{u} \tag{3.13}$$

Equation becomes

$$\frac{dp_\parallel}{dt} = -\mu_m \frac{\partial B}{\partial s} - \frac{D \ln \delta_s}{Dt} p_\parallel - m\mathbf{b} \cdot \frac{D\mathbf{u}}{Dt} \tag{3.14}$$

In the co-moving frame of reference, the perpendicular component of motion is gyrations about the line. From the rate of change of gyration energy

$$\frac{dp_\perp}{dt} = \frac{1}{2}\frac{p_\perp}{W_\mathrm{g}}\frac{dW_\mathrm{g}}{dt} = \frac{1}{2}\frac{d\ln B}{dt}p_\perp = \frac{1}{2}\left(\frac{D\ln B}{Dt} + \frac{\partial \ln B}{\partial s}\right)p_\perp \tag{3.15}$$

3.5 Concluding Remark

The field line approach works well, when ideal MHD is a reasonable approximation and, thus, $\mathbf{E}\times\mathbf{B}$-drift ensures that particles advect together with the background plasma. However, it is not always the case. For example, near the reconnection sites one can't completely disregard the action of reconnection electric field, which displaces particles from their field lines. Some estimates can be done for this particular case. It has been demonstrated (see e.g. *Craig and Litvinenko*, 2002; *Egedal et al.*, 2012) that a particle, while passing through a reconnection current sheet gains energy of order $\sim mV_A^2/2$. In the case of energetic particles this usually is a vary small fraction of particle's energy. Also, since magnetic lines recede rapidly from the reconnection site, few particles experience this already small effect and may usually be disregarded, when considering particle acceleration in plasmoids near reconnection sites.

CHAPTER IV

Kinetic Description of SEP

4.1 Introduction

The kinetic transport of energetic particle population through the inter-planetary space is an important problem in space science. It was studied since the discovery of the Galactic Cosmic Rays (GCR), the energetic particles originating from beyond the Solar system. A comprehensive summary of the problem can be found in the review by *Parker* (1965). Although results in the said review are obtained in a different context, some can readily be applied for the SEP transport.

The distribution of SEPs is far from Maxwellian, therefore, they should be characterized by a (canonical) distribution function $F(\mathbf{R}, \mathbf{p}, t)$ of coordinates, $\mathbf{R}$, and momentum, $\mathbf{p}$, as well as time, t, such that the number of particles, dN, within the elementary volume, $d^3\mathbf{R}$, is given by the following normalization integral: $dN = d^3\mathbf{R} \int d^3\mathbf{p} F(\mathbf{R}, \mathbf{p}, t)$. In a magnetized plasma, it is convenient to deal with the distribution function at the given point, $\mathbf{R}$, in the co-moving frame of reference, which moves with the local velocity of interplanetary plasma, $\mathbf{u}(\mathbf{R}, t)$. Also, we introduce spherical coordinates, $(p = |\mathbf{p}|, \mu = \mathbf{b} \cdot \mathbf{p}/p, \varphi)$, in the momentum space with its polar axis aligned with the direction of the magnetic field, $\mathbf{b}$. Herewith, μ is the cosine of pitch-angle. The normalization integral in these new variables becomes: $dN = d^3\mathbf{R} \int_0^\infty p^2 dp \int_{-1}^1 d\mu \int_0^{2\pi} d\varphi F(\mathbf{R}, p, \mu, \varphi, t)$. Using this canonical distri-

bution function, one can also define a gyrotropic distribution function, $f(\mathbf{R}, p, \mu, t) = \frac{1}{2\pi}\int_0^{2\pi} d\varphi F(\mathbf{R}, p, \mu, \varphi, t)$. This function is designed to describe the particle motion averaged over the phase of its gyration about the magnetic field. The isotropic (omnidirectional) distribution function, $f_0(\mathbf{R}, p, t) = \frac{1}{2}\int_{-1}^{1} d\mu f(\mathbf{R}, p, \mu, t)$ is averaged over the pitch angle too. The normalization integrals are: $dN = 2\pi d^3\mathbf{R}\int_0^\infty p^2 dp \int_{-1}^{1} d\mu f(\mathbf{R}, p, t) = 4\pi d^3\mathbf{R}\int_0^\infty p^2 dp f_0(\mathbf{R}, p, t)$

The commonly used kinetic equation for the isotropic part of the distribution function has been introduced in *Parker* (1965):

$$\frac{\partial}{\partial t} f_0(\mathbf{R}, p, t) + (\mathbf{u}\cdot\nabla) f_0(\mathbf{R}, p, t) - \frac{1}{3}(\nabla\cdot\mathbf{u})\frac{\partial}{\partial \ln p} f_0(\mathbf{R}, p, t) = \nabla\cdot(\varkappa\cdot\nabla f_0(\mathbf{R}, p, t)) + S, \tag{4.1}$$

where $\varkappa = D_{xx}\mathbf{bb}$ is the tensor of parallel (spatial) diffusion along the magnetic field, S is the source term. In this approximation, the cross-field diffusion of particles is neglected.

Eq. 4.1 captures the effect of interplanetary plasma and Interplanetary Magnetic Field (IMF) on the SEP transport and acceleration. The term proportional to the divergence of $\mathbf{u}$ is the adiabatic cooling, for $(\nabla\cdot\mathbf{u}) > 0$, or (the first order Fermi) acceleration in compression or shock waves. According to estimates by *Parker* (1965), during quiet time the adiabatic scaling of particles' energy from their origin to 1 AU is $\propto (\rho_{1AU}/\rho_\odot)^{(n/3)}$, where n=2 for non-relativistic and n=1 for relativistic particles.

Small scale irregularities also have a significant impact on particle propagation. Their scale is $\sim 10^5 \div 10^7$km, which is comparable with gyroradii of SEP but very small compared to 1 AU. Particles scatter on these irregularities, and on the large scale the particle motion can be described as diffusion, the first term on the right in Eq. 4.1. Based on Eq. 4.1, *Krymsky* (1977); *Axford et al.* (1977); *Bell* (1978a,b); *Blandford and Ostriker* (1978) proposed the DSA mechanism to explain the observed power-law spectra of GCRs.

When pitch angles of particles are taken into account, one needs to consider the appropriate scattering in the momentum space, as accounted for in the equation for a non-relativistic gyrotropic distribution function $f(\mathbf{R}, p, \mu, t)$ from *Skilling* (1971):

$$\begin{aligned} \frac{\partial f}{\partial t} + (\mathbf{u} + \mu v \mathbf{b}) \cdot \nabla f \quad + \\ \left[\frac{1-3\mu^2}{2} (\mathbf{bb} : \nabla \mathbf{u}) - \frac{1-\mu^2}{2} (\nabla \cdot \mathbf{u}) - \frac{\mu}{v} \left(\mathbf{b} \cdot \frac{D\mathbf{u}}{Dt} \right) \right] \frac{\partial f}{\partial \ln p} \quad + \\ \frac{1-\mu^2}{2} \left[v (\nabla \cdot \mathbf{b}) - 3\mu (\mathbf{bb} : \nabla \mathbf{u}) + \mu (\nabla \cdot \mathbf{u}) - \frac{2}{v} \left(\mathbf{b} \cdot \frac{D\mathbf{u}}{Dt} \right) \right] \frac{\partial f}{\partial \mu} \quad = \quad \frac{\delta f}{\delta t} + S, \end{aligned} \tag{4.2}$$

where v is particle's velocity, and $D(*)/Dt = \partial(*)/\partial t + \mathbf{u} \cdot \nabla(*)$ is the substantial derivative

The particle scattering rate, $\frac{\delta f}{\delta t}$, in this model is due to the particle interaction with the Alfvén wave turbulence which is described by the Fokker-Planck diffusion over the pitch-angle:

$$\frac{\delta f}{\delta t} = \frac{\partial}{\partial \mu} \left(D_{\mu\mu} \frac{\partial f}{\partial \mu} \right) \tag{4.3}$$

The diffusion coefficient, $D_{\mu\mu}$, may be expressed in terms of the Alfvén wave turbulence spectrum, as discussed in this Chapter below. Since both types of diffusion, spatial and pitch-angle, are different representations of the same physical process, scattering on the magnetic field irregularities, one can establish a relation between D_{xx} and $D_{\mu\mu}$ (*Jokipii*, 1966; *Earl*, 1974):

$$D_{xx} = \frac{v^2}{8} \int_{-1}^{1} \frac{(1-\mu^2)^2}{D_{\mu\mu}} d\mu \tag{4.4}$$

An important physical effect related to particles' pitch angle distribution is the focusing effect (*Earl*, 1976, and references therein), also referred to as focused transport. The effect takes places under conditions that constrain pitch-angle scattering across μ=0. In the extreme case, when particles can't change the direction of their

propagation along their field lines, the whole population is effectively split into two independent hemispheric subpopulations, one of particles propagating inward, the other of particles propagating outward. The idea of such splitting has been utilized in *Isenberg* (1997). Effects of interaction of particles with solar wind plasma and IMF such as adiabatic cooling/heating on the focused transport have been studied in, for example, *Ruffolo* (1995). A detailed view on the different aspects of evolution of distribution of particles propagating along magnetic-field lines, i.e. convection, cooling/heating, and focusing, can be found in *Kóta and Jokipii* (1997).

4.2 Lagrangian Coordinates and Field Line Advection Model

The equations above constitute a general mathematical approach to the problem of SEP transport. However, this consideration is computationally challenging: a spatially 3-D propagation of particles requires significant resources. This can be avoided by observing that both Eq. 4.1 and Eq. 4.2 assume that the particle motion in physical space consists of the particle guiding center's displacement along the IMF and advection with plasma into which the IMF is frozen. This property allows us to represent these equations in the Lagrangian coordinates. The benefits of this approach is the reduction of a complex 3-D problem to a multitude of much simpler 1-D problems, with no loss of generality.

At the early age of the mechanics of continuous media there were two competing approaches to a mathematical description of the motion of fluids. In Eulerian coordinates, $\mathbf{R}, t$, the distribution of the fluid parameters (density, velocity, temperature, pressure, etc) at each instant of time, t, is provided as a function of coordinates, $\mathbf{R}$, in some coordinate frame. No need to emphasize that any given point, $\mathbf{R}$ is immovable, while the fluid passes this point with the local flow velocity $\mathbf{u}(\mathbf{R}, t)$, so that at each time instant the fluid element at this point differs from that present at this point a while ago. In contrast with this approach, the Lagrangian coordinates, $\mathbf{R}_L$, stay

with the given fluid element rather than with the given position in space. While the fluid moves, each moving fluid element keeps unchanged the value of the Lagrangian coordinates, $\mathbf{R}_L$, while its spatial location, $\mathbf{R}(\mathbf{R}_L, t)$, changes in time in accordance with the definition of the fluid local velocity:

$$\frac{D\mathbf{R}(\mathbf{R}_L, t)}{Dt} = \mathbf{u}(\mathbf{R}, t) \tag{4.5}$$

Herewith, the partial time derivative at constant Lagrangian coordinates, $\mathbf{R}_L$ is denoted as $\frac{D}{Dt}$, while the usual denotations, $\frac{\partial}{\partial t}$ are used to denote the partial time derivative at constant Eulerian coordinates, $\mathbf{R}$. As usually, we choose the Lagrangian coordinates for a given fluid element equal to the Eulerian coordinates of this element at the initial time instant, $\mathbf{R}_L = \mathbf{R}|_{t=0}$. For numerical simulations, with any choice of the grid in Lagrangian coordinates, $(\mathbf{R}_{ijk})_L = (\mathbf{R}_{ijk})|_{t=0}$, one can numerically solve the multitude of ordinary differential equations, Eq. 4.5, to trace the spatial location for all Lagrangian grid points in the evolving fluid velocity field, $\mathbf{u}(\mathbf{R}, t)$, as long as the latter is known.

An example of application of Lagrangian coordinates to the Parker equation, Eq. 4.1, is FLAMPA (*Sokolov et al.*, 2004).

In order to express the focused transport equation, Eq. 4.2, in Lagrangian coordinates, we use the substantial derivative, $D(*)/Dt$, and the following form of continuity

$$\nabla \cdot \mathbf{u} = -\frac{D \ln \rho}{Dt} \tag{4.6}$$

and induction equation

$$(\mathbb{I} - \mathbf{bb}) : \nabla \mathbf{u} = -\frac{D \ln B}{Dt} \tag{4.7}$$

ρ is the plasma density, $\mathbb{I}$ is the identity matrix, and, as before, the coordinate s measures a distance along the IMF lines. This distance is such that: $\partial/\partial s = \mathbf{b} \cdot \nabla$. The time-dependent changes in the distance between two neighboring Lagrangian

meshes, δs, is described by the following evolutionary equation (e.g. *Landau and Lifshitz*, 1959):

$$\frac{D \ln \delta s}{Dt} = \mathbf{bb} : \nabla \mathbf{u} \tag{4.8}$$

From the solenoidal constraint, $\nabla \cdot \mathbf{B} = 0$, one can find that:

$$\nabla \cdot \mathbf{b} = -\partial \ln B / \partial s \tag{4.9}$$

Relations above allow a new treatment of Eq. 4.2 for field-aligned transport of SEP and acceleration (*Kóta and Jokipii*, 2004; *Kóta et al.*, 2005a):

$$\begin{aligned} \frac{Df}{Dt} + v\mu \frac{\partial f}{\partial s} \quad + \\ \left[\mu^2 \frac{D \ln \rho}{Dt} + \frac{1-3\mu^2}{2} \frac{D \ln B}{Dt} - \frac{\mu}{v} \mathbf{b} \cdot \frac{D\mathbf{u}}{Dt} \right] \frac{\partial f}{\partial \ln p} \quad + \\ \frac{1-\mu^2}{2} \left[-v \frac{\partial \ln B}{\partial s} + \mu \frac{D \ln (\rho^2 / B^3)}{Dt} - \frac{2}{v} \mathbf{b} \cdot \frac{D\mathbf{u}}{Dt} \right] \frac{\partial f}{\partial \mu} \quad = \quad \frac{\delta f}{\delta t} + S \end{aligned} \tag{4.10}$$

where f is a function of (s, p, μ, t).

Also, by introducing the parallel, $p_{||} = \mu\, p$, and perpendicular, $p_\perp = (1-\mu^2)^{1/2}\, p$, components of the momentum instead of pitch-angle, μ, one can write Eq. 4.2 in the form:

$$\begin{aligned} \frac{Df}{Dt} + \left(\frac{ds}{dt} \right)_p \frac{\partial f}{\partial s} + \left(\frac{dp_\perp}{dt} \right)_p \frac{\partial f}{\partial p_\perp} + \\ + \left(\frac{dp_{||}}{dt} \right)_p \frac{\partial f}{\partial p_{||}} = \left(\frac{\delta f}{\delta t} \right)_{scat} + S. \end{aligned} \tag{4.11}$$

Here, the coefficients $(...)_p$ in the kinetic equation, which are also time-derivatives of canonical variables of a particle along its trajectory, are given by Eqs. 3.10 - 3.15,

which we reproduce for convenience:

$$\left(\frac{ds}{dt}\right)_p = v_{||}, \tag{4.12}$$

$$\left(\frac{dp_\perp}{dt}\right)_p = \frac{1}{2}\left(\frac{D\ln B}{Dt} + \frac{\partial \ln B}{\partial s} v_{||}\right) p_\perp, \tag{4.13}$$

and

$$\left(\frac{dp_{||}}{dt}\right)_p = -\mu_m \frac{\partial B}{\partial s} - \frac{D\ln \delta s}{Dt} p_{||} - m_i \mathbf{b}\cdot\frac{D\mathbf{u}}{Dt}. \tag{4.14}$$

Hereafter, m_i is the ion mass and index i denotes the sort of ions. The use of the equations of single particle's dynamics in the kinetic equations highlights the deep connection between these two different approaches to describing SEPs. The terms in Eqs. 4.11-4.14 have simple and straightforward physical meaning. The evolution of the distribution function (first term on the left-hand side (LHS) of Eq. 4.11) is governed by: (1) particle advection (second term on LHS); (2) conservation of the magnetic moment $\mu_m = p_\perp^2/(2m_i B)$ along the particle trajectory (third term on LHS); (3) magnetic mirror force (first term on RHS of Eq. 4.14); (4) first-order Fermi acceleration, with the conservation of another adiabatic invariant, $p_{||}\delta s$ (corresponds to second term on RHS of Eq. 4.14); (5) action of a non-inertial force $\sim -D\mathbf{u}/Dt$; and (6) particle scattering and sources (RHS of Eq. 4.11). Regarding process (3), the first term on the RHS of Eq. 4.14 is the force repelling the particle from a magnetic mirror. For a time-independent magnetic field (i.e., $DB/Dt = 0$), the action of this force balances the energy change due to the perpendicular momentum increase (adiabatic focusing), thus ensuring the energy conservation. The above Eq. 4.11 is more convenient for computations, especially within the Monte-Carlo approach.

The μ-dependent form of Eq. 4.11 can be written as:

$$\frac{Df}{Dt} + \mu v \frac{\partial f}{\partial s} + \left(\frac{dp}{dt}\right)_p \frac{\partial f}{\partial p} + \left(\frac{d\mu}{dt}\right)_p \frac{\partial f}{\partial \mu} = \left(\frac{\delta f}{\delta t}\right)_{scat} + S, \tag{4.15}$$

where

$$\left(\frac{dp}{dt}\right)_p = \frac{p_{||}}{p}\left(\frac{dp_{||}}{dt}\right)_p + \frac{p_\perp}{p}\left(\frac{dp_\perp}{dt}\right)_p, \tag{4.16}$$

and

$$\left(\frac{d\mu}{dt}\right)_p = \frac{p_\perp}{p^2}\left(\frac{dp_{||}}{dt}\right)_p - \frac{p_{||}p_\perp}{p^3}\left(\frac{dp_\perp}{dt}\right)_p. \tag{4.17}$$

4.3 Wave-Particle Interaction

Value of the coefficient of pitch angle diffusion in the quasi-linear theory has been derived and studied in a number of works (*Jokipii*, 1966; *Lee*, 1982, 1983):

$$D_{\mu\mu} = \frac{\pi e^2 \left(1-\mu^2\right) v}{2c^2 \left|\mu\right| p^2} I\left(\frac{eB}{cp\mu}\right); \quad \left\langle \delta B^2 \right\rangle = \int_{-\infty}^{+\infty} I(k) dk \tag{4.18}$$

This relation has been used in *Sokolov et al.* (2004), the spectrum of turbulence in Eq. 4.18 was chosen to be $I(k) = (\delta B)^2 / \pi \left|k\right|$, where k is the wave number.

Above in this Chapter, we have summarized the equations of the kinetic treatment of SEP propagation and acceleration, specifically that of pitch-angle scattering and particle diffusion. However, the complexity and importance of these effects require a much closer consideration, see below in this Chapter.

According to DSA, during gradual SEP events particle acceleration occurs near the Sun at the CME-driven shock waves. Fast DSA requires that particles experience frequent scattering back and forth across the shock-wave front. This enhanced scattering of particles, unless the shock wave is entirely perpendicular, occurs on the Alfvén waves that are generated by the accelerated particles streaming from the

shock (e.g. *Bell*, 1978a,b; *Lee*, 1983). This demonstrates the necessity for a complete SEP model to require the particle acceleration model to be coupled with a realistic model of self-excited Alfvén turbulence and a model of particle transport in realistic turbulent IMF.

4.3.1 Excitation of Turbulence

The self-generated Alfvén waves produced in the vicinity of a shock-wave front have been demonstrated to have important consequences for SEP elemental abundance variations (*Ng et al.*, 1999; *Tylka et al.*, 1999) and the evolution of SEP anisotropies (*Reames et al.*, 2001).

The Alfvén wave excitation in a uniformly magnetized plasma has been studied in great detail (*Ichimaru*, 1973). The dispersion relation, i.e. relation between the wave's frequency, ω, and the wave number, k, takes a very simple form once circularly polarized Alfvén waves are introduced (see Eq. 5.29 from *Ichimaru*, 1973): $(kc/\omega)^2 = \epsilon_{r(l)}(k,\omega)$, for right, r, and left, l, polarization, respectively. Here $\epsilon_{r(l)}(k,\omega)$ is a dielectric response function, which is complex in general. By neglecting the excitation and damping of the Alfvén waves (thus assuming that $\Im(\omega) = 0$ and $\Im(\epsilon_{r(l)}) = 0$), their dispersion relation becomes: $\omega/|k| = c/\sqrt{\epsilon_{r(l)}} = V_A$. The wave frequency, ω, should be smaller than the ion-cyclotron frequency, $\omega_{ci} = eZ_iB/(m_ic)$, i.e., $\omega \ll \omega_{ci}$, otherwise the wave experiences a strong Landau damping at ions. Here eZ_i is the ion charge.

In the next approximation, the increment of Alfvén waves instability due to the presence of supra-thermal ion fluxes can be expressed in terms of the imaginary part of the dielectric response function (see *Ichimaru*, 1973). By assuming a harmonic time-dependence for the wave amplitude $\sim \exp\left[-i\,\Re(\omega)t + \Im(\omega)t\right]$, one can find the growth rate of the wave intensity ($\propto$ square of wave amplitude) to be $\gamma_{r(l)}(k) = 2\Im(\omega)$. Using the dispersion equation above and disregarding terms of second and higher orders in

$\Im(\omega)/\Re(\omega)$, this can be written as: $\gamma_{r(l)}(k) \approx -\Im(\epsilon_{r(l)})\,\omega V_A^2/c^2$. Hereafter, $\omega \approx \Re(\omega)$. If one adopts the quasi-linear (QL) approach, the input from the supra-thermal ions to the dielectric response function is given by Eq. 7.59 from *Ichimaru* (1973):

$$\gamma_{r(l)} = \frac{e^2 Z_i^2 V_A^2}{2\varepsilon_0 m_i c^2 \omega} \int d\mathbf{p}\,(\mathbf{p}_\perp \cdot \mathbf{G}\{f\})\,\Im\left(\frac{1}{kv_{||} - \omega \mp \omega_{ci} - i0}\right), \tag{4.19}$$

where plus (minus) sign correspond to right (left) wave polarization, ε_0 is the vacuum permettivity. Here we introduced the differential operator

$$\mathbf{G}\{f\} = \left(\omega - kv_{||}\right)\frac{\partial f}{\partial \mathbf{p}_\perp} + k\mathbf{v}_\perp \frac{\partial f}{\partial p_{||}}, \tag{4.20}$$

which is only by a numerical factor different from that used in *Ng et al.* (2003). Here, parallel, $p_{||}$, and perpendicular, $\mathbf{p}_\perp$, components of the particle momentum, as well as positive and negative values of the wave number are defined with respect to the direction of the regular magnetic field.

The pole in Eq. 4.19 should be bypassed using the Landau rule (e.g. *Ginzburg and Rukhadze*, 1975):

$$\Im\left(\frac{1}{kv\mu - \omega \mp \omega_{ci} - i0}\right) = \pi\delta(kv\mu - \omega \mp \omega_{ci}), \tag{4.21}$$

in which the Dirac δ-function is used. Thus, Eq. 4.19 can be re-written as follows:

$$\gamma_\sigma = \int d\mathbf{p}\, K_\sigma(k, \omega, \mathbf{p})\,(\mathbf{p}_\perp \cdot \mathbf{G}\{f\})\,, \tag{4.22}$$

where σ denotes all four possible combinations of wave polarization and direction of propagation, and

$$K_\sigma(k, \omega, \mathbf{p}) = \frac{\pi\,(eZ_iV_A)^2}{2\varepsilon_0 m_i c^2 \omega}\,\delta\left(|k|\,(\mu v - V_\sigma) - g_\sigma \omega_{ci}\right). \tag{4.23}$$

Here we introduce $V_\sigma = \omega/k$, which is equal to $\pm V_A$ for waves with positive and negative k, respectively. Also, $g_\sigma = \pm 1$, where the positive (negative) sign stands for the combination of right (left) wave polarization and $k > 0$ or for left (right) wave polarization and $k < 0$. These two branches of waves are in resonance with particles having a positive longitudinal velocity, $(\mu v - V_\sigma)$, with respect to the waves. Note, Eq. 4.23 is only valid in the QL approximation, whereas Eq. 4.22 is more general and holds true even in the non-linear theory see (see *Ng et al.*, 2003).

If one neglects the wave dispersion, there are only two admissible values for the phase speed of the wave, V_σ. Thus, the expression for the collision integral (see Eq. 4.26 below) for waves of a given branch becomes very simple and easy to compute in a special frame of reference in which the particle velocity is centered with respect to the phase speed of the wave.

In our approach, we introduce for each wave branch a transformed particle velocity of the kind $\mathbf{v}_\sigma = \mathbf{v} - V_\sigma \mathbf{b}$, and we express the growth rate, as well as the collision integral below, in terms of the distribution function, $f(\mathbf{p}, \mathbf{x}, t)$, transformed as follows: $f(\mathbf{p}_\sigma + m_i V_\sigma \mathbf{b}, \mathbf{x}, t)$. Under this transformation, the differential operator $\mathbf{G}$, when applied to a gyrotropic distribution function, involves only the derivative with respect to the transformed pitch angle, μ_σ:

$$\mathbf{G}\{f\} = \frac{\omega}{V_\sigma} \frac{\mathbf{v}_{\sigma\perp}}{p_\sigma} \frac{\partial f}{\partial \mu_\sigma} \tag{4.24}$$

Thus, Eq. 4.22 becomes:

$$\gamma_\sigma = 2\pi \int p_\sigma^2 dp_\sigma d\mu_\sigma K_\sigma(k, \omega, \mathbf{p}_\sigma + m_i V_\sigma \mathbf{b}) \left[\left(1 - \mu_\sigma^2\right) \frac{\omega}{V_\sigma} v_\sigma \frac{\partial f}{\partial \mu_\sigma} \right]. \tag{4.25}$$

4.3.1.1 Particle Scattering

The influence of the Alfvén turbulence on the supra-thermal particles can be evaluated in the following manner. The harmonic electric field of the waves, $\delta\mathbf{E}_w$, generates a harmonic magnetic field, $\delta\mathbf{B}_w = (\mathbf{k} \times \delta\mathbf{E}_w)/\omega$. The general solution of the kinetic equation for the perturbation of the distribution function, δf, is a linear response to the perturbation from the electromagnetic field of the waves, i.e. $\delta f = T\{e\,[\delta\mathbf{E}_w + (\mathbf{v} \times \delta\mathbf{B}_w)] \cdot \frac{\partial f}{\partial \mathbf{p}}\}$. Here $T\{\}$ is some linear operator. This general solution for δf can be also written as: $\delta f = e\,T\{(\delta\mathbf{E}_w \cdot \mathbf{G}\{f\})\}/\omega$.

Here, to derive the collision integral, the distribution function is separated in regular and irregular part due to the turbulent fluctuations. In the kinetic equation for the regular part of f, the scattering integral appears to be the average of $-e\,\{\delta\mathbf{E}_w + (\mathbf{v} \times \delta\mathbf{B}_w) \cdot (\partial\delta f/\partial\mathbf{p}) = -e\,\delta\mathbf{E}_w \cdot \mathbf{G}\{\delta f\}/\omega$. After substituting δf, this bi-linear by $\delta\mathbf{E}_w$ term should be averaged by the wave ensemble (yielding $I(k) \sim \delta\mathbf{E}_w^2(k)$), and then integrated by the wave spectrum (yielding integral of the kind $\int dk\, I(k)...$), so that some yet unknown linear integral-operator should result in:

$$\left(\frac{\delta f}{\delta t}\right)_{scat} = \sum_\sigma \int dk\, I_\sigma \mathbf{G} \cdot \{K'_\sigma(k, \omega, \mathbf{p})\mathbf{G}\{f\}\}. \tag{4.26}$$

Here, K'_σ is related to K_σ because the kernels in Eqs. 4.25 and 4.26 are coupled as the result of the energy conservation in the system comprising all ions and all waves (see *Ng et al.*, 2003). With the use of the normalization $(\delta\mathbf{B})^2 = \sum_\sigma \int dk\, I_\sigma(k)$, and since the energy of the turbulent pulsations is twice that of the magnetic field, $(\delta\mathbf{B})^2/2\mu_0$, one can express the total growth rate of the wave energy in terms of γ_σ. This should be also equal to the particle energy loss due to the scattering by turbulence. Stemming from these considerations, we come up with the following formulation of the energy

conservation law:

$$\sum_{\sigma} \int dk \, \frac{2I_{\sigma}(k)\gamma_{\sigma}(k)}{2\mu_0} + \int d\mathbf{p} \, \frac{p^2}{2m_i} \left(\frac{\delta f}{\delta t} \right)_{scat} = 0. \tag{4.27}$$

Let us now integrate by parts the energy losses with the collision integral given by Eq. 4.26. Using the identity $\mathbf{G}\{p^2\} = 2\omega \mathbf{p}_{\perp}$, and after substituting γ_{σ} from Eq. 4.22, we find that the energy conservation requires the following relation between the kernels of the integrals in Eqs. 4.22 and 4.26:

$$\frac{\omega K'_{\sigma}(k, \omega, \mathbf{p})}{m_i} = \frac{K_{\sigma}(k, \omega, \mathbf{p})}{\mu_0}. \tag{4.28}$$

Note, Eq. 4.28 is much more general than any existing model for wave generation and/or particle scattering. For comparison, a similar formula was obtained by *Ng et al.* (2003) using the non-linear growth rate for Alfvén turbulence. In computations, however, the use of approximations for the kernels of integral equations is almost inevitable. Therefore, the use of general relations like Eq. 4.28 in choosing approximations for the wave generation and particle scattering is necessary to make them comply with each other and with the energy conservation in the system.

In the frame of reference moving with the Alfvén waves, the collision integral is given by:

$$\left(\frac{\delta f}{\delta t} \right)_{scat} = \sum_{\sigma} \frac{\partial}{\partial \mu_{\sigma}} \left(D^{\sigma}_{\mu\mu} \frac{\partial f}{\partial \mu_{\sigma}} \right), \tag{4.29}$$

where

$$D^{\sigma}_{\mu\mu} = (1 - \mu^2_{\sigma}) \int dk \, I_{\sigma}(k) \frac{k^2}{\mu_0 m_i \omega} K_{\sigma}(k, \omega, \mathbf{p}_{\sigma} + m_i V_{\sigma} \mathbf{b}). \tag{4.30}$$

In the QL approximation, the integral by k can be taken using the presence of δ-

function in K_σ (see Eq. 4.23). Thus, for given σ and μ_σ, Eq. 4.30 becomes:

$$D^\sigma_{\mu\mu} = \frac{\pi(1-\mu_\sigma^2)e^2 Z_i^2 v_\sigma}{2p_\sigma^2|\mu_\sigma|} I_\sigma \left(\frac{\omega_{ci}}{v_\sigma|\mu_\sigma|}\right), \tag{4.31}$$

if $g_\sigma = \text{sign}(\mu_\sigma)$, and vanishes otherwise.

4.3.2 Diffusive Limit

The diffusive limit is less exact but widely used. When the particle speed is large compared to the Alfvén speed, one can neglect the difference between μ and μ_σ, and adopt a scattering integral:

$$\left(\frac{\delta f}{\delta t}\right)_{scat} = \frac{\partial}{\partial \mu}\left(D_{\mu\mu}\frac{\partial f}{\partial \mu}\right), \; D_{\mu\mu} = \sum_\sigma D^\sigma_{\mu\mu}. \tag{4.32}$$

Now let us consider $f(\mathbf{R}, p, \mu, t) = f_0(\mathbf{R}, p, t) + f_1(\mathbf{R}, p, \mu, t)$, and assume that $f_1 \ll f_0$. The isotropic part of the distribution function, f_0, has no dependence on μ. Let us also assume that $u << v$, and suppose that $D^{-1}_{\mu\mu}$ is small compared to any hydrodynamic time. Thus, the function f_1 can be obtained from the steady-state form of Eq. 4.10:

$$\mu v \frac{\partial f_0}{\partial s} = \frac{\partial}{\partial \mu}\left(D_{\mu\mu}\frac{\partial f_1}{\partial \mu}\right). \tag{4.33}$$

From here, $\partial f_1/\partial \mu$ can be expressed as:

$$\frac{\partial f_1}{\partial \mu} = -v\frac{1-\mu^2}{2D_{\mu\mu}}\frac{\partial f_0}{\partial s}. \tag{4.34}$$

To obtain the evolutionary equation for f_0, i.e. the Parker equation, Eq. 4.1, let us average Eq. 4.10 with respect to the particle pitch angle:

$$\frac{Df_0}{Dt} + \langle \mu v \frac{\partial f_1}{\partial s} \rangle_\mu + \frac{1}{3}\frac{d\ln\rho}{dt} p \frac{\partial f_0}{\partial p} - \\ -\langle \frac{1-\mu^2}{2}\left(v\frac{\partial \ln B}{\partial s}\right)\frac{\partial f_1}{\partial \mu}\rangle_\mu = S, \tag{4.35}$$

where $S = \langle S \rangle_\mu$ and $\langle ... \rangle_\mu = (1/2)\int d\mu(...)$. The second and fourth terms in Eq. 4.35 can be grouped together and the result reads: $(Bv/2)\langle (1-\mu^2)\partial^2(f_1/B)/(\partial s \partial \mu)\rangle_\mu$. Then, using Eq. 4.34, this term transforms into: $-B\partial[(D_{xx}/B)(\partial f_0/\partial s)]/\partial s$. Thus, the transport equation of particles in the diffusive limit reduces to:

$$\frac{Df_0}{Dt} + \frac{1}{3}\frac{d\ln\rho}{dt} v \frac{\partial f_0}{\partial v} - B\frac{\partial}{\partial s}\left(\frac{D_{xx}}{B}\frac{\partial f_0}{\partial s}\right) = S. \tag{4.36}$$

Here, by D_{xx} we denoted the spatial diffusion coefficient along the magnetic field defined through:

$$D_{xx} = \frac{v^2}{8}\int_{-1}^{1} \frac{(1-\mu^2)^2}{D_{\mu\mu}} d\mu. \tag{4.37}$$

In the QL approximation, using Eqs. 4.31 and 4.32 one can obtain a closed form of Eq. 4.37, which is:

$$D_{xx} = \frac{v\, p^2}{4\pi\,(eZ_i)^2}\int_{-1}^{1} \frac{(1-\mu^2)\,|\mu|}{\sum_\sigma I_\sigma\left(\frac{\omega_{ci}}{v|\mu|}\right)} d\mu, \tag{4.38}$$

where ω_{ci} is the ions' cyclotron frequency. In terms of an integral by the turbulence spectrum, the spatial diffusion coefficient can be written as:

$$D_{xx} = \frac{vB^2}{4\pi}\sum_{g_\sigma=\pm 1}\int_{k_r}^{\infty} \frac{dk\,(k^2-k_r^2)}{k^5\sum_{V_\sigma=\pm V_A} I_\sigma(k)}, \tag{4.39}$$

where the resonant wave number, k_r, is the inverse of the Larmor radius, i.e., $k_r = eZ_iB/p$.

One can also use Eq. 4.34 to evaluate the pitch-angle dependence of the distribution function in the expression for the wave growth rate (see Eq. 4.25). Again, by neglecting the difference between μ and μ_σ, one obtains:

$$\gamma_\sigma = 2\pi \int dp d\mu p^2 (1-\mu^2) \left(-kv^2 \frac{1-\mu^2}{2D_{\mu\mu}} \frac{\partial f_0}{\partial s} \right) K_\sigma(k, \omega, \mathbf{p}). \tag{4.40}$$

In the QL limit, using Eq. 4.31 this becomes:

$$\gamma_\sigma = -\frac{\pi V_\sigma}{\varepsilon_0 c^2 |k| \sum_{\sigma', g_{\sigma'} = g_\sigma} I_{\sigma'}(k)} \int\limits_{p_{res}(k)}^{\infty} dp p^3 \frac{p_{res}(k)}{m_i} \left(1 - \frac{p_{res}^2(k)}{p^2} \right) \frac{\partial f_0}{\partial s}, \tag{4.41}$$

where the resonant value of momentum, p_{res}, for a given k, is defined as $p_{res}(k) = m_i \omega_{ci}/k$.

CHAPTER V

MHD Modeling

5.1 Alfvén Wave Turbulence Driven MHD Description of the Solar Corona and the Solar Wind

5.1.1 Steady-State Solar Corona and Solar Wind

In any predictive model for eruptive solar events, the background steady-state SC and IH are as important as a stage for a performance. If poorly designed, the foundation would compromise the whole facility. Thus, an accurate and carefully validated model for the steady-state background is vital and shouldn't be overlooked or explored superficially. In our work we use a widely accepted paradigm that the solar wind is driven by and the SC is heated by the dissipation in, the Alfvén wave turbulence.

5.1.1.1 Alfvén wave turbulence

The concept of Alfvén waves was introduced more than 70 years ago by *Alfvén* (1942). The importance of the role they play within the Solar system was not immediately recognized due to lack of relevant observations. Results from Mariner 2 allowed a data-backed study of a wave-related phenomena in solar wind. A detailed analysis of these observations can be found in, for example, *Coleman* (1966, 1967).

This pioneering study culminated in *Coleman* (1968), a work that stated that Alfvén wave turbulence has the potential to drive solar wind in a way that is consistent with observations at 1 AU.

Attention to Alfvén waves related phenomena was continuously increasing and an ever growing number of studies on interaction of these waves with solar wind plasma and various aspects of associated effects were undertaken. Examples of the earliest efforts to investigate the role of Alfvén waves in solar wind acceleration are *Belcher et al.* (1969); *Belcher and Davis* (1971); *Alazraki and Couturier* (1971). A consistent and comprehensive theoretical description of Alfvén wave turbulence and its effect on the averaged plasma motion has been developed in a series of works, particularly, *Dewar* (1970) and *Jacques* (1977, 1978) (see also references therein). More recent efforts to simulate solar wind acceleration utilize the approach developed in these works (e.g. *Usmanov et al.*, 2000). Currently, it is commonly accepted, that the gradient of the Alfvén wave pressure is the key driver for the solar wind acceleration.

At the same time, damping of Alfvén wave turbulence as a source of the coronal heating was extensively studied (e.g. *Barnes*, 1966, 1968). Later, it was demonstrated that reflection from the sharp pressure gradients in the solar wind (*Heinemann and Olbert*, 1980; *Leroy*, 1980) is a critical component of Alfvén wave turbulence damping (*Matthaeus et al.*, 1999; *Dmitruk et al.*, 2002; *Verdini and Velli*, 2007). For this reason, many numerical models explore the generation of reflected counter-propagating waves as the underlying cause of the turbulence energy cascade (e.g. *Cranmer*, 2010), which transports the energy of turbulence from the large scale motions across the *inertial range* of the turbulence spatial scale to short-wavelength perturbations. The latter can efficiently damp due to the wave-particle interaction. In this way, the turbulence energy is converted to the particle (thermal) energy.

Recent efforts of many studies are aimed at developing models that include Alfvén waves as a primary driving agent for both heating and accelerating of the solar wind.

Examples are *Hu et al.* (2003); *Suzuki and Inutsuka* (2005); *Verdini et al.* (2010); *Matsumoto and Suzuki* (2012); *Lionello et al.* (2014a,b).

It is important to emphasize, that while incorporating the Alfvén wave driven acceleration is a matter of including the wave pressure gradient into governing equations (*Jacques*, 1977), there is still no widely accepted approach to describing the coronal heating via Alfvén wave turbulence cascade. Because of this, the next section is devoted to reviewing certain existing treatments of the problem.

5.1.1.2 Ad Hoc Coronal Heating Functions and Semi-Empirical Models for the Solar Wind Heating

A large number of models of solar corona heating have been constructed over the years. One can trace two major approaches to representing the process: (i) to use an ad-hoc heating function to mimic SC heating with heating rate being chosen to better fit observations; (ii) to use a semi-empirical coronal heating function that is based on aspects of physics of Alfvén waves.

The former approach is utilized, for example, by *Lionello et al.* (2001, 2009); *Riley et al.* (2006); *Titov et al.* (2008); *Downs et al.* (2010). This method provides a reasonably good agreement with observations in EUV, X-rays and white light. The agreement looks particularly impressive for the PSI predictions about the solar eclipse image (*Mikić et al.*, 2007). An important limitation is that models utilizing an ad-hoc approach depend on a few free parameters, which need to be determined for various solar conditions. Such approach has an inherent shortcoming: although it is well-suited for typical conditions, it can't properly account for unique conditions as those that can take place during extreme solar events.

Another illustration of the *ad hoc* approach is the semi-empirical model to simulate solar wind. For example, the Wang-Sheeley-Arge (WSA) model instead of incorporating physical properties of Alfvén waves, utilizes semi-empirical formulae

that relate the solar wind speed with the solar magnetogram and the properties of the magnetic field lines of the potential magnetic field as recovered from the synoptic magnetogram. Its development history may be traced through *Wang and Sheeley* (1990, 1992, 1995); *Arge and Pizzo* (2000); *Arge et al.* (2003). The major benefit of the model is the opportunity to seamlessly integrate it into a global space weather simulation as was done in *Cohen et al.* (2007a). In this study, the WSA formulae were used as the boundary condition for the MHD simulator via the varied polytropic gas index distribution (see *Roussev et al.*, 2003b). Models mentioned above successfully explain observations of the solar wind parameters at 1 AU.

A number of validation and comparison studies have been published (*Owens et al.*, 2008; *Vásquez et al.*, 2008; *MacNeice*, 2009; *Norquist and Meeks*, 2010; *Gressl et al.*, 2014; *Jian et al.*, 2015; *Reiss et al.*, 2016). However, these models don't fully capture the physics of Alfvén wave turbulence or even disregard it altogether. Even though some models are designed to account for the Alfvén waves' physics (such as *Cohen et al.*, 2007b), neither does capture every aspect of the interaction of the turbulence with the background flow, which include both energy and momentum transfer from the turbulence to the solar wind plasma. Thus, neither model can be used as a fully consistent tool for simulating the solar atmosphere.

5.1.1.3 Alfvén-Wave-Turbulence-Based Model for the Solar Atmosphere

The *ad hoc* elements were eliminated from the model for the SC and quiet-time IH by *Sokolov et al.* (2013). In the AWSoM the plasma is heated by the dissipation of the Alfvén wave turbulence, and the dissipation, in turn, is generated by the nonlinear interaction between oppositely propagating waves (*Hollweg*, 1986). Within the coronal holes, there are no closed magnetic field lines, hence, there are no oppositely propagating waves. Instead, a weak reflection of the outward propagating waves locally generates sunward propagating waves as quantified by *van der Holst*

et al. (2014). The small power in these locally generated (and almost immediately dissipated) inward propagating waves leads to a reduced turbulence dissipation rate in coronal holes, naturally resulting in the bimodal solar wind structure. The over-expanding field near the edge of the coronal hole remains critical to the development of the slow wind. Another consequence is that coronal holes look like cold black spots in the EUV and X-rays images, while the closed field regions are hot and bright, and the brightest are active regions, near which the wave reflection is particularly strong (see *Sokolov et al.*, 2013; *Oran et al.*, 2013; *van der Holst et al.*, 2014).

The model equations are the following:

$$\frac{\partial \rho}{\partial t} + \nabla \cdot (\rho \mathbf{u}) = 0, \tag{5.1}$$

$$\frac{\partial \mathbf{B}}{\partial t} + \nabla \cdot (\mathbf{u}\mathbf{B} - \mathbf{B}\mathbf{u}) = 0, \tag{5.2}$$

$$\frac{\partial (\rho \mathbf{u})}{\partial t} + \nabla \cdot \left(\rho \mathbf{u}\mathbf{u} - \frac{\mathbf{B}\mathbf{B}}{\mu_0} \right) + \nabla \left(P_i + P_e + \frac{B^2}{2\mu_0} + P_A \right) = -\frac{G M_\odot \rho \mathbf{R}}{R^3}, \tag{5.3}$$

$$P_A = \frac{1}{2}(w_+ + w_-) \tag{5.4}$$

The notation used in the equations is as follows: ρ is the mass density, $\mathbf{u}$ is the velocity, $u = |\mathbf{u}|$, assumed to be the same for the ions and electrons, $\mathbf{B}$ is the magnetic field, $B = |\mathbf{B}|$, G is the gravitational constant, $M_\odot$ is the solar mass, $\mathbf{r}$ is the position vector relative to the center of the Sun, $R = |\mathbf{R}|$, μ_0 is the magnetic permeability of vacuum. As has been shown by *Jacques* (1977), the Alfvén waves exert an *isotropic* pressure (see term ∇P_A in the momentum equation). Herewith, P_A is the wave pressure, $w_\pm$ are the energy densities for the turbulent waves propagating along the magnetic field vector (w_+) or in the opposite direction (w_-). The isotropic ion pressure P_i and

electron pressure P_e are governed by the energy equations:

$$\frac{\partial}{\partial t}\left(\frac{P_i}{\gamma-1}+\frac{\rho u^2}{2}+\frac{\mathbf{B}^2}{2\mu_0}\right)+\nabla\cdot\left\{\left(\frac{\rho u^2}{2}+\frac{\gamma P_i}{\gamma-1}+\frac{B^2}{\mu_0}\right)\mathbf{u}-\frac{\mathbf{B}(\mathbf{u}\cdot\mathbf{B})}{\mu_0}\right\}=$$
$$=-(\mathbf{u}\cdot\nabla)\left(P_e+P_A\right)+\frac{N_eN_ik_B}{\gamma-1}\left(\frac{\nu_{ei}}{N_i}\right)(T_e-T_i)-\frac{GM_\odot\rho\mathbf{R}\cdot\mathbf{u}}{R^3}+Q_i, \quad (5.5)$$

$$\frac{\partial\left(\frac{P_e}{\gamma-1}\right)}{\partial t} + \nabla\cdot\left(\frac{P_e}{\gamma-1}\mathbf{u}\right)+P_e\nabla\cdot\mathbf{u}=$$
$$= -P_e\nabla\cdot\mathbf{u}-\nabla\cdot\mathbf{q}_e+\frac{N_eN_ik_B}{\gamma-1}\left(\frac{\nu_{ei}}{N_i}\right)(T_i-T_e)-Q_{\rm rad}+Q_e, \quad (5.6)$$

where $T_{e,i}$ are the electron and ion temperatures, $N_{e,i}$ are the electron and ion number densities, and k_B is the Boltzmann constant. Other newly introduced terms are explained below.

The equation of state $P_{e,i}=N_{e,i}k_BT_{e,i}$, is used for both species. The polytropic index is $\gamma=5/3$. The optically thin radiative energy loss rate in the lower corona is given by

$$Q_{\rm rad}=N_eN_i\Lambda(T_e) \quad (5.7)$$

where $\Lambda(T_e)$ is the radiative cooling curve taken from the CHIANTI version 7.1 database (*Landi et al.*, 2013, and references therein). The Coulomb collisional energy exchange rate between ions and electrons is defined in terms of the collision frequency

$$\frac{\nu_{ei}}{N_i}=\frac{2\sqrt{m_e}L_C(e^2/\varepsilon_0)^2}{3m_p(2\pi k_BT_e)^{3/2}} \quad (5.8)$$

The electron heat flux $\mathbf{q}_e$ is used in the collisional formulation of *Spitzer and Härm* (1953):

$$\mathbf{q}_e=\kappa_\parallel\mathbf{bb}\cdot\nabla T_e, \quad \kappa_\parallel=3.2\frac{6\pi}{L_C}\sqrt{\frac{2\pi}{m_e}\frac{{\varepsilon_0}^2}{e^2}}\left(k_BT_e\right)^{5/2}k_B \quad (5.9)$$

where m_e and e are the electron mass and charge, m_p is the proton mass, ε_0 is the

vacuum permittivity, $\mathbf{b} = \mathbf{B}/B$, L_C is the Coulomb logarithm.

Dynamics of Alfvén wave turbulence and its interaction with the background plasma requires a special consideration. The evolution of the Alfvén wave amplitude (velocity, $\delta\mathbf{u}$, and magnetic field, $\delta\mathbf{B}$) is usually treated in terms of the *Elsässer* (1950) variables, $\mathbf{z}_\pm = \delta\mathbf{u} \mp \frac{\delta\mathbf{B}}{\sqrt{\mu_0\rho}}$. The Wentzel-Kramers-Brillouin (WKB) approximation is used to derive the equations that govern transport of Alfvén waves, which may be reformulated in terms of the wave energy densities, $w_\pm = \rho\mathbf{z}_\pm^2/4$. Dissipation of Alfvén waves, $\Gamma_\pm w_\pm$, is crucial in driving the solar wind and heating the coronal plasma. The dissipation occurs, when two counter-propagating waves interact. Therefore, an efficient source of both types of waves is needed which is maintained by Alfvén wave reflection from steep density gradients. For this reason, we need to go beyond the WKB approximation that assumes that wavelength is much smaller than spatial scales in the background. Equation describing propagation of the turbulence, its dissipation and reflection has been derived in *van der Holst et al.* (2014):

$$\frac{\partial w_\pm}{\partial t} + \nabla\cdot[(\mathbf{u} \pm \mathbf{V}_A)w_\pm] + \frac{w_\pm}{2}(\nabla\cdot\mathbf{u}) = -\Gamma_\pm w_\pm \mp \mathcal{R}\sqrt{w_- w_+}. \tag{5.10}$$

Here, the dissipation rate equals $\Gamma_\pm = \frac{2}{L_\perp}\sqrt{w_\mp/\rho}$ and the reflection coefficient is given by

$$\begin{aligned}\mathcal{R} = \min\left\{\sqrt{(\mathbf{b}\cdot[\nabla\times\mathbf{u}])^2 + [(\mathbf{V}_A\cdot\nabla)\log V_A]^2}, \max(\Gamma_\pm)\right\}\times \\ \times\left[\max\left(1 - \frac{I_{\max}}{\sqrt{w_+/w_-}}, 0\right) - \max\left(1 - \frac{I_{\max}}{\sqrt{w_-/w_+}}, 0\right)\right],\end{aligned} \tag{5.11}$$

where $I_{\max} = 2$ is the maximum degree of the turbulence "imbalance". If $\sqrt{w \pm /w_\mp} < I_{\max}$, then $\mathcal{R} = 0$ and the reflection term is not applied.

Now, knowing the dissipation of the Alfvén turbulence, we are able to write the

expression for ion and electron heating due to turbulence

$$Q_i = f_p \left(\Gamma_- w_- + \Gamma_+ w_+\right), \quad Q_e = (1 - f_p) \left(\Gamma_- w_- + \Gamma_+ w_+\right), \tag{5.12}$$

where $f_p \approx 0.6$ is a fraction of energy dissipated to ions. Finally, to close the system of equations, we use the following boundary condition for the Poynting flux, Π:

$$\frac{\Pi}{B} = \frac{\Pi_{R_\odot}}{B_{R_\odot}} = \text{const} \approx 1.1 \cdot 10^6 \frac{\text{W}}{\text{m}^2\text{T}} \tag{5.13}$$

The scaling law for the transverse correlation length:

$$L_\perp \sim B^{-1/2}, \quad 100\text{km} \cdot \text{T}^{1/2} \leq L_\perp \sqrt{B} \leq 300\text{km} \cdot \text{T}^{1/2} \tag{5.14}$$

5.1.2 Alfvén-Wave-Turbulence-Based Model for the Solar Atmosphere in Real Time.

AWSoM has been demonstrated to be an accurate tool for modeling realistic conditions of solar wind (*Sokolov et al.*, 2013; *Oran et al.*, 2013; *van der Holst et al.*, 2014). However, in terms of computational efficiency, the model is somewhat restrictive. The reason for that deficiency is the extremely fine resolution of the computational mesh close to the solar surface; such fine mesh is needed to resolve the dynamics of Alfvén wave turbulence and ensure the numerical stability. An alternative approach is to reformulate the mathematical problem in the said region. Instead of solving a computationally expensive 3-D problem on such fine grid, we substitute it with a multitude of much simpler 1-D problems along *threads*, that allow bringing boundary conditions up from the solar surface to a height defined by the assumptions below and are the key concept of our Threaded-Field-Line-Model (TFLM).

The main assumption in the reformulated problem is that the solar magnetic field may be considered to be potential with high accuracy in a certain range of radii,

$R_\odot < R < R_b$. A thread represents a field line of such field. A 1-D problem being introduced here, concerns a flux tube that encloses the thread. Reduction from 3-D to 1-D is summarized below, for more details we refer readers to *Sokolov et al.* (2016). Due to the constraint on the magnetic field divergence, $\nabla \cdot \mathbf{B} = 0$, the magnetic flux remains constant along the thread:

$$B(s) \cdot A(s) = \text{const}, \tag{5.15}$$

hereafter s is the distance along the field line, B is the magnitude of the magnetic field, A is the cross-section area of the flux tube in the consideration. Conservation laws are also greatly simplified due to the fact that in low-beta plasma, velocity is aligned with the magnetic field. Here, assuming steady-state, conservation laws take the form:

Continuity equation:

$$\frac{\partial}{\partial s}\left(\frac{\rho u}{B}\right) = 0 \quad \Rightarrow \quad \left(\frac{\rho u}{B}\right) = \text{const} \tag{5.16}$$

Conservation of momentum:

$$\frac{\partial P}{\partial s} = -\frac{b_R G M_\odot \rho}{R^2} \quad \Rightarrow \quad P = P_{TR} e^{\int_{R_{TR}}^{R} \frac{G M_\odot m_p}{2 k_B T} d\frac{1}{R'}}, \tag{5.17}$$

here R_{TR} is the height of the transition region (TR), b_R is the radial component of $\mathbf{b}$ terms proportional to u^2 are neglected, $\mathbf{j} \times \mathbf{B}$ is omitted due to current vanishing in the potential field ($\mathbf{j} \propto \nabla \times \mathbf{B} = 0$) and pressure of Alfvén wave turbulence is assumed to be much smaller than the thermal pressure, $P_A \ll P$.

Conservation of energy:

$$\frac{2N_i k_B}{B\left(\gamma-1\right)}\frac{\partial T}{\partial t}+\frac{2k_B\gamma}{\gamma-1}\left[\frac{N_i u}{B}\right]\frac{\partial T}{\partial s}= \\ \frac{\partial}{\partial s}\left(\frac{\kappa_\parallel}{B}\frac{\partial T}{\partial s}\right)+\frac{\Gamma_- w_- +\Gamma_+ w_+ - N_e N_i \Lambda(T)}{B}+\left[\frac{\rho u}{B}\right]\frac{\partial\left(GM_\odot/R\right)}{\partial s}, \tag{5.18}$$

the term $\frac{\partial T}{\partial t}$ is retained under assumption that the electron heat conduction is a relatively slow process. Alfvén wave dynamics needs to be reformulated as well. In Eq. 5.10 we substitute $w_\pm = \left[\frac{\Pi}{B}\right]\sqrt{\mu_0\rho}a_\pm^2$:

$$\frac{\partial a_\pm^2}{\partial t}+\nabla\cdot\left(\mathbf{u}a_\pm^2\right)\pm\left(\mathbf{V}_A\cdot\nabla\right)a_\pm^2 = \mp\mathcal{R}a_- a_+ - 2\sqrt{\frac{\left[\Pi/B\right]\mu_0 V_A}{\left[L_\perp\sqrt{B}\right]^2}}a_\mp a_\pm^2 \tag{5.19}$$

The equations are additionally simplified since in the lower corona environment $u \ll V_A$, i.e. waves are assumed to travel fast and quickly converge to equilibrium, $\frac{\partial a_\pm^2}{\partial t}=0$:

$$\pm\left(\mathbf{b}\cdot\nabla\right)a_\pm^2 = \mp\frac{\mathcal{R}}{V_A}a_- a_+ - 2\sqrt{\frac{\left[\Pi/B\right]\mu_0}{\left[L_\perp\sqrt{B}\right]^2 V_A}}a_\mp a_\pm^2 \tag{5.20}$$

Additionally, we substitute $d\xi = ds\sqrt{\frac{[\Pi/B]\mu_0}{\left[L_\perp\sqrt{B}\right]^2 V_A}}$:

$$\pm\frac{da_\pm}{d\xi} = \mp\frac{ds}{d\xi}\frac{\mathcal{R}}{2V_A}a_\mp - a_- a_+ \tag{5.21}$$

In order to close the system of equations we need to define the boundary conditions for TFLM. For "+" wave one needs to provide value at $\xi=\xi_-$, a_{+0}, and for "-" wave - value at $\xi=\xi_+$, a_{-0}. Boundary conditions at the interface between TFLM and

global corona model (GCM) are:

$$
\begin{aligned}
b_r|_{R=R_b} > 0 \quad : \qquad & \left(\frac{u}{B}\right)_{TFLM} = \quad \left(\frac{\mathbf{u}}{B^2}\cdot\mathbf{B}\right)_{GCM}; \\
& (a_-)_{TFLM} = (a_-)_{GCM}\,; \quad (a_+)_{GCM} = (a_+)_{TFLM} \\
b_r|_{R=R_b} < 0 \quad : \qquad & \left(\frac{u}{B}\right)_{TFLM} = -\left(\frac{\mathbf{u}}{B^2}\cdot\mathbf{B}\right)_{GCM}; \\
& (a_-)_{TFLM} = (a_+)_{GCM}\,; \quad (a_-)_{GCM} = (a_+)_{TFLM}
\end{aligned}
\tag{5.22}
$$

Also one needs to sew temperature and density across the interface between TFLM and GCM. We assume that the radial component of the temperature gradient is the dominant one, then:

$$
\left(\frac{\partial T}{\partial R}\right)_{GCM} = \left(\frac{\partial T}{\partial s}\right)_{TFLM} / \left|b_R\right| \tag{5.23}
$$

Boundary condition for density is controlled by sign of u:

$$
\begin{aligned}
\text{for} \quad u > 0 \quad : \qquad & \left(\frac{N_i u}{B}\right)_{TFLM} = (N_i)_{TFLM}\left(\frac{u}{B}\right)_{GCM}; \\
\text{for} \quad u < 0 \quad : \qquad & \left(\frac{N_i u}{B}\right)_{TFLM} = \left(\frac{N_i u}{B}\right)_{GCM}.
\end{aligned}
\tag{5.24}
$$

Now we close the problem by stating conditions at the lower boundary, i.e. at the top of TR. Assuming steady-state, the energy conservation equation with only dominant terms retained reads:

$$
\frac{\partial}{\partial s}\left(\kappa_0 T^{5/2}\frac{\partial T}{\partial s}\right) = N_e N_i \Lambda(T) \tag{5.25}
$$

For a chosen width of TR along the field line, $L_{TR} = \int_{r_\odot}^{r_{TR}} ds$, and for a given temperature on top of the TR, T_{TR}, one can solve the heat flux and pressure from the

following equations:

$$\begin{aligned} [N_i k_B T] &= \frac{1}{L_{TR}} \int_{T_{ch}}^{T_{TR}} \frac{\kappa_0 \tilde{T}^{5/2} d\tilde{T}}{U_{\rm heat}(\tilde{T})} \\ \kappa_0 T_{TR}^{5/2} \left(\frac{\partial T}{\partial s} \right)_{T=T_{TR}} &= [N_i k_B T] U_{\rm heat}(T_{TR}) \end{aligned} \tag{5.26}$$

$\Lambda(T)$ and $U_{\rm heat}(T) = \sqrt{\frac{2}{k_B^2} \int_{T_{ch}}^{T} \kappa_0 (T')^{1/2} \Lambda(T') dT'}$ are easy to tabulate using CHIANTI database.

Thus, TFLM is fully described as a closed mathematical problem that can be solved numerically.

5.2 CME Models in Numerical Simulations

As mentioned above, the focus of our work are so called gradual SEP events. Events of this kind are characterized by a particle flux steadily increasing over several hours and maintaining a value above normal over the span of several days, unlike impulsive events, which have an abrupt time profile (*Reames*, 1999). Based on numerous observations (*Kahler et al.*, 1978), it is commonly accepted that gradual, proton-rich SEP events are associated with CMEs. The two phenomena are linked via interplanetary shock wave, which forms in front of a CME: the shock wave itself results from interaction of a CME with ambient solar wind plasma and at the same time, as shock moves outwards, it accelerates particles that it encounters along its path, hence the gradual nature of events.

Thus, properties of gradual SEP events are strongly influenced by CMEs that trigger them. Therefore, in order to successfully design a predictive model for gradual SEP events, we need an accurate model to describe CMEs. Due to the lack of in-situ measurements of the shock waves and the excited turbulence in their vicinity, numerical simulations remain the primary means of research. A series of numerical

studies employing the theory of DSA were performed in cases of both idealized (*Zank et al.*, 2000; *Rice et al.*, 2003; *Li et al.*, 2003) and realistic (*Sokolov et al.*, 2004; *Kóta et al.*, 2005a) CME-driven shock waves.

While there are many models of CME initiation by magnetic free energy, these simulations are often performed in a small Cartesian box (e.g. *Török and Kliem*, 2005), or using global models with no solar wind (e.g. *Antiochos et al.*, 1999; *Fan and Gibson*, 2004). So far, there have only been a few magnetically driven Sun-to-Earth CME simulations through a realistic interplanetary medium using 3-D MHD (cf. *Manchester et al.*, 2004b; *Manchester et al.*, 2005; *Lugaz et al.*, 2007a; *Tóth et al.*, 2007). The MHD simulation of *Tóth et al.* (2007) was able to match the CME arrival time to Earth within 1.8 hours and reproduce the magnetic field magnitude of the event.

Observations of halo CMEs (e.g. with LASCO instrument, *Brueckner et al.*, 1995; *Plunkett et al.*, 1998) provided new insights into the geometry of CMEs and its relation with other properties. One can accurately infer the angular width and the central position angle of a halo CME together with the plasma velocity. For example, these observations have revealed that: (i) the bulk velocity tends to be radial; (ii) the angular width, $2\Delta\theta$, tends to remain constant as CME propagates through the corona. These persistent features lead to the development of the cone model (*Zhao et al.*, 2002). Having only three free parameters, angular width of a CME and its initial position on the solar surface, the model approximates a CME and its propagation with a cone with apex located at the center of the Sun. It was later improved by *Michalek* (2006) for arbitrary shapes. The cone model is successfully used at Community Coordinated Modeling Center (CCMC) and has proved to be an efficient tool for predicting arrival times of CMEs (*Vršnak et al.*, 2014; *Mays et al.*, 2015). It is commonly used together with WSA model. However, by design, the cone model lacks details about the magnetic field carried by a CME. The model may be improved, as

we show below in this Chapter.

A simple but convenient way to simulate a magnetically-driven CME is to superimpose a *Gibson and Low* (1998) (GL) or *Titov and Démoulin* (1999) (TD) magnetic flux-tube configuration onto the background state of the SC. These magnetic configurations describe an erupting magnetic filament filled with excessive plasma density. That filament becomes an expanding flux rope (magnetic cloud) in the ambient solar wind while evolving and propagating outward from the Sun, thus allowing the simulation of the propagation to 1 AU of a magnetically driven CME (*Manchester et al.*, 2004a, 2014). We provide a detailed description of GL configuration, since we extensively utilize it for initiating eruptive events (see Chapter VI), and briefly discuss TD configuration.

5.2.1 Equilibrium Magnetic Configurations: Spheromak

The starting point of constructing a pre-eruptive flux rope is equations of MHD equilibrium (*Landau and Lifshitz*, 1960):

$$\mathbf{j} \times \mathbf{B} - \nabla P = 0, \tag{5.27}$$

which we consider in spherical coordinates (r, θ, φ). Herewith, $\mathbf{B}(r, \theta, \varphi)$ is the vector of magnetic field and $P(r, \theta, \varphi)$ is the plasma pressure. However, it has been demonstrated (*Grad and Rubin*, 1958; *Shafranov*, 1966) that an axisymmetric equilibrium MHD configuration is governed by a single scalar equation, commonly referred to as the Grad-Shafranov equation. The key concept that allows transforming Eq. 5.27 to this simpler form is that of *magnetic surfaces*, which are defined as surfaces of constant pressure, P.

From Eq. 5.27, $\mathbf{j} \cdot \nabla P = 0$ and $\mathbf{B} \cdot \nabla P = 0$, i.e. a single line of either magnetic field, or electric current is entirely confined within a single magnetic surface. Further,

magnetic field flux and current functions defined as

$$\begin{aligned} \psi\left(r_{\perp},z\right) &= \int_{0}^{r_{\perp}} B_z(r'_{\perp},z)r'_{\perp}dr'_{\perp} \\ I\left(r_{\perp},z\right) &= \int_{0}^{r_{\perp}} j_z(r'_{\perp},z)r'_{\perp}dr'_{\perp} \end{aligned} \tag{5.28}$$

can both be demonstrated to be constant on a given magnetic surface (herewith, $r_{\perp} = r\sin\theta$ and $z = r\cos\theta$). Therefore, for an axisymmetric equilibrium configuration, there is a functional dependence between ψ, I and P: $I{=}I(\psi)$, $P{=}P(\psi)$. Using Ampere's law, $\nabla\times\mathbf{B} = \mu_0\mathbf{j}$, and by introducing the toroidal component of the vector potential, $\nabla\times\mathbf{A} = \mathbf{B}$, one can relate the current and magnetic flux via the toroidal components of the field and vector potential: $I = \frac{r_{\perp}}{\mu_0}B_{\varphi}$, $\psi = r_{\perp}A_{\varphi}$. Thus, the total magnetic field may be expressed as:

$$\mathbf{B} = \nabla\times\left(A_{\varphi}\mathbf{e}_{\varphi}\right) + B_{\varphi}\mathbf{e}_{\varphi} = \frac{1}{r_{\perp}}\left(\nabla\psi\times\mathbf{e}_{\varphi} + \mu_0 I\mathbf{e}_{\varphi}\right) \tag{5.29}$$

Herewith, $\mathbf{e}_{\varphi}$ is the unit vector of the azimuthal (toroidal) direction. Analogously, for the current density vector we have:

$$\mu_0\mathbf{j} = \nabla\times\left[\nabla\times\left(A_{\varphi}\mathbf{e}_{\varphi}\right) + B_{\varphi}\mathbf{e}_{\varphi}\right] = -\nabla^2\left(A_{\varphi}\mathbf{e}_{\varphi}\right) + \mu_0\frac{dI}{d\psi}\frac{\nabla\psi\times\mathbf{e}_{\varphi}}{r_{\perp}} \tag{5.30}$$

Once substitutions Eq. 5.29 and Eq. 5.30 are performed and a common factor of $\frac{\nabla\psi}{r_{\perp}}$ is omitted, the condition of equilibrium, Eq. 5.27, reads

$$\mathbf{e}_{\varphi}\cdot\nabla^2(A_{\varphi}\mathbf{e}_{\varphi}) = -\mu_0 r_{\perp}\frac{dP}{d\psi} - \mu_0\frac{dI}{d\psi}B_{\varphi}. \tag{5.31}$$

In the particular case of constant $\frac{dI}{d\psi}$ and $\frac{dP}{d\psi}$, by expressing the Laplace operator in spherical coordinates Eq. 5.31 reduces to the equation describing electro-magnetic

waves (magnetic dipole and multipole harmonics - see *Jackson*, 1999):

$$\frac{1}{r^2}\frac{\partial}{\partial r}\left(r^2\frac{\partial A_\varphi}{\partial r}\right)+\frac{1}{r^2\sin\theta}\frac{\partial}{\partial\theta}\left(\sin\theta\frac{\partial A_\varphi}{\partial\theta}\right)-\frac{A_\varphi}{r^2\sin^2\theta}+\alpha_0^2A_\varphi=-\mu_0 r\sin\theta\frac{dP}{d\psi} \quad (5.32)$$

where $\alpha_0 = \mu_0 dI/d\psi$. It may be solved by developing the solution over spherical harmonics: $A_\varphi = \sum_{n=1}^{\infty} c_n j_n(\alpha_0 r) P_n^1(\cos\theta) - \mu_0\alpha_0^{-2} r\sin\theta\frac{dP}{d\psi}$, where $j_n(x) = \sqrt{\frac{\pi}{2x}}J_{n+1/2}(x)$, $J_\nu(x)$ and $j_n(x)$ are regular and spherical Bessel functions respectively. For a dipole harmonic we have:

$$A_\varphi = A_{\varphi 0}\left[j_1(\alpha_0 r)-\frac{\mu_0 r}{\alpha_0^2 A_{\varphi 0}}\frac{dP}{d\psi}\right]\sin\theta \quad (5.33)$$

In application to the solar corona the solution with the low plasma β is of a particular interest. In the first approximation, $dP/d\psi = 0$, the force-free solution is as follows:

$$\begin{aligned} B_\varphi &= \alpha_0 A_\varphi = B_0 j_1(\alpha_0 r)\sin\theta, \\ B_r &= \frac{1}{r\sin\theta}\frac{\partial}{\partial\theta}(\sin\theta A_\varphi) = B_0\frac{2}{\alpha_0 r}j_1(\alpha_0 r)\cos\theta, \\ B_\theta &= -\frac{1}{r}\frac{\partial}{\partial r}(rA_\varphi) = B_0\left[j_2(\alpha_0 r)-\frac{2}{\alpha_0 r}j_1(\alpha_0 r)\right]\sin\theta, \end{aligned} \quad (5.34)$$

where $j_1(x) = \frac{\sin x}{x^2} - \frac{\cos x}{x}$, $j_2(x) = \frac{3j_1(x)}{x} - \frac{\sin x}{x}$, $B_0 = \alpha_0 A_{\varphi 0}$. In the third of Eqs. 5.34 the identity, $\frac{d}{dx}\left(\frac{j_n(x)}{x^n}\right) = -\frac{j_{n+1}(x)}{x^n}$, has been applied. The solution is valid within the sphere on which the radial component of the field vanishes, i.e. $j_1(\alpha_0 r_0)$=0, hence $\alpha_0 \approx 4.49/r_0$. At the boundary, B_φ also vanishes, while non-zero B_θ matches the external field (see below in this Chapter), which prevents the configuration from being disrupted by the hoop force.

To include a low non-zero pressure into consideration, the following expression may be used: $P = r_\perp A_\varphi\frac{dP}{d\psi} = P_0\alpha_0 r\sin\theta(B_\varphi/B_0)$, where $P_0 = \beta_0 B_0^2/\mu_0$ and $\beta_0 = \frac{\mu_0}{B_0\alpha_0^2}\frac{dP}{d\psi}$.

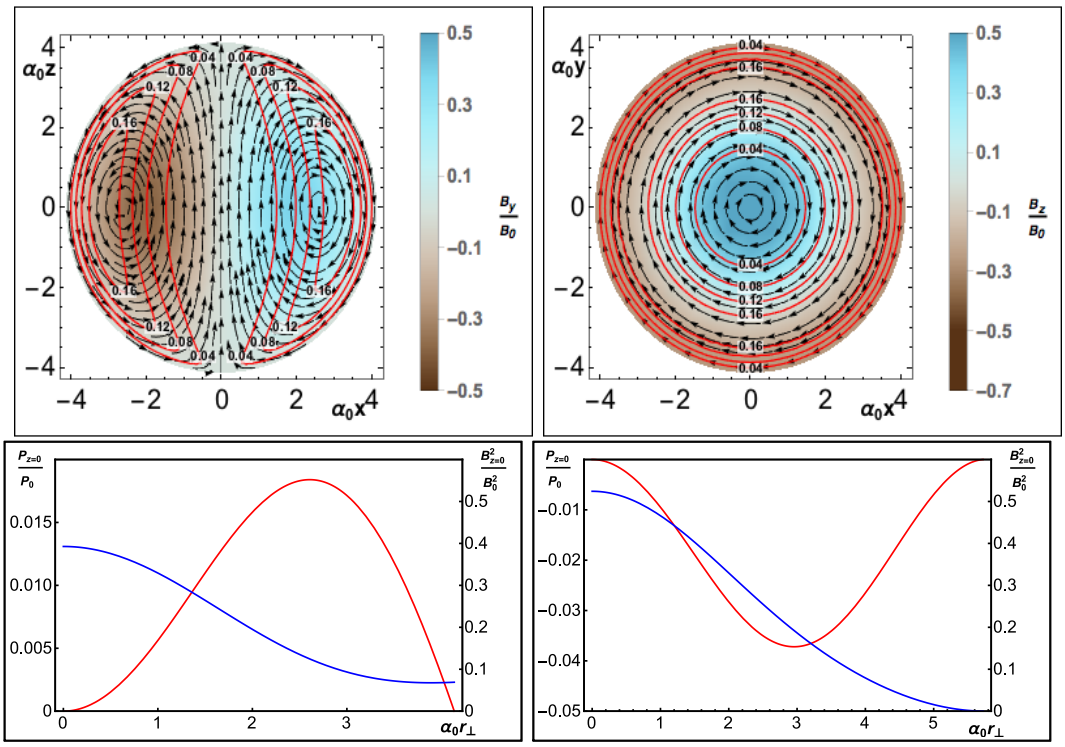

Figure 5.1: **Top:** spheromak configuration for β_0=0.02: meridional (**left**) and equatorial (**right**) planes. Magnetic field direction is marked with arrows, off-plane component of the magnetic field is normalized per B_0 and shown by color. Local values of plasma parameter $\beta(\mathbf{r}) = \mu_0 P(\mathbf{r})/B^2(\mathbf{r})$ are shown with orange curves corresponding to levels $\beta = 0.04, 0.08, 0.12, 0.16$ as marked explicitly. **Bottom**: radial dependence of thermal pressure, $\mu_0 P(r)/B_0^2$, (red curve) and magnetic pressure, $B^2(r)/B_0^2$, (blue curve) in the equatorial cut z=0: for β_0=0.02 (**left panel**) and for $\beta_0 = -2.87\times10^{-2}$ (**right panel**) .

Now, Eqs. 5.34 may be written with the effect of finite pressure:

$$\mathbf{B}_{\rm sph}(\mathbf{r}) = \left[\frac{j_1(\alpha_0 r)}{\alpha_0 r} - \beta_0\right](2\mathbf{B}_0 \pm \alpha_0[\mathbf{B}_0 \times \mathbf{r}]) + j_2(\alpha_0 r)\frac{[\mathbf{r} \times [\mathbf{r} \times \mathbf{B}_0]]}{r^2} \tag{5.35}$$

$$P_{\rm sph}(\mathbf{r}) = \left[\frac{j_1(\alpha_0 r)}{\alpha_0 r} - \beta_0\right]\frac{\beta_0 \alpha_0^2 [\mathbf{r} \times \mathbf{B}_0]^2}{\mu_0}. \tag{5.36}$$

Herewith, the vector $\mathbf{B}_0$ is introduced with the magnitude equal to B_0 directed along the polar axis of the spherical coordinate system which we won't use from this point on. At the center of configuration the magnetic field equals $\mathbf{B}_{\rm sph}|_{r=0} = 2\left(\frac{1}{3} - \beta_0\right)\mathbf{B}_0$, which only by a numerical factor of ≈0.7 differs from $\mathbf{B}_0$. In Eqs. 5.35-5.36, the

coordinate vector, $\mathbf{r}$, originates at the center of configuration, $\mathbf{R}_{\rm sph}$. In the heliocentric coordinate system we used prior to the current section the coordinate vector had been denoted as $\mathbf{R}$, which is related to $\mathbf{r}$ as $\mathbf{r} = \mathbf{R} - \mathbf{R}_{\rm sph}$. Thus, in the arbitrary coordinate system, the field and pressure of the configuration equal: $\mathbf{B}_{\rm sph}(\mathbf{R}-\mathbf{R}_{\rm sph})$, $p_{\rm sph}(\mathbf{R}-\mathbf{R}_{\rm sph})$, for $\|\mathbf{R}-\mathbf{R}_{\rm sph}\| \leq r_0$.

Once $\mathbf{B}_0$ and $\mathbf{R}_{\rm sph}$ are given, there remains the choice of $\pm$ sign in Eq. 5.35. The upper (+) sign corresponds to the geometry considered above: positive B_0, α_0 and positive B_φ require the current in the configuration to be parallel to the field (positive helicity), while the lower (-) sign corresponds to the negative helicity (the current is anti-parallel to the magnetic field). Alternatively, one may always keep plus sign in Eq. 5.35, in which case the negative helicity would be given by the choice of negative α_0: both $j_1(x)/x$ and $j_2(x)$ are even functions, therefore, the direction of only toroidal component of the magnetic field is affected.

For $\beta_0 \neq 0$ the condition at the external boundary, $\|\mathbf{R}-\mathbf{R}_{\rm sph}\| = r_0$ needs a revision. The radial and toroidal components of the magnetic field turn to zero at the surface, if $j_1(\alpha_0 r_0) - \beta_0 \alpha_0 r_0$. For a given β_0 this equation relates the configuration size, r_0, with the extent of magnetic field twisting, α_0, needed to close the configuration within this size. The plasma pressure, P, also turns to zero at the external boundary.

The meridional and equatorial planes (top) and radial dependence of the field and pressure for β_0=0.02 (bottom left) are shown in Fig. 5.1. The shown magnetic field lines are also the cross-sections of magnetic surfaces.

In *Gibson and Low* (1998) and the papers cited therein the non-trivial choice of *negative* value of β_0 had been proposed (without stating this point explicitly), such that all three components in Eq. 5.35 vanish at $\|\mathbf{R}-\mathbf{R}_{\rm sph}\| = r_0$. Specifically, the choice of $\beta_0 = j_1(\alpha_0 r_0)/(\alpha_0 r_0) \approx -2.87 \cdot 10^{-2}$, where the radius is defined by condition $j_2(\alpha_0 r_0)$=0, i.e. $\alpha_0 r_0 \approx 5.76$, satisfies this criterion. The radial dependency of negative pressure variation in comparison with the magnetic pressure is shown in Fig. 5.1

(bottom right). The advantage of this approach is that it is somewhat simpler to superimpose this configuration onto background with no need to analyze the field outside the configuration. The disadvantage is that the negative variation of pressure within the configuration as in Eq. 5.36 is meaningful only when summed with some positive background pressure, $P_{\text{background}}$, so that the total pressure, $P_{\text{sph}}+P_{\text{background}}$, is positive and realistic. The background pressure distribution may be uniform, thus not contributing to the force balance, or barometric, thus balancing the gravity force not accounted for in Eq. 5.27. To avoid the pressure jump at the boundary, this background pressure should also exist outside the configuration to maintain the force balance, particularly, preventing the configuration disruption by the hoop force.

5.2.2 Magnetized Cone Model

The idea of CME generator is to perturb the existing ("ambient") solution describing the state of the SC and IH magnetic field, $\mathbf{B}_{\text{amb}}(\mathbf{R})$, prior to the eruption by superposing the spheromak configuration around the point, $\mathbf{R}_{\text{sph}}$. For doing this, one needs to account for the field, which the currents *inside* spheromak produce *outside* the boundary, $\|\mathbf{R}-\mathbf{R}_{\text{sph}}\| = r_0$. The calculation of the magnetic moment (see definition in *Jackson*, 1999), $\mathfrak{m}$, of the spheromak configuration gives:

$$\mathfrak{m} = \frac{1}{2}\int\limits_{\|\mathbf{r}\|\le r_0} d^3r[\mathbf{r}\times\mathbf{j}] = \frac{1}{2\mu_0}\int\limits_{\|\mathbf{r}\|\le r_0} d^3r[\mathbf{r}\times[\nabla\times\mathbf{B}_{\text{sph}}]] = \frac{4\pi r_0^3}{3\mu_0} j_2(\alpha_0 r_0)\mathbf{B}_0 \quad (5.37)$$

The final expression for $\mathfrak{m}$ is obtained via reducing the volume integral to the integral over the spheromak's surface, at which $\mathbf{B}_{\text{sph}}|_{r=r_0} = j_2(\alpha_0 r_0)\frac{[\mathbf{r}\times[\mathbf{r}\times\mathbf{B}]]}{r^2}$. The field of magnetic dipole, $\mathfrak{m}$, which we admit as the spheromak's field outside the boundary, equals:

$$\mathbf{B}_{\text{sph},r>r_0}(\mathbf{r}) = \frac{\mu_0}{4\pi r^3}\left\{\frac{3\,(\mathbf{r}\cdot\mathfrak{m})\,\mathbf{r}}{r^2} - \mathfrak{m}\right\} = j_2(\alpha_0 r_0)\frac{r_0^3}{r^3}\left\{\frac{(\mathbf{r}\cdot\mathbf{B}_0)\,\mathbf{r}}{r^2} - \frac{\mathbf{B}_0}{3}\right\} \quad (5.38)$$

Now, we can provide the full expression for superposed field:

$$\mathbf{B}(\mathbf{R}) = \begin{cases} \mathbf{B}_{\rm amb}(\mathbf{R}) + \mathbf{B}_{{\rm sph},r>r_0}(\mathbf{R}-\mathbf{R}_{\rm sph}), & \|\mathbf{R}-\mathbf{R}_{\rm sph}\| \geq r_0 \\ \left[\mathbf{B}_{\rm amb}(\mathbf{R}) + \frac{2}{3} j_2(\alpha_0 r_0)\mathbf{B}_0\right] + \mathbf{B}_{\rm sph}(\mathbf{R}-\mathbf{R}_{\rm sph}), & \|\mathbf{R}-\mathbf{R}_{\rm sph}\| \leq r_0 \end{cases} \tag{5.39}$$

where the uniform field, $\frac{2}{3} j_2(\alpha_0 r_0)\mathbf{B}_0$ is added to the spheromak field for two reasons. First, this preserves the field continuity at $\|\mathbf{R}-\mathbf{R}_{\rm sph}\| = r_0$, i.e. from both side of the boundary the field equals $j_2(\alpha_0 r_0)\left\{\frac{(\mathbf{r}\cdot\mathbf{B}_0)\mathbf{r}}{r^2} - \frac{\mathbf{B}_0}{3}\right\}$. Second, certain aspects of CME ejecta's interaction with ambient plasma dictate this correction. Indeed, if an ejecta represents a *magnetic cloud*, its *frozen in* magnetic field effectively *replaces* the pre-existing field, $\mathbf{B}_{\rm amb}$, at any location, $\mathbf{R}_{\rm cloud}$, it passes. Therefore,the cloud's internal field, which we assume to be the superposition of the ambient field with the field of the spheromak centered at $\mathbf{R}_{\rm cloud}$ (i.e. $\mathbf{R}_{\rm cloud} \equiv \mathbf{R}_{\rm sph}$), must be corrected by the negative of this pre-existing field. This reasoning demands the expression in the square brackets in Eq. 5.39 be exactly zero at $\mathbf{R}_{\rm sph}$, i.e. $\mathbf{B}_0$ and $\mathbf{B}_{\rm amb}$ must be related as:

$$\mathbf{B}_0 = -\frac{3}{2j_2(\alpha_0 r_0)}\mathbf{B}_{\rm amb}(\mathbf{R}_{\rm sph}) \tag{5.40}$$

which ensures both the continuity of the field, Eq. 5.39, and the proximity of the internal field (equality, if the ambient field is uniform), $[\mathbf{B}_{\rm amb}(\mathbf{R}) - \mathbf{B}_{\rm amb}(\mathbf{R}_{\rm sph})] + \mathbf{B}_{\rm sph}(\mathbf{R}-\mathbf{R}_{\rm sph})$, to the equilibrium state $\mathbf{B}_{\rm sph}(\mathbf{R}-\mathbf{R}_{\rm sph})$. Should the field of the superimposed configuration not match the ambient field *in direction*, the non-zero torque, $[\mathfrak{m} \times \mathbf{B}_{\rm amb}(\mathbf{R}_{\rm sph})]$ acting on the magnetic moment, $\mathfrak{m}$, in the field $\mathbf{B}_{\rm amb}(\mathrm{R}_{\rm sph})$, would tend to align the configuration axis with the external field. Should the configuration field is stronger/weaker than that governed by Eq. 5.40, the ambient field would be too weak/strong to balance the hoop force in the spheromak configuration, so that the latter would tend to expand/shrink. The field in the configuration

determined by Eqs. 5.39, 5.40 is oppositely directed and somewhat stronger than the ambient field. For comparison, the field in the center of configuration equals: $\mathbf{B}_{\rm sph}(\mathbf{R}_{\rm sph}) = 2(\frac{1}{3}-\beta_0)\mathbf{B}_0 = -\frac{1-3\beta_0}{j_2(\alpha_0 r_0)}\mathbf{B}_{\rm amb}(\mathbf{R}_{\rm sph})$. Magnetic geometry of the described configuration provides a natural explanation of the geomagnetic activity caused by CMEs. Indeed, if the configuration described above passes the Earth location, the local magnetic field may consequently change from $\mathbf{B}_{\rm amb}(\mathbf{R}_{\rm sph})$ to $\mathbf{B}_{\rm sph}(\mathbf{R}_{\rm sph})$ and back, so that all components of the interplanetary magnetic field change sign and increase in absolute value by a factor of $\frac{(1-3\beta_0)}{j_2(\alpha_0 r_0)} \approx (4-5)$. This is a classical scenario for the magnetospheric storm. Particularly, the cone model by *Zhao et al.* (2002); *Michalek* (2006) may be enriched by incorporating the described configuration field into the model of ejecta, the direction and magnitude of the magnetic field in the configuration being controlled by the ambient external field at the location, $\mathbf{R}_{\rm sph}$, where the CME is added, while the spatial scale of the cloud being among the output parameters of the cone model.

The magnetic cloud described here is at force equilibrium and, in the trivial case, static. However, the presented solution may be used to describe more realistic *self-similar* motion if we assume, and implement in the numerical simulations, the radially diverging initial motion with the radial velocity at each point being proportional to the heliocentric distance: $\mathbf{u}|_{t=0} = \eta\mathbf{R}$, $\eta = \text{const}$. The time evolution of that initial distribution is easy to treat in terms of motion of individual fluid elements, i.e. using Lagrangian formulation of fluid dynamics. As usually, we choose the Lagrangian coordinates for a given fluid element equal to the Eulerian coordinates of this element at the initial time instant, $\mathbf{R}_L = \mathbf{R}|_{t=0}$.

Here, as we consider evolution of the magnetic cloud, we may superimpose a radial velocity profile, $\mathbf{u} = \eta\mathbf{R}_L$, where η is an arbitrary constant. In other words, we force each fluid to move with a constant speed along its trajectory . The real, Eulerian,

coordinates of a fluid element is $\mathbf{R} = (1 + \eta t)\mathbf{R}_L = \Phi(t)\mathbf{R}_L$, i.e.

$$\mathbf{u} = \frac{1}{\Phi}\frac{d\Phi}{dt}\mathbf{R} \tag{5.41}$$

As demonstrated by *Low* (1982), under such conditions and for adiabatic index $\gamma = 4/3$ the magnetic structure evolves *self-similarly* (*Sedov*, 1959; *Zel'dovich and Raizer*, 1967), i.e. with no change in its geometry, provided it is initially at force equilibrium. In application to the magnetized cone model this means that superimposing a spheromak with such velocity profile onto a barometric atmosphere would be consistent with basic principles of the cone model of *Zhao et al.* (2002): (i) bulk velocity of the resulting magnetic cloud is radial, and (ii) geometry of the cloud, due to self-similarity, remains constant.

5.2.3 Stretched Spheromak Configuration by Gibson-Low

The family of solutions for the equilibrium configurations may be extended with the use of *coordinate transformation*. The new equilibrium configuration in the heliocentric coordinates, $\mathbf{R}$, with the magnetic field, $\mathbf{B}(\mathbf{R})$, and pressure distribution, $P(\mathbf{R})$, may be described in terms of the known solutions of the Grad-Shafranov equations, $\mathbf{B}'(\mathbf{R}') = \mathbf{B}_{\rm sph}(\mathbf{R}' - \mathbf{R}_{\rm sph})$ and $P'(\mathbf{R}') = P_{\rm sph}(\mathbf{R}' - \mathbf{R}_{\rm sph})$. For each point, $\mathbf{R}$, we take the values of these functions in the point, $\mathbf{R}'(\mathbf{R}) = \left(1 + \frac{a}{R}\right)\mathbf{R}$, $R' = R + a$, what is radial coordinate stretching, an arbitrary constant a being the distance of stretching. When the stretching transformation is applied, it displaces the magnetic configuration toward the heliocenter and gives it a teardrop-like shape. The magnetic field vector in the course of stretching should be scaled in addition to the coordinate transformation:

$$\mathbf{B}(\mathbf{R}) = \frac{R'}{R}\left(\mathbb{I} + \frac{a}{R}\mathbf{e}_R\mathbf{e}_R\right)\cdot\mathbf{B}'(\mathbf{R}') \tag{5.42}$$

where $\mathbf{e}_R = \mathbf{R}/R$ and $\mathbb{I}$ is the identity matrix. The radial field component, $B'_R = (\mathbf{B}' \cdot \mathbf{e}_R)$, is thus multiplied by $\left(\frac{R'}{R}\right)^2$, all the other by $\frac{R'}{R}$. Thus transformed magnetic field is divergence-free. The plasma pressure of the stretched magnetic configuration is defined as:

$$P(\mathbf{R}) = \left(\frac{R'}{R}\right)^2 \left(P' - \frac{a}{R}\left(2 + \frac{a}{R}\right)\frac{B'^2_R}{2\mu_0}\right) \tag{5.43}$$

One can verify an equilibrium condition for the transformed magnetic configuration. The spatial derivatives of $\mathbf{B}'(\mathbf{R}')$ and $P'(\mathbf{R}')$ are transformed as follows: $\nabla = \left[\left(1 + \frac{a}{R}\right)\mathbb{I} - \frac{a}{R}\mathbf{e}_R\mathbf{e}_R\right] \cdot \nabla'$. Using the equilibrium condition for the non-stretched configuration, $\frac{1}{\mu_0}[[\nabla' \times \mathbf{B}'] \times \mathbf{B}'] - \nabla' P' = 0$, the left hand side of Eq. 5.27 may be reduced to the following form: $\frac{1}{\mu_0}[[\nabla \times \mathbf{B}] \times \mathbf{B}] - \nabla P = F_R \mathbf{e}_R$, where the radial force arising from extra tension of the stretched magnetic field is:

$$F_R = \frac{aR'^2}{R^3}\left[\left(2 + \frac{a}{R}\right)\left(\frac{B'^2}{\mu_0 R'} + (\mathbf{e}_R \cdot \nabla')\left(P' + \frac{B'^2}{2\mu_0}\right)\right) + \frac{2P'}{R'} - \left(3 + 2\frac{a}{R}\right)\frac{B'^2_R}{\mu_0 R}\right] \tag{5.44}$$

Now, one can consider the stretched magnetic configuration described by Eqs. 5.42, 5.43 once superposed with some background barometric distribution of pressure, $P_{\text{bar}}(\mathbf{R})$, and density, $\rho_{\text{bar}}(\mathbf{R})$, which satisfy the hydrostatic equilibrium condition, $-\nabla P_{\text{bar}} + \rho_{\text{bar}}\mathbf{g} = 0$, $\mathbf{g} = -GM_\odot \mathbf{e}_R/R^2$. The superposed distribution satisfies the equilibrium condition accounting for gravity:

$$\frac{1}{\mu_0}[[\nabla \times \mathbf{B}] \times \mathbf{B}] - \nabla(P + P_{\text{bar}}) + (\rho + \rho_{\text{bar}})\mathbf{g} = 0 \tag{5.45}$$

if the density variation due to the effect of stressed field is

$$\rho = \frac{F_R}{g(R)} \tag{5.46}$$

As a result of the transformation, the spherical configuration is stretched towards the heliocenter as shown in Fig. 5.2. When the solution represented by Eq. 5.42, 5.43, 5.46

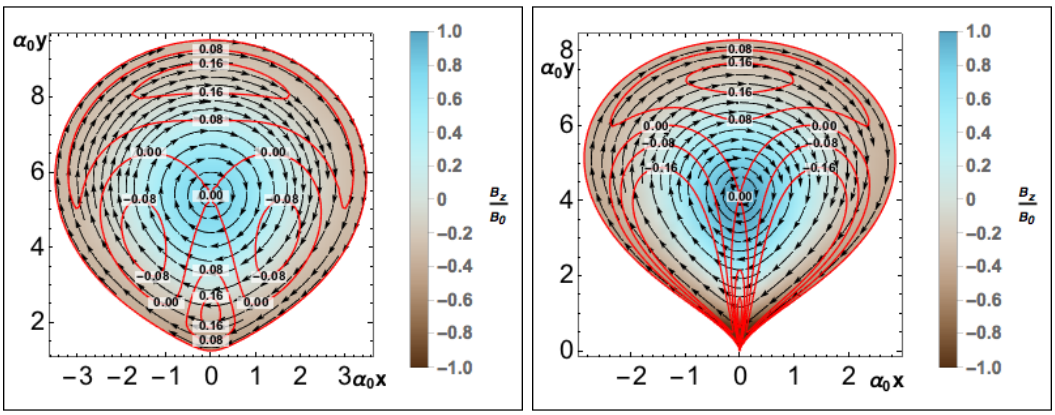

Figure 5.2: Equatorial plane of the stretched flux rope for β_0=0.02 (cf. Fig. 5.1). The original flux rope is shifted by distance $1.6r_0$ along a direction in the equatorial plane and then stretched towards the heliocenter by distance $0.3r_0$ (**left**) and $0.6r_0$ (**right**). The notations are the same as in Fig. 5.1.

is superimposed onto the existing corona, the sharper end of the teardrop shape is submerged below the solar surface. In the wider top part of the configuration ("balloon") the density variation in Eq. 5.46 is *negative*, that is the resulting density is lower than that of the ambient barometric background. As the result, the Archimedes force acting on this part pulls the whole configuration outward the Sun. The cavity with the reduced density is often observed in the CME images from the LASCO coronagraphs. Then, in the narrower bottom part of the configuration ("basket") the excessive *positive* density simulates the dense ejecta, which is pulled outward the Sun by the radial tension in the stretched magnetic configuration. Finally, the tip of the configuration with the magnetic field lines both ingoing and outgoing the solar surface in anchored to the negative and positive magnetic spots of a bipolar AR, considered as the source of the CME. Depending on the reconnection rate, the configuration can either keep being magnetically connected to the AR, or it may disconnect and close and then propagate toward 1 AU as the magnetic cloud.

One may demonstrate that the time evolution of GL flux rope is self-similar (provided $\gamma = 4/3$, see *Low*, 1982). Additionally, this result may be generalized: adjusting the density profile in Eq. 5.46 for effective gravity $g(R) + \alpha R$ and applying a velocity

profile, Eq. 5.41 with $\left(\frac{d\Phi}{dt}\right)^2 = \eta^2 - 2\alpha/\Phi$ would result in accelerated/decelerated propagation of a CME. However, self-similarity of GL flux rope, isn't retained in realistic corona: in order for the configuration to remain at force-equilibrium (or to keep the specific shape of the force imbalance) and therefore propagate in a self-similar fashion, a confining shape needs to have a specific distribution of the external pressure. Realistic coronal plasma doesn't meet this requirement, which leads to the pressure imbalance, the loss of equilibrium and self-similarity. Additionally, since the Ampere's force is non-linear in magnetic field, superimposing GL flux-rope adds a new component, the action of the background magnetic field onto the flux-rope's currents, which contributes even more to the force imbalance. The significance of these effects hasn't been thoroughly studied, however, CME propagation has been shown to be approximately self-similar (e.g. *Manchester et al.*, 2004a,b).

The GL flux rope model has been used for CME initiation in, for example, *Manchester et al.* (2004a,b, 2006); *Lugaz et al.* (2005); *Jin et al.* (2017a,b). Our recent developments allowed us to significantly simplify the process of triggering CMEs using GL model. The product of the effort is the Eruptive Event Generator based on Gibson-Low magnetic configuration (EEGGL) (*Jin et al.*, 2017b).

5.2.4 Thin Flux Rope by Titov-Demoulin

The approach of TD also stems from consideration of the magnetic field's topology. A pre-eruptive configuration of the field is reconstructed with 3 different components, $\mathbf{B}_I$, $\mathbf{B}_q$, $\mathbf{B}_\theta$. $\mathbf{B}_I$ is created by a uniform ring current flowing in the emerging flux rope (later the model has been modified in *Titov et al.* (2014) to include a non-uniform current profile, TDm hereafter), $\mathbf{B}_q$ is the magnetic field of two equal imaginary magnetic charges of opposite signs embedded below the solar surface and, finally, $\mathbf{B}_\theta$ is produced by a constant line current flowing through the said charges.

The TD flux rope model has been used in a number of studies (*Roussev et al.*,

2003a; *Manchester et al.*, 2008, e.g.), as well as its modified version, TDm (*Linker et al.*, 2016). Specific examples of CME simulations using the AWSoM model for the SC and IH with a superimposed TD magnetic configuration include *Manchester et al.* (2012) and *Jin et al.* (2013).

CHAPTER VI

Technology with Many Field Lines

6.1 Computational Tools

A computational technology capable of forecasting SEP events and their impacts is a sophisticated product. It needs to account for many physical aspects of kinetic physics and MHD, while maintaining computational efficiency. Such product can only be a combination of modules/components, where each one is designed to solve it's own set of problems. Ensuring their proper functioning while operating together is a challenging problem in itself. Here, we list available numerical models, that will be included in the final predicting model, and provide their brief description. A major emphasize is made on M-FLAMPA and it's operation, since it is the primary product of the dissertation project.

6.1.1 Space Weather Modeling Framework

The Space Weather Modeling Framework (SWMF) is a high-performance computational tool that was developed to simulate the coupled Sun-Earth system (*Tóth et al.*, 2005a,b, 2007, 2012). One of the main modules within the SWMF is the BATS-R-US MHD code (see below in this Chapter).

The SWMF is a structured collection of software building blocks, such as numerical physical models, coordinated data transfer, data processing tools, etc., designed

to develop Sun-Earth system modeling components in order to couple and assemble them into applications. The framework was designed to have "plug-and-play" capabilities, and presently it links together fifteen inter-operating models of physics domains, ranging from the surface of the Sun to the upper atmosphere of the Earth. Tying these models together gives a self-consistent whole in which each region is described by a world-class model, and those models communicate data with each other. The SWMF has achieved faster than real-time performance on massively parallel computers, similar to facilities available at the CCMC.

The SWMF integrates the BATS-R-US-based AWSoM-R and AWSoM models to simulate the SC and IH as well as the SEP code, all models self-consistently taking into account the Alfvén wave turbulence. M-FLAMPA serves primarily as the interface between the SEP code and SWMF. In this way the self-consistent physics-based model for extreme SEP events will be achieved, with the faster-than-real-time performance and predictive capability.

6.1.2 Block-Adaptive-Tree Solar-Wind Roe-Type Upwind Scheme

The Block-Adaptive-Tree Solar-wind Roe-type Upwind Scheme (BATS-R-US) code solves the equations of extended MHD – a system of equations describing the transport of mass, momentum, energy, and magnetic flux (*Powell et al.*, 1999; *Groth et al.*, 2000). This high-performance code enables Sun-to-Earth CME propagation simulations to be performed in near real-time when run on hundreds of processors on a supercomputer (*Manchester et al.*, 2004a). The implementation of Adaptive Mesh Refined (AMR) in BATS-R-US allows orders of magnitude variation in numerical resolution within the computational domain while keeping the total computational resource requirement at a reasonable level. This is important for a global model of the magnetized solar plasma in which one strives to resolve small structures like shocks, flux ropes, electric current sheets in a 3-D domain, which may extend to hundreds

of $R_\odot$. The use of AMR also enables resolving the fine structure of active regions on the Sun, which spawn CMEs. This is critically necessary for incorporating high-resolution magnetic field observations into a global MHD model. In the context of solar-heliospheric physics, BATS-R-US has been utilized to model the global structure of the solar corona and solar wind (*Roussev et al.*, 2003b; *Cohen et al.*, 2007a; *Cohen et al.*, 2008), the initiation (*Roussev et al.*, 2003b; *Jacobs et al.*, 2009) and propagation of idealized (*Manchester et al.*, 2004b,a) and more realistic (*Roussev et al.*, 2004, 2007; *Lugaz et al.*, 2007b; *Evans et al.*, 2011; *Jin et al.*, 2013) solar eruptions and associated SEP events (*Sokolov et al.*, 2004, 2009).

Two BATS-R-US-based AWSoM models are used to simulate the SC and IH, both self-consistently taking into account Alfvén wave turbulence (see Chapter V). In the SC, the AWSoM-R model is applied above the inner boundary at the heliocentric distance of $R \approx 1.1 - 1.15\ R_\odot$, while below the boundary the model is bridged to the upper chromosphere via threaded field lines (see Chapter V). This way we save computational resources which otherwise would be spent to resolve the detailed structure of the transition region on a highly refined 3-D grid with very short time steps.

6.1.3 Eruptive Event Generator

EEGGL (Eruptive Event Generator using Gibson-Low configuration) is a user-friendly tool developed by *Jin et al.* (2016) and successfully transitioned to the CCMC. It integrates solar images of the eruption into an intuitive visual user interface that allows the user to set the parameters of the GL magnetic configuration to model a magnetically driven CME and its propagation to 1 AU (see Chapter V). EEGGL incorporates magnetograms of the solar magnetic field prior to the eruption, and, if possible, the multi-viewpoint observations of the CME near the Sun. The STEREOCat web-application available at the CCMC, which allows the user to derive both

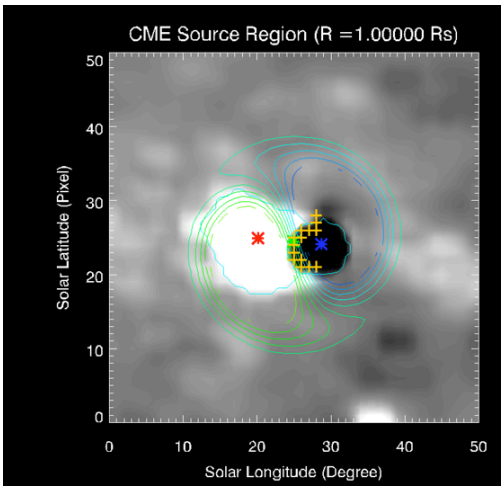

Figure 6.1: The zoomed-in AR as seen in the GONG magnetogram. By clicking on the white (positive) and black (negative) spots, EEGGL calculates the GL configuration parameters. The radial magnetic field levels of the recommended GL configuration is shown with the contour lines. The S-shaped polarity inversion line of the GL configuration, separating the cusped contours, overlaps with that of the AR (yellow crosses).

the CME speed and an approximate source location. With these input parameters the operator chooses the AR from which the CME originates. Using these inputs EEGGL automatically (1) processes the magnetogram; (2) analyzes and calculates the integral parameters of the AR; (3) automatically sets the parameters of the GL magnetic configuration; and finally (4) visualizes the magnetic field of the AR and of the GL configuration to verify that they match (see Fig. 6.1).

The Eruptive Event Generator using the Gibson-Low flux-rope will be used to select an active region on the Sun and insert a flux-rope to simulate a magnetically driven eruption.

6.1.4 Adaptive Mesh Particle Simulator

Dynamics of the energetic particles in the Earth's magnetosphere is inherently of the kinetic nature. The complexity of the magnetic field line topology, together with large gyroradii of the energetic particles compared to the size of the Earth, limits the applicability of the field aligned particle motion approximation. The Monte

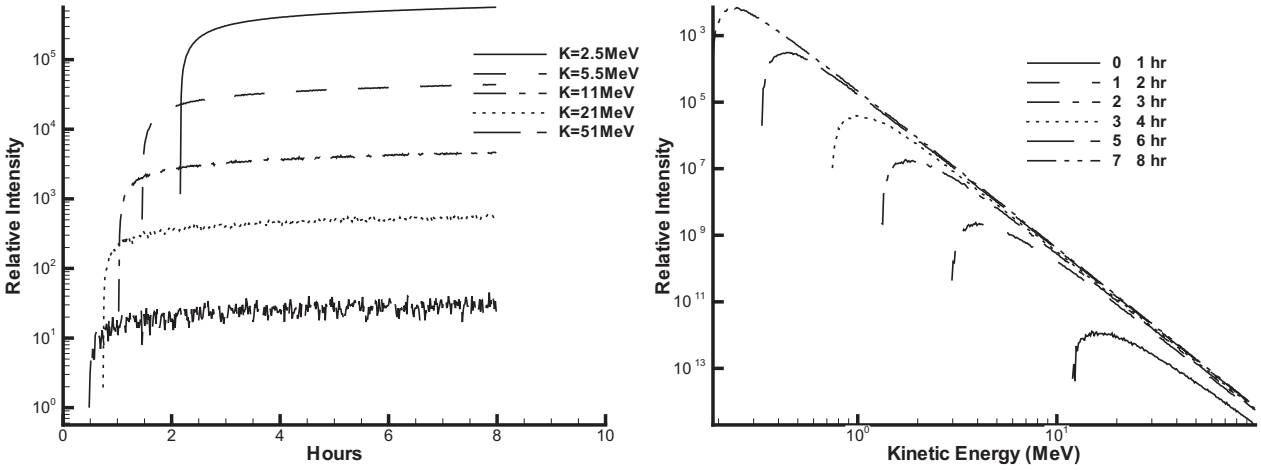

Figure 6.2: *Left:* Computed relative intensity of protons at 1 AU using the Monte-Carlo code. *Right:* Modeled relative spectrum of protons for the same case (see *Tenishev et al.* (2005) for more details).

Carlo approach is the widely used modeling technique for simulating physical systems described by kinetic equations, which is done either by solving a kinetic equation itself, or by modeling of the evolution of a large set of the representative particles affected by the same physical laws and forces as real ones. The primary difference between those approaches is that the first implicitly inherits the same approximations and averaging of the particle microscopic parameters as those integrated into the kinetic equation to be solved. According to the latter, a more realistic particle dynamics may be simulated though some details of this dynamics might be insignificant, and for that matter intentionally neglected when the kinetic equation describing the simulated system was derived, which also can simplify its numerical modeling.

Monte Carlo type models have been be used for studying transport of the energetic particles both inside and outside of the Earth's magnetosphere. Application of a Model Carlo model to simulating transport and acceleration of SEPs is described by *Tenishev et al.* (2005), who have solved Parker equation, Eq. 4.1, assuming that: (1) the magnetic field is described by the Parker's spiral model (*Parker*, 1958), and (2) SEPs are attached to the magnetic field lines. SEPs have been traces outside of the

acceleration region. With these assumptions Eq. 4.1 was reduced to 1-dimensional Boltzmann equation. Scattering of the energetic protons on perturbations of the magnetic field was simulated using standard Monte Carlo approaches, which is illustrated in Fig. 6.2. For charged particles propagating in the solar wind, the collision integral, $(\delta f/\delta t)$, due to scattering from fluctuations of the interplanetary magnetic field can be described in terms of a mean free path, $\lambda_{\parallel}$, that was adopted from *Li et al.* (2003) in the form $\lambda_{\parallel} = \lambda_0 \left(\frac{pc}{1\ \mathrm{GeV}}\right)^{\alpha} \left(\frac{R}{1\ \mathrm{AU}}\right)^{\beta}$, where p is the relativistic momentum of a particle, R is its heliocentric distance, and λ_0 is an empirical parameter. Parameters α and β describe the momentum and the heliocentric dependence of the mean free path λ_0, respectively.

Adaptive Mesh Particle Simulator (AMPS) is a general-purpose Monte Carlo code developed within the frame of the Direct Simulation Monte Carlo method (DSMC) with the original purpose to study planetary and cometary exospheres. Later, AMPS has been generalized to simulate dynamics of the relativistic particles affected by the Lorentz force. AMPS can be used for both (1) modeling of the kinetic equations by advancing a particle location and momentum along characteristics of the simulated kinetic equation, as well as (2) for modeling of the dynamics and evolution of an energetic particle population by tracing the particles affected by the Lorentz force.

One of the most important features of AMPS is employment of the AMR meshes for discretization of the computational domain, which allows it to refine the spatial resolution of the mesh locally where it is needed. That is critically important when the important characteristic scales varies significantly within the simulation domain as it happened when modeling distribution of the energetic particles in a region that includes the entire magnetosphere.

AMPS is a component of the SWMF, and therefore, can be executed coupled with other components of the framework. Coupling with BATS-R-US and M-FLAMPA allows us to complete the suite of the physical model required for forecasting of the

energetic particle distribution within the Earth's magnetosphere starting from the magnetopause and to the LEO altitudes.

6.1.5 Multiple-Field-Line-Advection Model for Particle Acceleration

The geometry of magnetic field lines may become very complex and they can form intricate patterns as they evolve in time. By pushing and twisting field lines, extreme events, such as CMEs and associated interplanetary shocks, can make the field line topology even more complex. This makes forecasting the regions affected by SEP events a challenging problem. To address this challenge one needs to design a computational technique that naturally describes this ever evolving geometry efficiently. The Multiple-Field-Line-Advection Model for Particle Acceleration (M-FLAMPA) code was designed to solve this problem. M-FLAMPA allows us to solve the kinetic equation for SEPs along a multitude of interplanetary magnetic field lines originating from the Sun efficiently, using time-dependent magnetic field and plasma parameters obtained from the MHD simulation. The model is a high-performance extension of the original FLAMPA code *Sokolov et al.* (2004), which simulates SEP distribution along a single field line. M-FLAMPA is a major improvement that takes full advantage of modern supercomputers.

M-FLAMPA solves for a gyrotropic SEP distribution function $f(\mathbf{x}, p, \mu, t)$, where p and μ are the magnitude of the relativistic momentum and cosine of pitch-angle of energetic particles. The code takes advantage of the fact that particles stay on the same magnetic field line and, therefore, the distribution function may be treated as a function of the distance along the filed line, s, rather than a 3-D vector $\mathbf{x}$. Also, coefficients in the governing equations depend only on background plasma parameters and their Lagrangian derivatives (see Chapter IV). This important property reduces the problem of particle acceleration in 3-D magnetic field into a set of independent 1-D problems on continuously evolving Lagrangian grids. Each field line in the model

is treated separately from others resulting in an "embarrassingly parallel" algorithm. We note that the same computational technology is applied to the transport equations for the Alfvén wave amplitudes (*Sokolov et al.*, 2009).

Similar models have been developed previously (see e.g. *Kóta and Jokipii*, 1997; *Kóta et al.*, 2005b,a). The underlying physics of particle acceleration in the low solar corona has been studied with self-consistent particle-in-cell simulation (*Giacalone*, 2005). The larger scale effects have also been investigated. The Energetic Particle Radiation Environment Module (EPREM) was designed to account for SEP propagation and acceleration in rapidly changing magnetic fields (*Schwadron et al.*, 2010). EPREM also uses Lagrangian grids to represent evolving magnetic field lines. The original model assumed a Parker spiral configuration. Later the solution of a realistic MHD model was used as a background plasma state by *Kozarev et al.* (2013); *Schwadron et al.* (2014, 2015). The primary focus of the effort was physics of acceleration mechanisms and effects of particle acceleration fairly close to the Sun (up to 8 solar radii).

M-FLAMPA stands out compared to these efforts as the first numerical model aimed at actually forecasting SEP events. It treats the background plasma state as a time series of Lagrangian grids, which significantly simplifies the computations. In addition, M-FLAMPA is a part of a larger integrated system, and it is directly coupled with AWSoM via the SWMF. This integration allows the user to run both codes simultaneously, thus saving time, memory and even computational power. No intermediate steps, such as saving MHD into output files by one model and subsequently re-reading them by another, are required. This opens a possibility to study SEP events at distances comparable with 1 AU. The model is able to predict SEP fluxes and spectra that may be potentially produced by CMEs should they occur at a currently existing active region on the solar surface. This technology can provide advanced warning needed to mitigate potentially hazardous impacts of SEP events.

M-FLAMPA is augmented with a new interpolation algorithm that was designed to provide smooth and continuous field lines on very complex AMR grids used in realistic MHD simulations of extreme solar events (*Borovikov et al.*, 2015, see Appendix A). The primary advantage of the algorithm is the elimination of spurious distortions near grid resolution interfaces that produce shock-like effects on the particle population traveling along a field line. These distortions may have complex geometries and are otherwise unavoidable. The new algorithm solves this problem entirely.

M-FLAMPA was designed to operate as part of a larger framework. An advanced coupling algorithm ensures efficient communication with multiple MHD models such as AWSoM and AWSoM-R. This technique seamlessly connects field lines between the computational domains of different components of SWMF, e.g. one simulating the solar corona and one simulating the inner heliosphere. Ultimately, this technique results in smooth field lines without spurious distortions. Again, it is important to emphasize that the coupling algorithm does not hinder the performance of either code, BATS-R-US and M-FLAMPA.

These underlying algorithmic innovations ensure that M-FLAMPA can combine the accuracy of realistic MHD simulations with high computational efficiency. Thus, the new technology is well suited for space weather applications such as modeling and predicting SEP impacts during extreme solar events.

The integrated model traces magnetic field lines from the MHD models to connect an object of interest (Earth, spacecraft) with the Sun or, alternatively, find the area that is covered by field lines originating from a given area of the solar surface,such as an active region. As described above, each field line is represented by a Lagrangian grid that advects with the background plasma in a time dependent manner. The relevant data at the location of the grid points is transferred to M-FLAMPA, which in turn calculates the evolution of the energetic particle population by solving the

governing kinetic equations.

6.2 Field Line Tracing

Since the concept of field lines is the backbone of the method, the tracing of field lines must be treated with great care and attention. Tracing the field line is essentially a numerical integration of the equation

$$\frac{d\mathbf{R}}{ds} = \mathbf{b}(\mathbf{R}) \tag{6.1}$$

A common and reliable approach is using the second order explicit Runge-Kutta method:

$$\begin{aligned} \mathbf{R}^{n+\frac{1}{2}} &= \mathbf{R}^n + \frac{1}{2}\Delta s\, \mathbf{b}\left(\mathbf{R}^n\right) \\ \mathbf{R}^{n+1} &= \mathbf{R}^n + \Delta s\, \mathbf{b}\left(\mathbf{R}^{n+\frac{1}{2}}\right) \end{aligned} \tag{6.2}$$

However, it must be noted that accelerating particles are extremely sensitive to discontinuities in the background parameters. Sudden changes in geometry, in particular, in direction of lines may result in perceived discontinuities. Continuous second order interpolation (Appendix A) solves the problem of smooth tracing of lines across resolution changes in the grid. However, it doesn't guarantee that the line being traced from the solar surface would extend to 1 AU or any given significant large heliocentric distance. The line may turn back and close onto the solar surface.

This presents yet another challenge for the overall method. For example, should an AR be located close to the current sheet, many of the lines may close. In this case, a large portion of computational effort would be spent on the processing of these lines, while providing no real output for the purposes of the research.

Several solutions are suggested. First, the simplest approach is to stop tracing of

field lines once they start turning back to the Sun. The signal to do so in the change of the sign of b_R. This event is likely occurs, when the line crosses the Current Sheet. The solar wind subsequently pushes the fluid elements along the line away from the Sun. Eventually the line would reach 1 AU.

Another approach is to correct the direction of lines to prevent them from closing. To do so one may try to divert the line away the surface b_R=0 The correction to line's direction to be introduced may be determined based on, for example, the gradient of b_R. In particular, to correct the line, the direction $\mathbf{b}$ is substituted as

$$\mathbf{b}^{n+\frac{1}{2}} \Rightarrow \mathbf{b}^{n+\frac{1}{2}} + \min\left(\frac{1}{2}\Delta s, \frac{\boldsymbol{\gamma}\cdot\boldsymbol{b}^{n+\frac{1}{2}}}{\boldsymbol{\gamma}\cdot\boldsymbol{\gamma}}\right)\boldsymbol{\gamma}$$

$$\boldsymbol{\gamma} = \begin{cases} \frac{\nabla b_R}{b_R}(1-2|b_r|) & \text{if } |b_R| < 0.5 \\ 0 & \text{if } |b_R| > 0.5 \end{cases} \tag{6.3}$$

This diverts the line away from the surface b_R=0, the effect is stronger the closer the line approaches this surface. Unlike the previous method, this causes the traced lines to temporarily decouple from the actual field line. Eventually, however, thus traced line will reach the appropriate state as in the previous method due to solar wind pulling the line away from the Sun.

This method, however, has limited efficiency. The main assumption is that the corrected line would, in extreme case, travel parallel to b_R=0 until it reaches a field line that is directed away from it. This is valid if normal vector of b_R=0 has anti-parallel component to $\mathbf{b}$. In the opposite case, the corrected line moves closer to the surface with each step.

Corrections may be introduced in a different fashion. For example, one may derive

from Eq. 6.1:

$$\begin{aligned} \frac{d^2\mathbf{R}}{ds^2} &= \frac{d\mathbf{R}}{ds} \times \left[\frac{d\mathbf{b}}{ds} \times \frac{d\mathbf{R}}{ds} \right] \\ \left. \frac{d\mathbf{R}}{ds} \right|_{s=s_0} &= \mathbf{b}(s_0) \end{aligned} \tag{6.4}$$

System Eq. 6.4 is equivalent to Eq. 6.1. The integration of Eq. 6.4 is based on a well-known within the computational plasma physics community Boris scheme (*Boris*, 1970) and goes as follows

$$\begin{aligned} \boldsymbol{\Omega}^{n-\frac{1}{2}} &= \frac{\mathbf{b}^n - \mathbf{b}^{n-\frac{1}{2}}}{\Delta s/2} \times \left(\frac{d\mathbf{R}}{ds} \right)^{n-\frac{1}{2}} \\ \left(\frac{d\mathbf{R}}{ds} \right)^{n} &= \left(\frac{d\mathbf{R}}{ds} \right)^{n-\frac{1}{2}} + \frac{\Delta s}{2} \left(\frac{d\mathbf{R}}{ds} \right)^{n-\frac{1}{2}} \times \boldsymbol{\Omega}^{n-\frac{1}{2}} \\ \mathbf{R}^{n+\frac{1}{2}} &= \mathbf{R}^{n-\frac{1}{2}} + \left(\frac{d\mathbf{R}}{ds} \right)^{n} \frac{\Delta s}{2} \\ \boldsymbol{\Omega}^{n} &= \frac{\mathbf{b}\left(\mathbf{R}^{n+\frac{1}{2}}\right) - \mathbf{b}\left(\mathbf{R}^{n-\frac{1}{2}}\right)}{\Delta s} \times \left(\frac{d\mathbf{R}}{ds} \right)^{n} \\ \left(\frac{d\mathbf{R}}{ds} \right)' &= \left(\frac{d\mathbf{R}}{ds} \right)^{n-\frac{1}{2}} + \frac{\Delta s}{2} \left(\frac{d\mathbf{R}}{ds} \right)^{n-\frac{1}{2}} \times \boldsymbol{\Omega}^{n} \\ \left(\frac{d\mathbf{R}}{ds} \right)^{n+\frac{1}{2}} &= \left(\frac{d\mathbf{R}}{ds} \right)^{n-\frac{1}{2}} + \Delta s \frac{\left(\frac{d\mathbf{R}}{ds}\right)' \times \boldsymbol{\Omega}^{n}}{1 + \frac{\Delta s^2}{4} \Omega^{n\,2}} \\ \mathbf{R}^{n+1} &= \mathbf{R}^{n} + \Delta s \left(\frac{d\mathbf{R}}{ds} \right)^{n+\frac{1}{2}} \end{aligned} \tag{6.5}$$

Additionally, the step size Δs is reduced, if after the iteration the sign of b_R changes.

The main advantage of this integration scheme is the smoother correction to the line's direction. The correction vector, $\boldsymbol{\gamma}$, is instead added to $d\mathbf{b}/ds$. It is computed similarly, but one also needs to account for the "memory" of this scheme: direction at each step depends on the direction at previous step. For this reason, once the line has moved far enough from b_R=0, it needs to be forced to turn back to the direction

of the field. Thus, the correction is chosen to be

$$\begin{aligned} \frac{d\mathbf{b}}{ds} &\Rightarrow \frac{d\mathbf{b}}{ds} + \boldsymbol{\gamma} \\ \boldsymbol{\gamma} &= \begin{cases} \frac{\nabla b_R}{b_R}(1 - 2|b_R|), & \text{if } |b_R| < 0.5 \\ \frac{1}{\lambda}\mathbf{b}, & \text{if } |b_R| > 0.5 \end{cases} \end{aligned} \tag{6.6}$$

where λ is a parameter that defines the curvature radius of the line as it turns back to the field's direction. The choice of λ=$10\Delta s$ proved to be reasonable.

6.3 Storage

A new distributed data structure has been developed to efficiently store extracted field lines within BATS-R-US. Since each line is represented with a set of fluid elements, its size isn't known in advance. Therefore, the storage needs to accommodate some unknown number of particles with unknown distribution over computational processors, which may change significantly over the times of simulation. The implemented storage is organized as an unstructured collection of objects, each holding parameters such as coordinates, identification of field line and index along the line. Evolution of field lines in time is simulated via advection of these objects with the local plasma bulk velocity. Values of plasma parameters are obtained via interpolation (Appendix A) on the AMR grid of BATS-R-US. Distribution of fluid elements over processors is also defined according the interpolation algorithm.

6.4 Preliminary Results

The current operational version of the predictive technology consists of: (1) numerical MHD model of SC (covering the region from 1.15 $R_\odot$ to 21 $R_\odot$) - BATS-R-US; (2) numerical MHD model of IH (covering the region from 21 $R_\odot$ to 1 AU) - BATS-R-US; and (3) numerical kinetic model of SEP transport along individual magnetic field

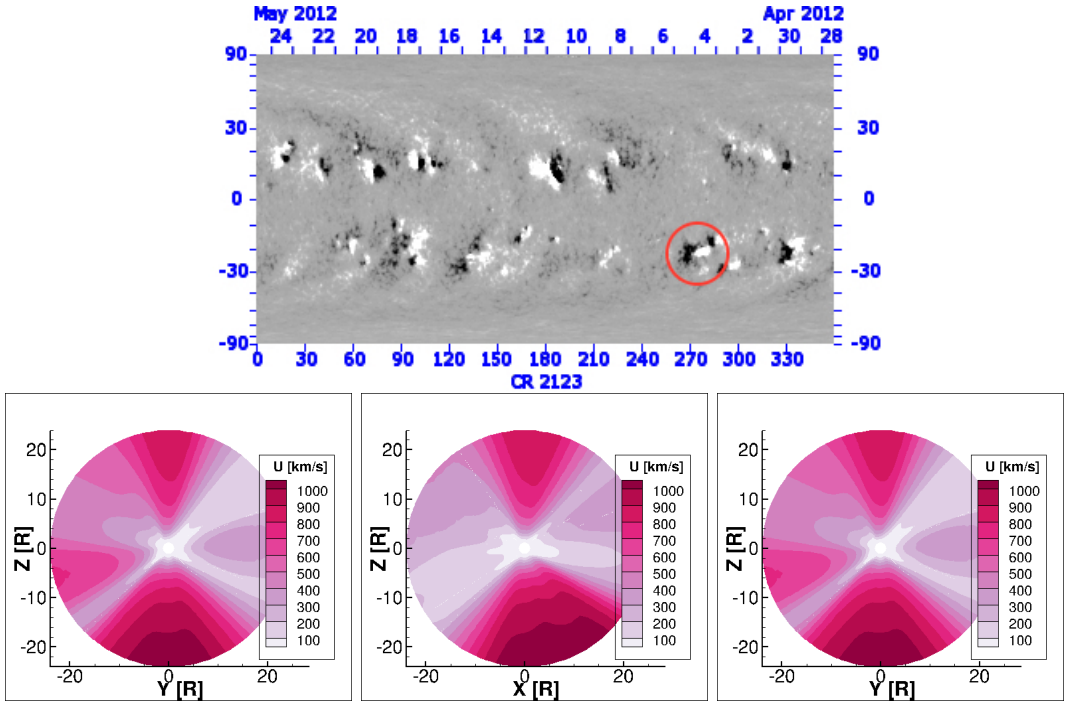

Figure 6.3: **Top**: GONG synoptic map for Carrington rotation 2123. The color is the strength of the observed magnetic field with its polarity being positive for light gray and white areas and negative for dark gray and black areas. The red circle marks the chosen AR. The extracted field lines originate above this AR. **Bottom**: the simulated state of SC corresponding to this synoptic map. Color shows the magnitude of the plasma bulk velocity.

lines - M-FLAMPA.

As discussed before, the communication between the constituting components is a crucial aspect of the overall model. The data is exchanged according to the following pattern: (1) MHD data is passed from the SC model to the IH model, where it serves as a boundary condition; (2) the field lines, the geometry and the background conditions, are extracted and imported from the data simulated by the SC and IH models to the particle model.

Here, we demonstrate an example of the technology's application to realistic steady conditions. The simulation is split into two stages. The goal of the first stage is to obtain the steady state of SC and IH, SEP population isn't simulated. After this stage is completed, the field lines are extracted from the simulated background

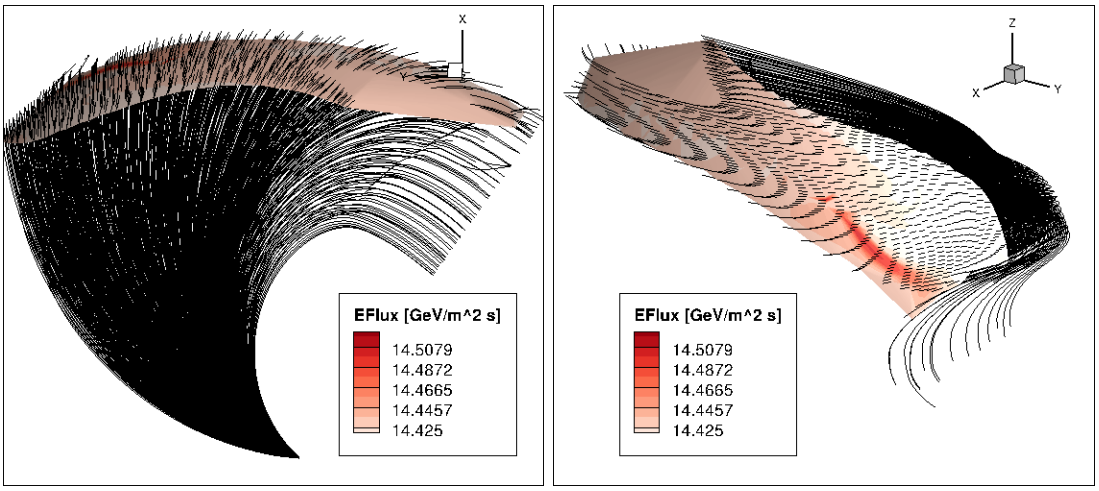

Figure 6.4: The extracted field lines and their mapping onto 1 AU sphere. The conditions are steady, the shape of the field lines is similar, at least qualitatively to the classic Parker's spiral. Triangulation on footprints of field lines on the 1 AU sphere allows interpolating the simulated data to obtain, for example, the energy flux carried by SEPs at 1 AU (shown in color). The mapped region has an irregular shape, which is expected due to non-trivial geometry of field lines.

and then imported into M-FLAMPA.

To provide a realistic representation of the background, we have used the Global Oscillation Network Group (GONG) synoptic map for Carrington Rotation 2123 (see Fig. 6.3) as a boundary condition for the solar corona model. The MHD simulation results are also shown in Fig. 6.3.

At the beginning of the second stage, an AR on the synoptic map has been chosen (see Fig. 6.3) and a rectangular angular grid has been imposed over this region. The field lines have been traced from this grid both towards and away from the Sun. The extracted field lines as well as the region on 1 AU sphere that they map are shown in Fig. 6.4.

The simulation proceeded as follows. All the numerical models simulated a time dependent evolution of the system. The advection of the extracted field lines was simulated by both MHD models, which also regularly provided an updated information on the location of the field lines as well as the state of the background to the

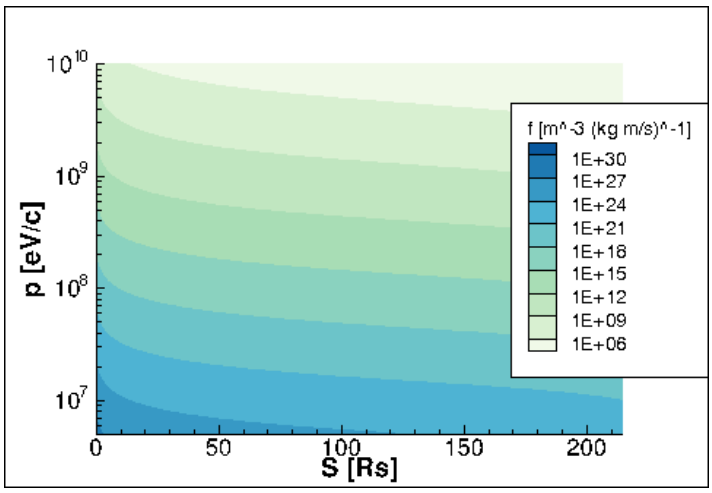

Figure 6.5: Simulated distribution of SEP along an individual field line. S is the distance along the field line and is measured in solar radii. Since the background conditions are steady, no enhancements of high energy part of the distribution are observed.

particle model. The latter, in its turn, used these data to simulate the transport of the SEP population along the field lines. We have injected the particle population with the following energy distribution at origins of field lines on solar surface (cf. *Sokolov et al.*, 2004)

$$f\left(p_{\text{inj}}\right) = \frac{C_{\text{inj}}}{4\pi(q-3)} \frac{N_p}{\left(2m_pT_p\right)^{3/2}} \left(\frac{\sqrt{2m_pT_p}}{p_{\text{inj}}}\right)^q \tag{6.7}$$

where N_p and T_p are the background plasma density and temperature, q is the spectral index, and C_{inj} is the injection efficiency, which determines the absolute value of SEP flux. Example of the simulated particle distribution along an individual field line is shown in Fig 6.5.

The main goal of this simulation was to demonstrate the operation of the prototype of the forecasting model. The simulation was performed for steady conditions without extreme events such as solar flares or CMEs, no enhancements of the high energy particle flux have been observed. Although the technology's ability to simulated extreme solar events hasn't been tested, the initial results for steady conditions serve

as a proof of the feasibility of the technology.

Results have been obtained using the computational resources of the NASA Pleiades super-computer. The number of computational cores used is 300, the in-simulation time was about 1.5 faster than the real time.

CHAPTER VII

Simulation of Electron Acceleration During Solar Flares

7.1 Introduction

Here we present the results of simulation of electron acceleration in contracting plasmoids during solar flares. This work is a continuation of the work of *Guidoni et al.* (2016) and is a collaborative effort between University of Michigan and NASA Goddard Space Flight Center.

The main goal is to explore the acceleration mechanism suggested by *Drake et al.* (2006a). As discussed in Chapter II, solar flares are accompanied by a formation of plasmoids in the reconnection current sheet. As plasmoids contract, the particles being trapped inside them gain energy. The primary particle species affected by this mechanism is the electron species, which are in focus of this study. The effect of the acceleration per individual electron within a single contracting plasmoid is expected to be modest (*Drake et al.*, 2006a). For example, *Guidoni et al.* (2016) found an increase in energy below a factor of 5. This result is extended, and generally confirmed, by the analysis presented in the present work.

7.2 MHD Simulation

The background plasma conditions have been simulated with the Adaptively Refined MHD Solver (ARMS) code (*DeVore*, 1991). A detailed description of this simulation can be found in *Guidoni et al.* (2016). For the sake of simplicity, a 2.5D setting is adopted, i.e. the system is assumed to have axial symmetry. Ideal MHD is assumed. The flare is triggered according to the principles discussed in *Karpen et al.* (2012) and earlier papers on the breakout mechanism for solar eruptions (e.g. *Antiochos et al.*, 1999). The modeled current sheet, as expected, is populated by several X-points separated by plasmoids, which are usually referred to as magnetic islands under 2.5D conditions. Because the current sheet forms in the initially low-lying, sheared magnetic field that powers the eruptive flare, the magnetic field in the sheet has a strong component in the translationally invariant direction (out of the plane in Figure 7.1).

A number of islands were well resolved on the adaptive mesh. Their shape, evolution and life cycle were carefully tracked. The simulation revealed the presence of one persistent X-point with smaller ones generated near it, some moving sunward until reaching and merging with the flare arcade, others moving outward and merging with the erupting coronal mass ejection.

Those islands that were present in the system for significantly long time and had clear features were chosen for investigation to test the acceleration mechanism of *Drake et al.* (2006a). Since ARMS doesn't include a particle tracking capability, only theoretical estimates could be made. We found that individual electrons should gain up to a factor of 5 in energy (*Guidoni et al.*, 2016). The simulated MHD data for Island 2 of *Guidoni et al.* (2016) was exported and used as input for the particle simulation described below.

7.3 Particle Simulation

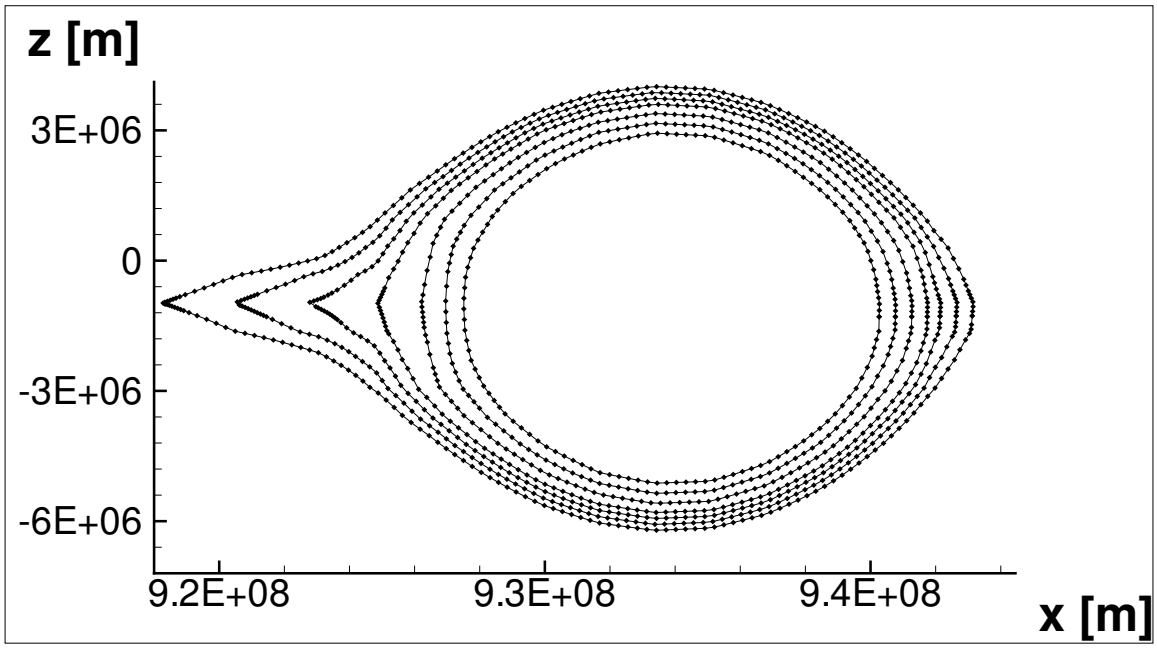

Figure 7.1: Extracted field line projections. Diamond shapes are the fluid elements obtained via the extraction procedure described in Chapter VII. The effectiveness and accuracy of the procedure are demonstrated with well-resolved features of the field lines at the parts stretched toward the X-point (toward the left axis).

The electron population's evolution has been simulated with the AMPS code developed at the University of Michigan and successfully used by *Tenishev et al.* (2008, 2010, 2013).

The injected electrons were randomly sampled from the tail of the Maxwellian distribution in the range between $v_{min}^{inj} = 5 \times 10^6$m/s and $v_{max}^{inj} = 1.2 \times 10^7$m/s:

$$f(\mathbf{v}) \propto \exp\left\{-\frac{m(\mathbf{v}-\mathbf{U})^2}{2k_B T}\right\}, \tag{7.1}$$

where k_B is the Boltzmann constant, T and $\mathbf{U}$ are local plasma temperature and bulk velocity. The energy range was chosen to ensure that the two adiabatic invariants discussed in Chapter III are conserved. To satisfy this condition, particles need to

move faster than the the island contracts. Due to outflows from the X-points, the characteristic speed of contraction is the Alfvén speed, $V_A \sim 10^5$m/s.

With this setup, rather than directly integrating Newton's equations of motions for the electrons in the electromagnetic field, **E** and **B**, which would be prohibitively expensive, we are enabled to integrate the equations for guiding-center motion (see Chapter III). The full 3-D simulation of individual particles must resolve each gyration of a particle about the magnetic field. This puts an enormous restriction on the time step. The scale of this restriction is demonstrated by the following estimation. The value of the magnetic field in the region of interest is $\sim 10^{-5}$T, which results in a gyration period of $m/(eB) \sim 10^{-6}$s, where e is the electron's charge. In order to simulate a process that lasts 10 minutes, one would need to perform at least half a trillion time steps per electron. Since the number of test electrons per field line needed to produce reliable statistics is of order of a million, the problem would be virtually impossible to simulate on modern hardware. Thus the adoption of guiding center motion equations greatly facilitates simulation of the problem.

7.4 Data Structure

It is also worth noting that the guiding center approximation is naturally tied to the notion of the magnetic field lines. Thus, the underlying physics of the process motivates improvements in the numerical approach. Since the motion of high energy electrons is essentially one-dimensional, as viewed on a larger scale, and follows the magnetic field lines, it is most practical to adopt a data structure that takes advantage of it.

Rather than utilizing a Cartesian grid, a linear structure that follows a magnetic field line has been developed. Under the assumption of axial symmetry used to simulate the background field and plasma, which reduces the dimensionality of the problem, we introduce a scalar potential for poloidal (out of the plane of Figure 7.2)

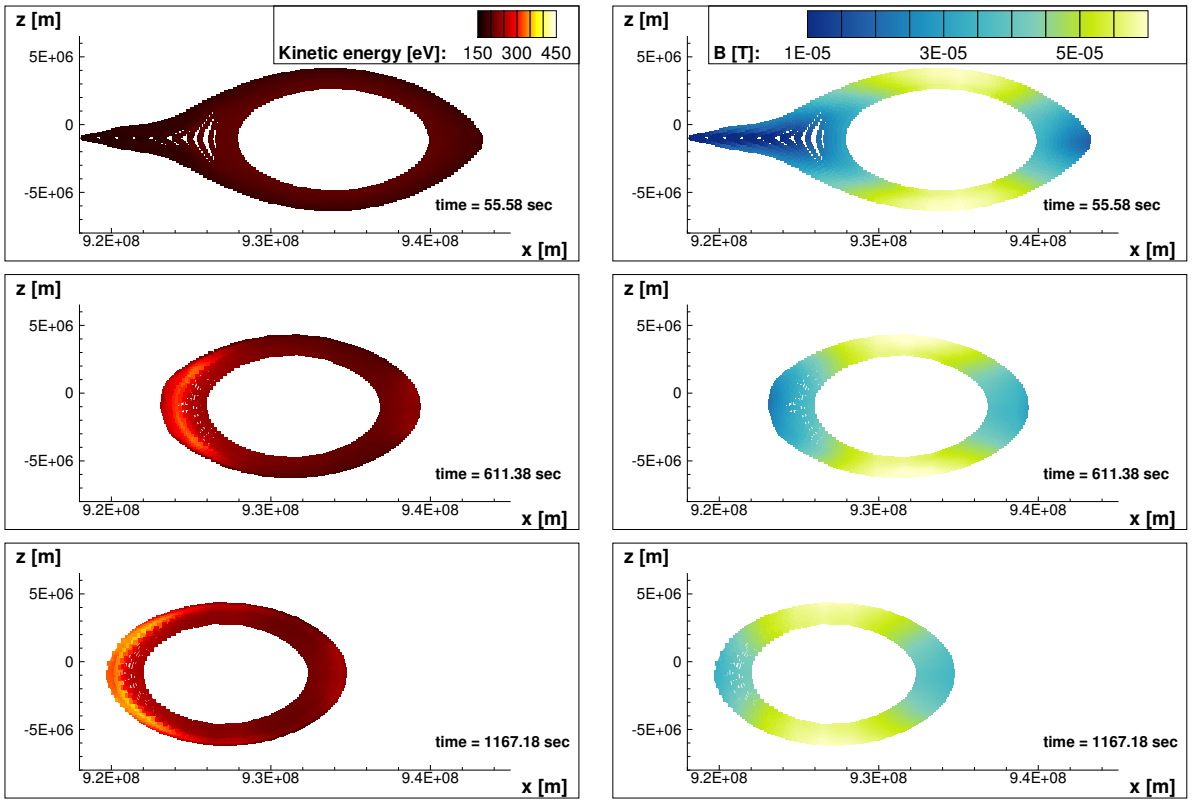

Figure 7.2: Evolution of a magnetic island over time. Left column: colors indicate average kinetic energy of electrons; right column: colors indicate magnitude of background magnetic field. Electrons gain most energy when magnetic field changes most rapidly, as seen in the stretched sections of field lines.

components of the magnetic field as well as the magnetic flux function, Ψ. The latter quantity greatly simplifies the problem of field line extraction while keeping high accuracy. The procedure is as follows.

The poloidal projection of a magnetic field line is defined as a line of constant value of Ψ. If one chooses a starting point for a magnetic loop, it is possible to extract the whole loop point-by-point.

The initial point, X_0, is taken at an arbitrary location within the magnetic island. The value of the magnetic flux function, Ψ_0, must be the same for all points associated with this magnetic loop. The candidate point is taken in the direction of the magnetic field, then it is corrected via gradient descent iterations until value of the magnetic

flux function is sufficiently close to Ψ_0.

$$\begin{aligned}
\tilde{\mathbf{X}}_0 &= \mathbf{X}_{n-1} + \mathbf{B} * \delta \\
\tilde{\mathbf{X}}_k &= \tilde{\mathbf{X}}_{k-1} + \alpha \frac{(\tilde{\Psi}_k - \Psi_0)}{B^2} \nabla \tilde{\Psi}_k, \quad k \geq 1 \\
\mathbf{X}_n &= \tilde{\mathbf{X}}_\infty,
\end{aligned} \tag{7.2}$$

where $\mathbf{X}_{n-1}$ is the last extracted point on the field line, $\mathbf{B}$ is the magnetic field at this location, $\mathbf{X}_n$ is the point being extracted, k enumerates iterations, $\tilde{\mathbf{X}}_k$ and $\tilde{\Psi}_k$ are values at iteration k, $\tilde{\mathbf{X}}_\infty$ is the limit of iterations, δ controls distance between consecutive extracted points, and α controls stability of gradient descent.

The effectiveness and accuracy of this procedure are demonstrated in Figure 7.1. As one can see, even complex features such as the stretched parts of field lines near an X-point additionally complicated with low values of the magnetic field are carefully resolved.

Each point thus extracted moves with the local plasma velocity. Under ideal MHD, frozen-in conditions apply, hence allowing us to trace the evolution of an individual field line via following motion of fluid elements extracted along it.

Although only the poloidal projections of field lines were extracted, the full 3D plasma velocity is used to update their state. The new locations of thus-obtained fluid elements are then projected to the original poloidal plane. The same procedure was applied to the electron motion.

The background plasma data from our ARMS simulation are imported into AMPS, with a data file cadence of 1 second. To maintain higher accuracy, linear time interpolation between files is used. Extracted field lines are regularly updated with each plasma fluid element being moved with the velocity of the background plasma and corrected via gradient descent to match the original value of Ψm which should be preserved under ideal MHD.

Another reason why our approach is better suited for particle tracking in the current case is the issue with electrons staying within the island. While the physical reason for electrons to escape the island is the cross field drift, artificial electron leakage from the island is observed when a full 3D simulation on a regular grid is performed. Since the field evolves rapidly, an electron on the edge of the island commonly finds itself outside the island when the plasma state is updated. Such electrons escape the domain and information is lost. Our solution is to correct the position of a electron in order to put it back into the island (Eq. 7.2). With the adopted field-aligned data structure this problem was effectively non-existent. Since all electrons are essentially attached to field lines, they cannot escape the island due to non-physical reasons.

7.5 Results

The particle-tracking simulation started after an island was fully formed. Evolution of the electron population was prominent throughout all contraction process. Results are presented in this section.

First, a significant change in energy is observed. The evolution of the average electron kinetic energy, together with magnitude of the background magnetic field, is shown in Figure 7.2. It is clearly seen that the most rapid change in energy occurs near the stretched parts of field lines. These are the locations where electrons experience betatron and Fermi acceleration, as the newly reconnected magnetic field retracts and thus carries electrons away from the reconnection regions. The energy increase is much higher on the left (Sunward) side of the island than on the right, because the initial shape of the outward side is smoother and, therefore, undergoes less intense change in the background field. Also, the magnetic field increases more in magnitude on the sunward side as seen in Figure 7.2. The initial field strength is lower there, as it is closer to the corresponding X-point. As described in Chapter III, an increase

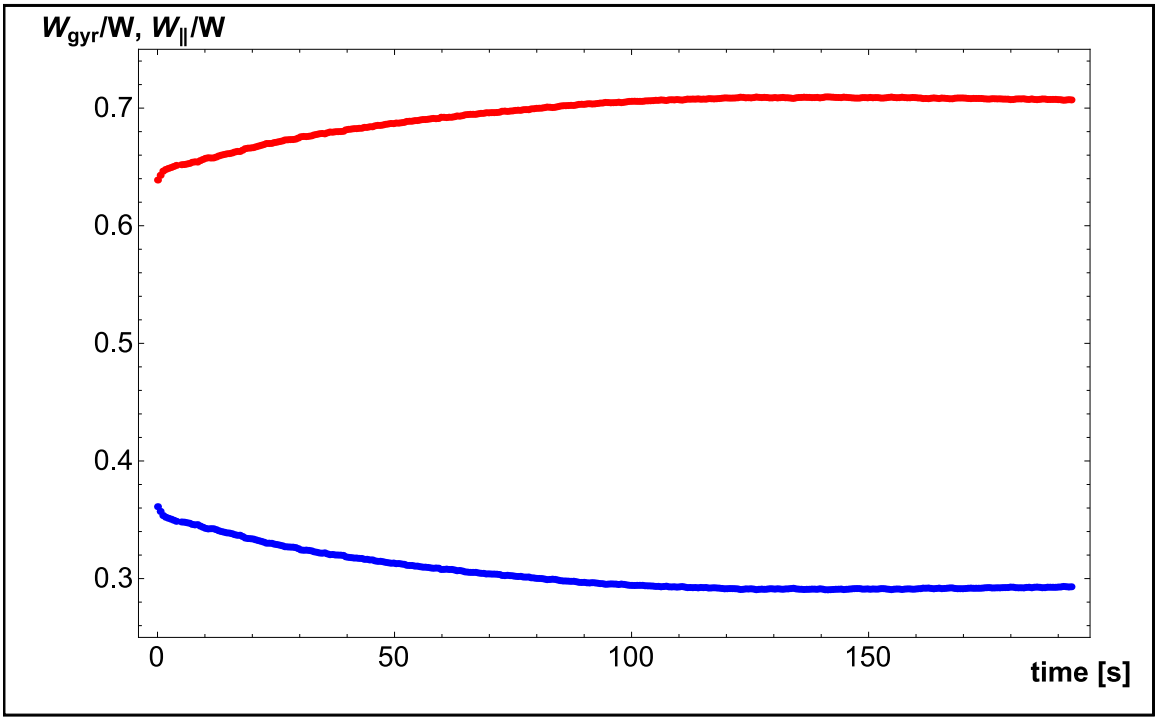

Figure 7.3: Evolution of partition of particle energy between 0 and 200 seconds from the start of the simulation: red curve is the fraction of gyration energy W_{gyr}/W, blue curve is the fraction of energy of parallel motion $W_{\|}/W$.

in magnetic field strength leads to an increase in the gyration energy of electrons due to the betatron effect. In addition, the island contracts overall and the electrons experience slow but steady energy gain throughout the whole island, producing an increase in the parallel energy due to Fermi acceleration.

In order to determine the relative importance of betatron and Fermi acceleration in our analysis, we tracked the population's energy partition as shown in Figure 7.3. The fractions of gyration and parallel energy, W_{gyr}/W and $W_{\|}/W$, respectively, are displayed as red and blue curves. Both W_{gyr} and $W_{\|}$ increase with time, so both acceleration mechanisms are active, but W_{gyr} clearly increases faster than $W_{\|}$. Thus, the betatron mechanism dominates the acceleration of particles in our simulation. This result differs from that reported by *Drake et al.* (2006a), who found only a small contribution by the betatron effect in the nearly incompressible evolution of their

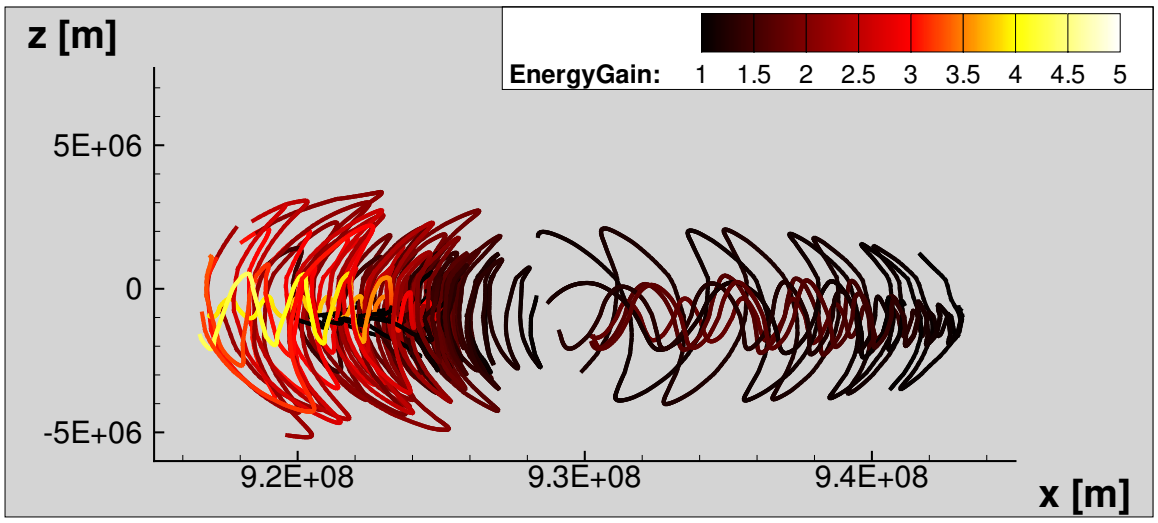

Figure 7.4: Trajectories of selected individual particles. Energy gain is the highest for particles that bounce between mirror points close to the reconnection region and are subject to betatron and Fermi acceleration continuously throughout the process.

kinetic simulation. Indeed, a more recent and comprehensive analysis of acceleration mechanisms in kinetic reconnection by *Dahlin et al.* (2014) shows that the betatron effect actually slightly cools (decelerates) electrons in their system, due to a field-strength reduction in the islands after they form. In contrast, our flare simulation (*Guidoni et al.*, 2016) is highly compressible. The strong compression of the island leads to a substantial, indeed dominant, contribution of betatron acceleration to the total energy gain of the electrons.

While the average energy increase is ~ 2, some electrons experience an energy gain of up to 5 as shown in Figure 7.4: the electrons that bounce between mirror points close to the reconnection region. These electrons reside in the acceleration region throughout the lifetime of the trapping island, as is reflected in the higher average energy gain in this region in Figure 7.2. This is consistent with analysis in *Guidoni et al.* (2016): the energy gain depends on the initial pitch angle of the electrons. In kinetic simulations by *Oka et al.* (2010), the simulated electrons experienced an energy gain ~ 1.25 after being trapped in a magnetic island. However, that study

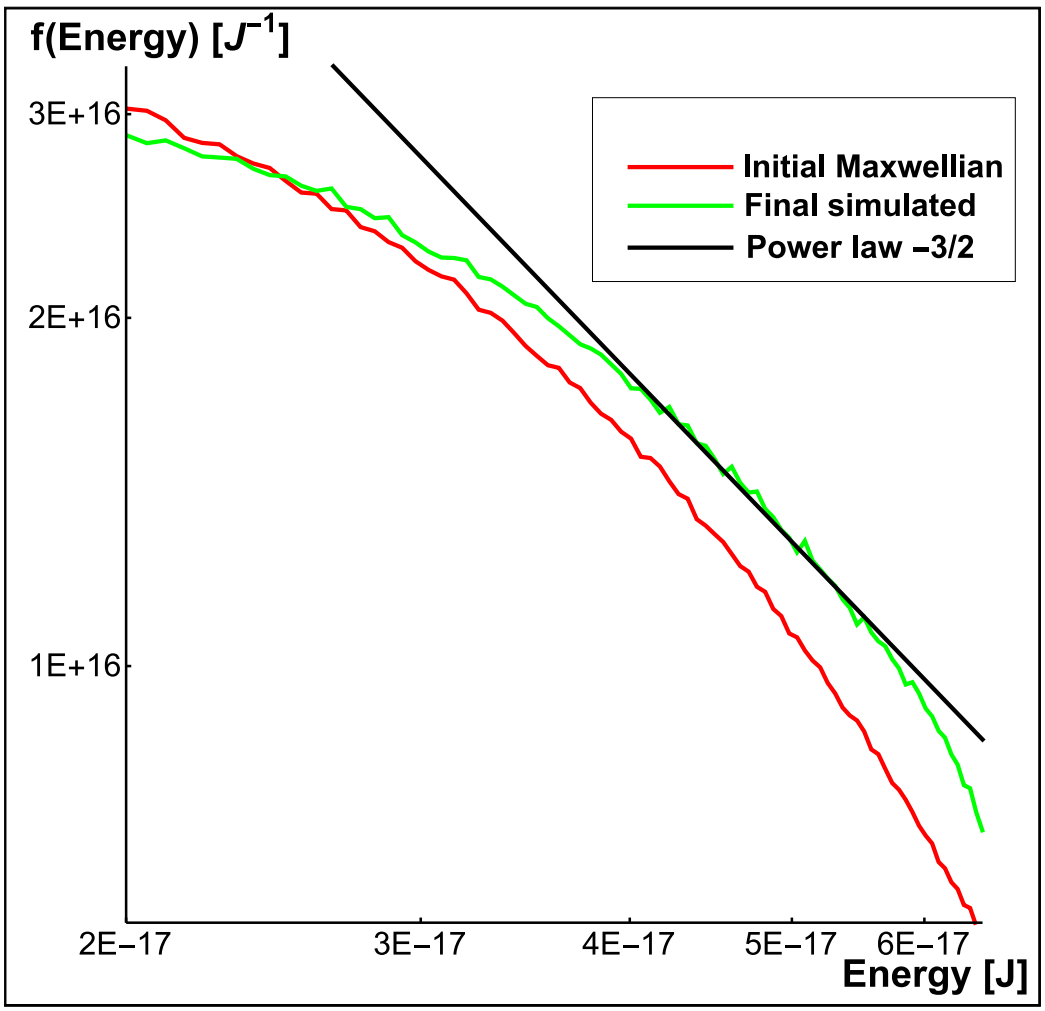

Figure 7.5: The initial and final electron energy distribution. Curves are shown on a log-log scale. The low energy part of the final distribution (green solid) drops due to lack of particles below the cutoff energy and bears no physical significance. At the end of the simulation the high energy tail of the distribution moved slightly closer to a power law with index -1.5.

considered relativistic electrons, while in the present work the classical approximation is still valid.

Finally, the change in the overall energy distribution, sampled over all electrons injected into the island (2×10^6), is demonstrated in Figure 7.5. The initial energy distribution is Maxwellian. In response to island contraction, its high energy tail moved closer to the ubiquitous $\propto E^{-3/2}$ power law that is commonly found in the distribution of suprathermal electrons (*Drake et al.*, 2006b). Moreover, the basic

assumption of *Drake et al.* (2006a) is that electrons experience acceleration multiple times in several magnetic islands. Therefore, when electrons visit many islands, we expect that the final distribution may approach a power law with a spectral index even closer to that observed. Such multiple visits to successive islands also seem necessary to obtain the energy amplifications required to understand hard X-ray emissions in flares. Whether the dominant mechanism is betatron or Fermi acceleration, or both are comparably important, the amplification by passage through a single island seems to be limited to a factor of 5 or less. Thus, as concluded by both *Drake et al.* (2006a) and *Guidoni et al.* (2016), accelerated electrons would have to visit several islands in order to attain the high energies observed.

Our particle-tracking simulation shows a clear average energy gain on the order of 2 for electrons trapped in a single magnetic island, with some electrons reaching a gain of $\sim$5. This is consistent with the results of *Guidoni et al.* (2016). We also found that, although the final electron energy distribution didn't reach a power law after contraction of one magnetic island, it is significantly different from the initial Maxwellian. Our study also revealed that betatron acceleration, rather than Fermi acceleration, is responsible for most of the energy gain.

In a more realistic scenario, i.e. for a flare occurring at active-region scales rather than the global scale of the *Guidoni et al.* (2016) MHD simulation, the plasmoids occupy a smaller volume. Because the drift velocity scales inversely with island size, electrons would escape more easily and reach other acceleration regions, thus undergoing additional acceleration. We expect the resulting electron distribution to more closely resemble a power law when the whole process is repeated many times via electrons traveling in multiple contracting islands. Islands merging as studied in *Drake et al.* (2013) is yet another opportunity to boost the acceleration process. However, *Guidoni et al.* (2016) found that very few islands merged in the model flare current sheet.

The approach utilized in this work assumes that the energetic electron population doesn't significantly affect the magnetic-field evolution, and the MHD and particle simulations were performed independently. On the other hand, self-consistent plasma simulations have shown that about half of the magnetic energy of a magnetic island is transferred to the energetic electrons (*Drake et al.*, 2006a).

The final conclusion of this study is that the island-contraction acceleration mechanism of *Drake et al.* (2006a) is a promising candidate to explain the energetic electron population observed in solar flares. The present study also finds that, when compressibility is included, the dominant source of electron acceleration in contracting islands is the betatron mechanism, rather than the Fermi process.

APPENDICES

APPENDIX A

Second-Order Accurate Continuous Interpolation on Block Adaptive Grids

A.1 Intro

The AMR grids (*Berger and Colella*, 1989) have become an essential part of many applications in computational physics. The AMR is an effective technique which allows us to adapt grid to particular features being simulated. For example, adaptive spatial discretization is employed by the BATS-R-US code for solving MHD equations (*Powell et al.*, 1999, 2003; *Gombosi et al.*, 2004; *Powell et al.*, 2005).

Often the physical quantities to be calculated are known at cell centers. To obtain data at arbitrary locations one needs an interpolation algorithm. A high variety of approaches allows us to achieve second order of accuracy. While for many applications this is enough to obtain accurate results, certain applications are sensitive to continuity, and therefore require an interpolation method that does not generate artificial discontinuities. For such cases an algorithm is needed, which meets requirements of both continuity and second order of accuracy.

A particular application that motivated us to develop such algorithm is acceleration of SEPs at the shock wave fronts. The model of field-aligned transport presented in *Sokolov et al.* (2004, 2006); *Sokolov and Roussev* (2008); *Sokolov et al.* (2009) relies

heavily on magnetic field line tracing as well as interpolation of solar wind parameters from the BATS-R-US AMR grid to the locations of the magnetic field lines points. Unphysical discontinuities within the interpolation algorithm affect results by producing particle acceleration/deceleration at false shocks near grid irregularities. Hence, the model's reliability is crucially dependent on the continuity of interpolation algorithm.

The numerical results obtained with AMR are typically sampled on the cell-centered grid. A popular method, which is utilized by visualization tools, e.g. Tecplot, resamples them to corner-centered grid. However, this approach involves more distant grid cells and, as a result, smooths the data. Alternative way is to apply a simple algorithm on the uniform parts of the AMR grid directly and to create a smooth transition between parts of the grid at different resolution levels. To do so in *Weber et al.* (2001a,b); *Moran and Ellsworth* (2011), the authors developed a stitching algorithm, as described in detail in *Weber et al.* (2001a). This method achieves continuity and the second order of accuracy. Tessellation of the computational domain into simpler shapes is employed, and the interpolation procedure is fully defined by the geometry of a particular shape a given point falls into. The algorithm is fairly complicated at all the grid resolution changes and the implementation requires a major effort. The authors provide a general idea of the algorithm without particular details. When developing our algorithm, we focused on its simplicity and availability. Compared to the stitching algorithm, it is advantageous in the sense that it uses a simple interpolation procedure over a large portion of the computational domain. If one only wants to perform continuous second order accurate interpolation across simple resolution changes, our algorithm is very simple, efficient and easy to implement. Extending this algorithm to the edges and corners of the grid resolution change surfaces remains complicated.

Section A describes the general idea behind the classification used for choosing

a particular interpolation procedure, the full algorithm description is provided in section A.

A.2 Grid

Here, we focus on block-adaptive AMR grids and assume that the computational domain is decomposed into blocks, each block being a rectangular box in Cartesian (or logically Cartesian) coordinates. The blocks are decomposed into $i \times j \times k$ "cells", for three-dimensional (3D) case, the cell-per-block integer numbers (usually, even) being constant throughout the whole grid, which maintains the claimed blocks similarity. Being similar, the blocks, however, are not all identical, as long as the cell size in different blocks may differ. Specifically, we assume that in the neighboring blocks (having at least one common point on the boundary) the cell size, $\Delta x^{(C)}$, $\Delta y^{(C)}$, $\Delta z^{(C)}$, in the *coarser* (C) block may be by a factor of two larger than those in the *finer* (F) block:

$$\Delta x^{(C)} = 2\Delta x^{(F)},\ \Delta y^{(C)} = 2\Delta y^{(F)},\ \Delta z^{(C)} = 2\Delta z^{(F)}.$$

Refinement ratios more than 2 are also possible and the algorithm generalizes to these cases, but our implementation is restricted to the refinement ratio of 2.

We assume that the numerical solution of the governing equations, obtained at each time step, is a *cell-centered* grid function, e.g. the solution obtained using *control volume* method. In order to find a numerical solution at an arbitrary point within the computational domain one needs to find the way to interpolate data from the cell-centered block-adaptive AMR grid. The goal is to find the procedure to interpolate data from cell-centered block-adaptive logically Cartesian AMR grid, which continuously connects bilinear interpolation from the uniform parts of the grid through the resolution changes.

Indeed, for a uniform 2D Cartesian grid the easiest and most natural approach is a bilinear interpolation (for three dimensions it is a trilinear interpolation). It is efficient and of the second order accuracy. Another advantage is that type of inter-

polation retains symmetries with respect to the coordinate axes if they are assumed by a correspondent symmetry of the problem to be solved. Should one perform the interpolation by splitting the computational domain into a set of tetrahedra, the second order accuracy would be also achieved, however, the symmetry of the numerical solution will be broken, as long as the set of tetrahedra would not be symmetric. In addition, this partitioning is not a unique solution, thus making ambiguous the interpolation procedure. The latter may be unacceptable.

Compared to tetrahedron-based method trilinear interpolation has one important drawback: it is not continuous when directly applied near grid resolution changes. This requires us to generalize the trilinear interpolation method for these problematic sites, as we describe below.

A.3 Basic Notations

In this section we describe basic definitions and methodology. Many ideas naturally translate from lower to higher dimensions. For this reason notations have been developed in an arbitrary number of dimensions N.

For any arbitrary point $\mathbf{X}$ an algorithm solves two distinct problems: to determine an *interpolation stencil* (set of cells involved into interpolation with non-zero weights) and to calculate *interpolation weights*. An interpolation stencil should consist of cells that are close to $\mathbf{X}$. In order to elucidate "closeness" we introduce the following notions.

Enclosing stencil for point $\mathbf{X}$ (the point $\mathbf{X}$ is enclosed by this stencil) is a set of 2^N grid cell centers with their coordinate vectors, $\mathbf{x}_1, \ldots, \mathbf{x}_{2^N}$, satisfying the following two conditions:

First, the rectangular box bounded by their coordinates contains point $\mathbf{X} = (X, Y, Z)$. For example, for 2D grids cell centers in the enclosing stencils for point $\mathbf{X}$

must satisfy inequalities:

$$x_1 \leq X < x_2, \qquad y_1 \leq Y < y_3,$$
$$x_3 \leq X < x_4, \qquad y_2 \leq Y < y_4. \tag{A.1}$$

In 3D case for the first four points, $\mathbf{x}_1$, .., $\mathbf{x}_4$, the inequalities (A.1) are fulfilled together with the requirement, $z_i \leq Z$, where $i = 1, .., 4$. For the last four points, $\mathbf{x}_5$, .., $\mathbf{x}_8$, the inequalities analogous to (A.1) are fulfilled together with the requirement, $Z < z_i$, where $i = 5, .., 8$.

Second, each edge of that box does not exceed the linear size of Coarser cells, $\Delta x^{(C)}$, $\Delta y^{(C)}$, along the corresponding axis, i, e.g. for 2D grids:

$$|x_{1,3} - x_{2,4}| \leq \Delta x^{(C)},$$
$$|y_{1,2} - y_{3,4}| \leq \Delta y^{(C)}. \tag{A.2}$$

As a part of definition, we introduce notion of *Fine cluster*. Two Finer grid points of the enclosing stencil form a *2-cluster*, if they lay on a line parallel to a coordinate axis, while four Finer grid points form a *4-cluster*, if they lay on a plane parallel to a coordinate plane, etc. To reduce an ambiguity, we set an extra constraint on an enclosing stencil, by claiming that the set of conditions (A.2) should be strict inequality for stencil points, e.g. 1 and 2, if both belong to the same Fine cluster, e.g. $|x_1 - x_2| < \Delta x^{(C)}$. In this way we exclude from consideration the enclosing stencils, which unreasonably involve farther Finer grid points instead of closer ones.

Still, we emphasize that an enclosing stencil is not unique for many point locations, as illustrated in Figure A.1. For this reason it can't be identified with an interpolation stencil, which must be unambiguous. However, all stencils enclosing the same point have the same values of *edge type*. Herewith, we say that a stencil has an edge type n, $n \leq N$, if it has resolution changes in n dimensions. Within this approach,

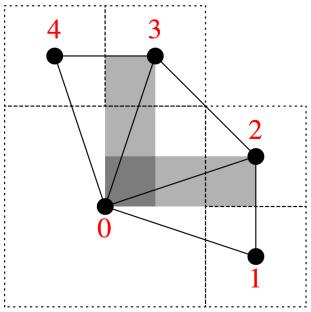

Figure A.1: Ambiguity of an enclosing stencil. All points inside the shaded rectangles are enclosed by 2 different stencils: (0,1,4,2) and (0,1,4,3) for dark gray, (0,1,3,2) and (0,1,4,2) for horizontal light gray, (0,1,4,3) and (0,2,4,3) for vertical light gray.

$(N-n)$-dimensional rectangles, which are shaped by points of a stencil parallel to the remaining dimensions, are refereed to as *trivial elements* of this stencil. Interpolation procedure on them is a simple generalization of a linear interpolation.

We refer to a set of points satisfying (A.1) for a given enclosing stencil as *an enclosed set* of this stencil. An enclosed set is an N-dimensional rectangular box. Adjacent enclosed sets of enclosing stencils of the same edge type, n, merge together into a *resolution n-edge*. Particularly, 0-edge (i.e. no resolution change) is a closed isolated domain covered by a uniform Cartesian grid. The following easy-to-prove claims are important. First, any given point can belong to one and only one resolution edge. In other words, the computational domain decomposes into a set of resolution n-edges. Second, for $n < N$, one can use simple linear interpolation in all dimensions that do not have a resolution change, i.e. on trivial elements. Thus, the effective dimensionality of non-trivial interpolation procedure for n-edge reduces to n. Indeed, this non-trivial interpolation procedure should be introduced on an n-dimensional subspace orthogonal to trivial elements.

Therefore, we define a *main interpolation subset* for point $\mathbf{X}$ inside a resolution n-edge as a cross-section of this n-edge by n-dimensional plane that includes point $\mathbf{X}$ and is perpendicular to trivial elements of enclosing stencils for the point $\mathbf{X}$. Particularly, for $n{=}N$ main interpolation subset coincides with the resolution n-edge itself. For

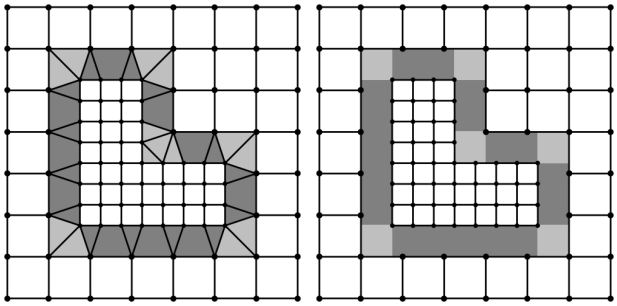

Figure A.2: Stitching (see *Weber et al.* (2001a)) and resolution edges (white - 0-edges, dark gray - 1-edges, light gray - 2-edges) on 2D grid of 4×4 adaptive blocks. Vertices are cell centers of the actual grid.

1-edge we refer to it as *main interpolation line* (see Figure A.3), for 2-edge - *main interpolation plane* (see Figure A.4).

As the last definition, an *extended interpolation stencil* for a point $\mathbf{X}$ is a minimal union of stencils enclosing together the main interpolation subset for this point. Unlike an enclosing stencil, the extended interpolation stencil is unique for any given point.

This gives us a starting point to outline the following algorithm. First, for a given point $\mathbf{X}$ we need to figure out the type of n-edge it belongs to. Based on found value of n and point location, one needs: (1) to construct the extended interpolation stencil; (2) to choose the actual interpolation stencil from the extended interpolation stencil; and (3) to calculate the interpolation weights. Then, with grid points forming the interpolation stencil for $\mathbf{X}$, indexed by $i = 1, .., m$, interpolation weights, w_i, and values of a function f sampled at grid points, f_i, the interpolated value in $\mathbf{X}$ is calculated as $f(\mathbf{X}) = \sum_{i=1}^{m} w_i f_i$. In a parallel implementation, the sum can be calculated with an `MPI_reduce` call, for example.

To conclude this section, we compare stitching algorithm *Weber et al.* (2001a) versus splitting the domain into n-edges. The left panel of Figure A.2 is based on Figure 3 of *Weber et al.* (2001a) showing a 2D AMR grid with stitch cells along edges of resolution regions (dark gray) and near their corners (light gray). On the right panel

one can see 1-edges (dark gray) and 2-edges (light gray) on the same grid. Though the images look similar, the boundaries between the light and dark gray zones are somewhat different. The stitching algorithm decomposes resolution change regions into simple shapes and performs interpolation based on them. However, throughout the 1-edge zone we apply a uniform algorithm as described below, while for the stitching algorithm two different sorts of stencils are employed. In 3D case the stitching algorithm branches further, employing three sorts of stencils for regions corresponding to a resolution 1-edge. Thus, our algorithm is easier in implementation.

A.4 Full Algorithm Description

Our goal is to develop a consistent algorithm that generalizes bilinear and trilinear interpolation to block-adaptive grids. For this reason, we apply bilinear/trilinear interpolation on uniform parts of the grids, which are 0-edges, as well as on trivial elements of extended interpolation stencils for higher order edges.

For resolution edges of types $n = 1, .., N$ on N-dimensional grid, our interpolation algorithm employs values in intersection points of the main interpolation subset with trivial elements of extended interpolation stencils. These values are calculated using linear/bilinear interpolation on $(N-n)$-dimensional trivial elements of extended interpolation stencils. Then, the interpolation scheme on resolution n-edge is solved, independently of the actual dimensionality of the grid, N, by applying the calculated interpolation weights to the values interpolated to the intersection points. Hence, the resulting interpolation weights are products of weights used to obtain the values at the intersection points and the weights resulting from interpolation procedure on a resolution n-edge.

The requirements of continuity yields an obvious relation between different types of edges: on interfaces between resolution n-edges the interpolation scheme should reduce to the algorithm used in adjacent edges of lower edge type.

As mentioned in the Introduction section, we make the code implementation of

the algorithm described in this section publicly available as a Fortran 90 library.

As outlined above, the interpolation algorithm for a given point $\mathbf{X}$ starts from determining the type of edge it belongs to and constructing the extended interpolation stencil. Practically, these two steps are combined together in the following manner. We assume in our presentation that the whole block-adaptive grid is described in terms of a "find" procedure, which for any given point coordinates returns the indices of the grid block and the grid cell containing the point as well as the cell sizes Δx, Δy, Δz, of the block and the point coordinates with respect to the block corner.

A.4.1 Construction of an Extended Stencil

Now, for the point $\mathbf{X}$ within the computational domain we first "find" the *initial* block it falls into. We note that we apply the proper nesting *Berger and Colella* (1989) restriction on the refinement levels so that grid levels of adjacent blocks (including diagonal directions) cannot differ by more than one.

If $\mathbf{X}$ happens to lay in the block interior, specifically farther than half a cell size apart from any block boundary, then it is necessarily within a uniform part of the grid formed by the block cell centers. Therefore, in order to improve the time performance, in this case a bilinear/trilinear interpolation is applied immediately and algorithm quits, returning weights and indices for the grid points of the enclosing stencil (a rectangular box $\Delta x^{(C)} \times \Delta y^{(C)} \times \Delta z^{(C)}$, the cell sizes for the *initial* block, they are marked as Coarse for the reason explained below) as the final interpolation stencil. In 2D case the weights of a bilinear interpolation, w_i^{2D}, $i = 1, .., 4$, are calculated in terms of the components (C_x, C_y) of the dimensionless coordinate vector of a given point $\mathbf{X}$ with respect to the first vertex of the enclosing stencil: $C_x = (X - x_1)/\Delta x^{(C)}$, $C_y = (Y - y_1)/\Delta y^{(C)}$. The interpolation weights of a 2D bilinear interpolation are:

$$
\begin{aligned}
w_1^{2D} &= (1 - C_x)(1 - C_y) & \qquad w_2^{2D} &= (1 - C_x)C_y \\
w_3^{2D} &= C_x(1 - C_y) & \qquad w_4^{2D} &= C_x C_y.
\end{aligned} \tag{A.3}
$$

In 3D yet another dimensionless coordinate is used, $C_z = (Z - z_1)/\Delta z^{(C)}$, and the trilinear interpolation weights are:

$$w_i^{3D} = w_i^{2D}(1 - C_z), \quad i = 1, .., 4,$$
$$w_i^{3D} = w_{i-4}^{2D} C_z, \quad i = 5, .., 8. \tag{A.4}$$

Otherwise, we extend the cell-centered grid beyond the block boundary. Now point $\mathbf{X}$ is enclosed by some rectangular box $\Delta x^{(C)} \times \Delta y^{(C)} \times \Delta z^{(C)}$ of the extended grid, but only some vertices of the box lay within the *initial* block. For the other vertices we "find" the block(s) those vertices fall into. If the newly "found" block(s) are at the same resolution level as the *initial* block, the vertices of the enclosing stencil coincide with the cell centers in these block(s) so that the indices for these blocks and cells should be included into the interpolation stencil. As above, the bilinear/trilinear interpolation is applied and the algorithm quits.

Otherwise, if any of the newly "found" block(s) is at the Finer resolution level, we need to form an extended stencil for $\mathbf{X}$ based on the coordinates of vertices of a rectangular box of size $\Delta x^{(C)} \times \Delta y^{(C)} \times \Delta z^{(C)}$ that we call the *Coarse-cell sized box* (CSB). An extended stencil includes grid points (their coordinates, cell and block ids) of the Coarser blocks, which coincide with the vertices of the CSB, as well as the Fine 2^N-clusters in the Finer blocks, the center of the cluster coinciding with the vertices of the CSB. Otherwise, if any of the newly "found" blocks is Coarser than the *initial* one, we claim this Coarser block to be *initial* and restart constructing the CSB and the extended stencil.

It is easy to see that: (1) CSB is unique for any point within the computational domain; (2) point $\mathbf{X}$ belongs to the CSB, but doesn't belong to any Fine 2^N-cluster, therefore, herewith, by CSB we mean the CSB excluding the domains enclosed by its Fine 2^N-clusters; (3) hence, the procedure above decomposes the computational

domain into CSBs and rectangular boxes; (4) union of all rectangular boxes is a union of all resolution 0-edges, while union of all CSBs is a union of all resolution edges of higher edge type; (5) the constructed set of grid points includes redundant points, but is guaranteed to include the extended stencil for any point $\mathbf{X}$ within the CSB.

Upon this stage of the algorithm, for a given point $\mathbf{X}$ we either have found it belonging to a resolution 0-edges and performed a bilinear/trilinear interpolation, or have constructed a set of grid points, which includes the extended interpolation stencil for $\mathbf{X}$.

A.4.2 Solving for Edge Type

The input for this stage of the algorithm is a set of grid points found in the previous stage and resolution levels of CSB vertices (*level sequences*). The expected output is an interpolation stencil, which is chosen from grid points of this set. It is easy to construct an enclosing stencil for the CSB *central* point, by taking all Coarser vertices of the set and selecting a single grid point from each Fine 2^N-cluster, which is the closest to the central point. Herewith, we refer to this stencil and the body it shapes as *central shape* in general or either *central quadrangle* in 2D, or *central hexahedron* in 3D. The central shape determines the upper limit for the edge type of the resolution edges present in the decomposition of the CSB, which can be derived from the sequence of the refinement levels. For example, the level sequence (the order of vertices in all sequences is defined as in Equation (A.1)) (CCCCFFFF) determines a resolution 1-edge (interface perpendicular to z-axis, see the right panel in Figure A.3), the level sequence (CFFFCFFF) determines a resolution 2-edge (edge going along z-axis, see the bottom left panel in Figure A.4). As we see, the level sequence of CSB determines not only the edge type, but also direction of trivial elements (if present) of a central shape and its orientation. We construct a lookup table for $2^{2^N}-2$ possible level sequences of CSB (excluding the 2 uniform cases), which allows us to efficiently determine the edge type and to identify the particular configuration.

A.4.3 Decomposition and Interpolation on Resolution 1-edge

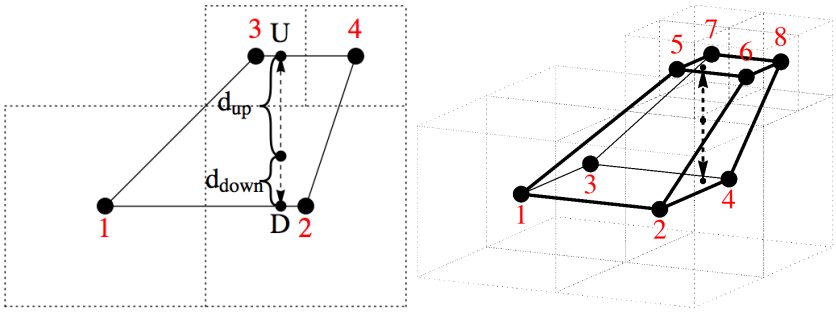

Figure A.3: Interpolation on 1-edge for 2D and 3D. Interpolation weights are calculated using distances, d_{up} and d_{down}, as: $w_{up} = d_{down}/\left(d_{down} + d_{up}\right)$, $w_{down} = 1 - w_{up}$, and are applied to the values in endpoints, U and D. These values are calculated using linear as on the left and bilinear interpolation (see equation (A.3)) on the trivial elements as on the right panel, the latter yields weights w_i^{2D}, $i = 1, .., 4$, for lower face and w_i^{2D}, $i = 5, .., 8$, for upper face, . Then the final interpolation weights are $w_i = w_i^{2D} w_{down}$, $i = 1, .., 4$, and $w_i = w_i^{2D} w_{up}$, $i = 5, .., 8$. The continuity, for example, at the boundary (1,2,3,4) between this 1-edge and 0-edge (see right panel) is ensured as our interpolation algorithm reduces to bilinear interpolation when point $\mathbf{X}$ approaches this boundary, both from below and from above. Also, as the main interpolation line crosses (2-4) edge, the weights of points 1 and 3 become zero, which ensures continuity within resolution 1-edge.

The simplest case is if the central part of the CSB, hence, the whole CSB, is a resolution 1-edge. In this case the interpolation stencil for $\mathbf{X}$, which coincides with its enclosing stencil, consists of Coarser vertices and the Fine 2^{N-1}-cluster, which $\mathbf{X}$ projects onto.

The interpolation procedure is a linear interpolation applied to endpoints of the main interpolation line, which are 2 vertices in 1D case or intersection points of the main interpolation line with trivial elements of enclosing stencil in 2D and 3D, the endpoint values are obtained using linear/bilinear interpolation on trivial elements as shown in Figure A.3. As mentioned before, we apply this simple algorithm throughout the whole resolution 1-edge. The algorithm quits.

This approach is different from that developed in *Weber et al.* (2001a), where the

authors decompose the corresponding part of a grid into two sorts of shapes in 2D and three sorts of shapes in 3D based on position of the point **X** *within* this region. In contrast, we apply the same simple interpolation procedure every time point **X** falls into a resolution 1-edge independently of its position.

A.4.4 Decomposition and Interpolation on Resolution 2-edge

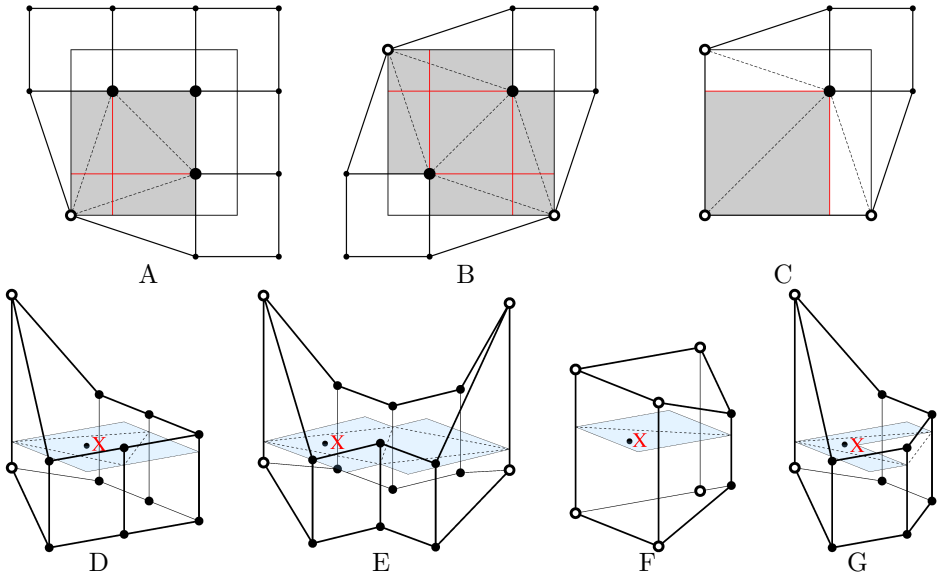

Figure A.4: CSB decomposition (top panels only) and interpolation on 2-edge for 2D (top panels) and 3D (bottom panels). Herewith, hollow points are centers of Coarser cells, solid points are those of Finer cells. Here, bolder solid points (panels A-C) mark Finer vertices of a central quadrangle. Shaded regions show main interpolation planes (which become resolution 2-edges in 2D) for point **X** (marked for 3D), white regions in top panels are resolution 0- and 1-edges. CSB decomposition is shown with red lines, being dividing lines. Triangulation of the main interpolation plane is shown with dashed lines. It is easy to see from panels A-C that interpolation on resolution 2-edges continuously transits to interpolation on resolution 0- and 1-edges through boundaries of main interpolation planes. Note, that certain triangles in the main interpolation plane only partially lay inside a resolution 2-edge with the remaining parts being inside resolution 1-edges.

If the edge type of the central shape derived from level set appears to be 2, then, generally speaking, the CSB decomposes into resolution 1- and 2-edges. Below we

provide implementation details for search for the interpolation stencil. Although not difficult for a resolution 2-edge, decomposition of a resolution 3-edge becomes very sophisticated. In order to reduce the computational time spent for the search, we split CSB into rectangular boxes. Based on which particular box the point $\mathbf{X}$ falls into, we can eliminate some of the grid points from the extended stencil and reduce the number of simple shapes that may contain point $\mathbf{X}$. We describe this procedure in details for 2-edge and only briefly we outline this for 3-edge in the next section.

Note, that the effective dimensionality in this case is 2. We consider a 2-edge in 2D (x, y) space, or a 2-edge in 3D with trivial elements along z-axis. Let $x{=}x_{min}$ be the lower face (edge) of the CSB perpendicular to x-axis, with $x{=}x_{min} + \Delta x^{(C)}{=}x_{max}$ being its upper face (edge). We divide the CSB by a plane (line), $x{=}x_{min} + \Delta x^{(C)}/4$, if the face $x{=}x_{min}$ intersects at least one Fine cluster. Analogously, we divide the CSB by a plane (line), $x{=}x_{max} - \Delta x^{(C)}/4$, if the face $x{=}x_{max}$ intersects at least one Fine cluster. Repeating the same procedure for y-axis, we split CSB into rectangular boxes (see panels A-C in Figure A.4, splitting is shown in red).

The white rectangular domains in panel C in Figure A.4 are resolution 1-edges. They are interpolated as described in section A and the algorithm quits.

The shaded boxes form the main interpolation plane for the point $\mathbf{X}$ within the resolution 2-edge. It is decomposed into triangles and we apply triangular interpolation. Once we determine, which rectangular box contains $\mathbf{X}$, only a subset of triangles needs to be checked, which makes the algorithm more efficient.

Thus, the interpolation procedure within resolution 2-edge is a triangular interpolation performed on selected vertices in 2D and on selected intersection points of the main interpolation plane with trivial elements in 3D. Again, values in these intersection points are calculated using a linear interpolation on the trivial elements. The product of weights used to calculate these values and those resulting from interpolation procedure in the main interpolation plane yields final interpolation weights.

The algorithm quits.

We note that within resolution 2-edges of a 2D grid our algorithm uses the same triangulation as *Weber et al.* (2001a), but it is connected to resolution 1-edges differently. We also describe how CSB splitting into rectangular boxes can be used to speed up the search for the interpolation stencil (triangular stencil in this case). Our approach for resolution 2-edges of a 3D grid is different from *Weber et al.* (2001a), as the authors use a 3D tessellation, while we use a linear interpolation along the trivial elements and a 2D interpolation on the main interpolation plane, which makes our algorithm simpler.

A.4.5 Decomposition and Interpolation on Resolution 3-edge

If the edge type of the central hexahedron appears to be 3, then, generally speaking, the CSB decomposes into resolution 1-, 2- and 3-edges. The approach for interpolation is similar to that applied in the previous section. Now, the dividing planes are introduced in three directions. We sort out domains, which are resolution 1- and 2-edges. Specifically, if one of the CSB faces is fully Coarse, then the rectangular box confined between this face and a Fine 4-cluster is a resolution 1-edge (see panel A of Figure A.6). Similarly, in configuration presented in panel B of Figure A.6, with one of the edges of CSB being fully Coarse, several rectangular boxes may be found, which form a domain of the resolution 2-edge with the trivial elements parallel to an isolated Coarse 2-cluster. This can be derived by analyzing the level set and decomposition of the CBS into rectangular boxes. If the point falls into a resolution 1-edge or a resolution 2-edge, the interpolation is performed as described above for such resolution edges in section A and A, respectively and the algorithm quits.

If the point $\mathbf{X}$ falls into the central box, i.e. the enclosed set of a central shape, then interpolation is performed using the tessellation shown in Figure A.5. In this case the interpolation procedure is the same as that in *Weber et al.* (2001a). The

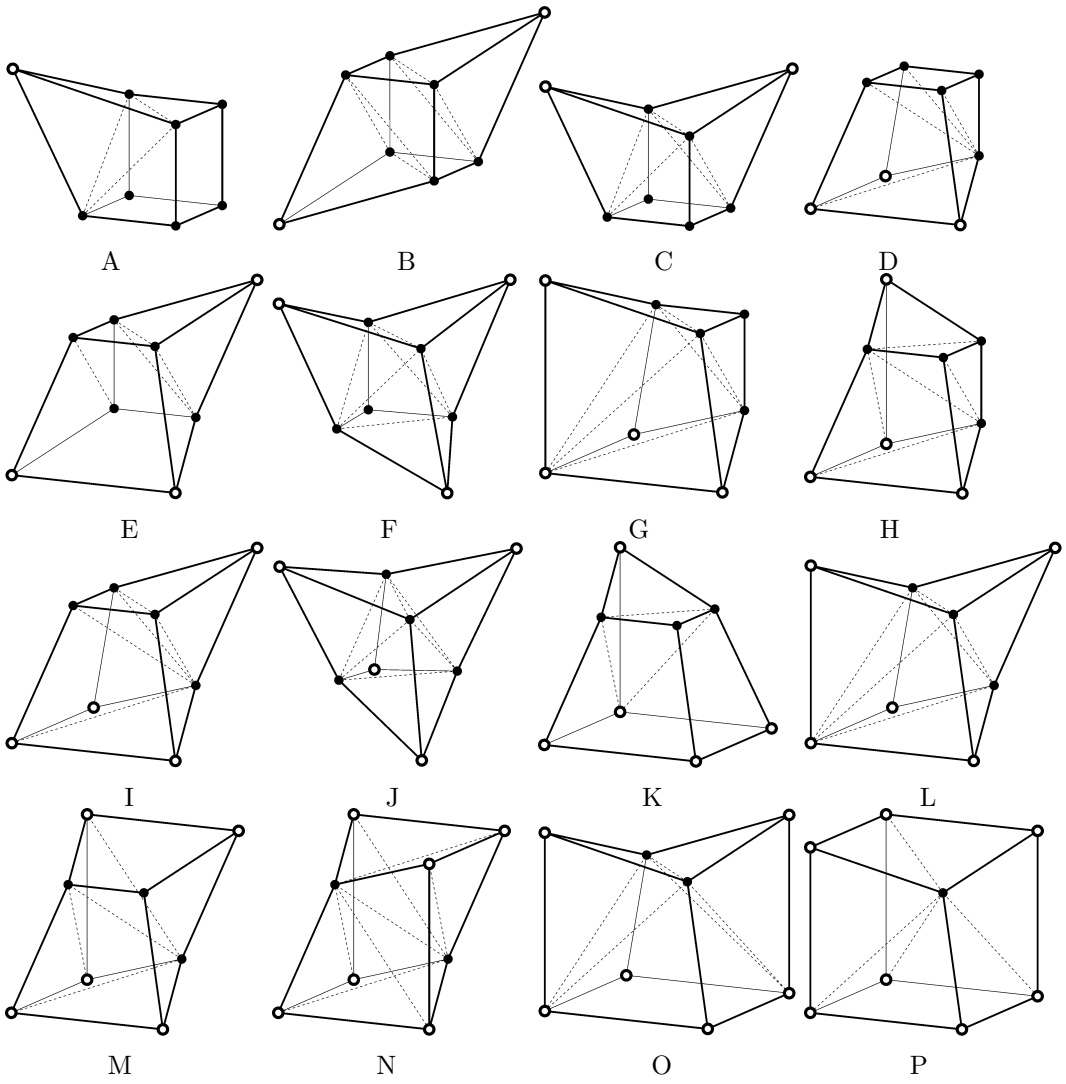

Figure A.5: Decomposition of central hexahedra of resolution 3-edges. Particular decomposition for each hexahedron is shown with dashed lines: A - tetrahedron and irregular shape; B - 2 tetrahedra and irregular shape; C - 2 tetrahedra and irregular shape; D - rectangular and 2 trapezoidal pyramids; E - tetrahedron, rectangular pyramid and wedge; F - 5 tetrahedra; G - 5 tetrahedra; H - 2 tetrahedra and 2 trapezoidal pyramids; I - 2 tetrahedra and 2 trapezoidal pyramids; J - 5 tetrahedra; K - tetrahedron and irregular shape; L - 5 tetrahedra; M - 2 tetrahedra and 2 trapezoidal pyramids; N - 6 tetrahedra; O - 2 tetrahedra and irregular shape; P - 3 rectangular pyramids.

algorithm quits.

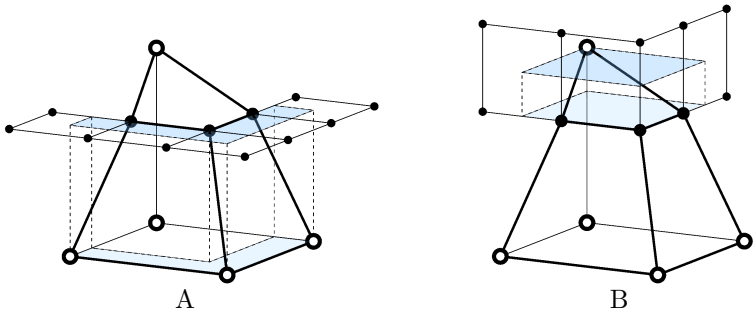

Figure A.6: An example of a CSB including resolution 1- and 2-edges. Within the CSB with central octagon K in Figure A.5 there are domains, which are: A - a resolution 1-edge; B - a resolution 2-edge. Borders of these domains are shown with dashed lines, their top and bottom faces are shaded.

Finally, for the point **X**, which doesn't fall into either the set enclosed by central hexahedron, or resolution 1- and 2-edges, the interpolation stencil is chosen according to resolution 3-edge decomposition outside the central hexahedron into simpler shapes. The interpolation is performed on the resulting shapes. The particular pattern of decomposition is based on the current CSB configuration and the position of the rectangular box **X** falls into. The idea of the decomposition procedure is given in Figure A.7.

At this point another branch in the CSB decomposition procedure is possible, as long as point **X** may happen to actually fall into the central hexahedron, rather than into the constructed shape, thus compromising the effort spent for its construction and decomposition. In this case the interpolation is performed on the central hexahedron as described in Figure A.5. The advantage of our resolution edge concept is that it allows us to avoid using whenever possible this complicated branch in the algorithm for points falling into resolution 1- and 2-edges.

We note that for resolution 3-edges our algorithm is essentially the same as the stitching algorithm, but it is connected differently to the resolution 2-edges. We also fully specify the interpolation into the various 3D shapes (*Weber et al.* (2001a) does

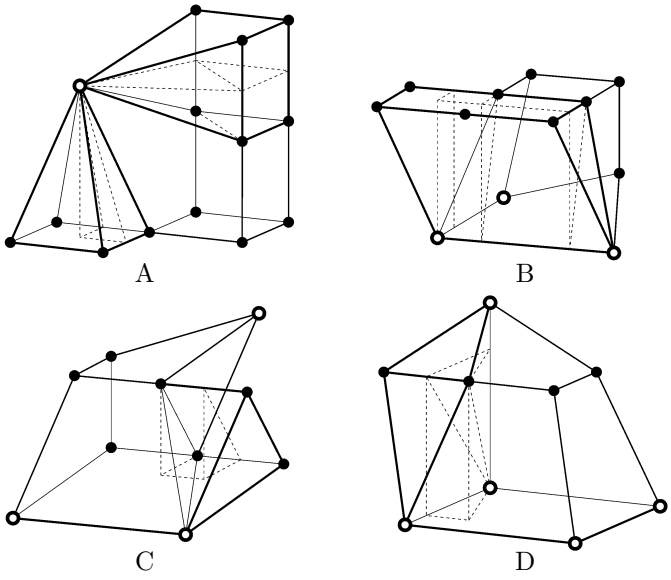

Figure A.7: Decomposition of a resolution 3-edge outside of a central hexahedron into simple shapes. Dashed lines show the boundaries of these shapes. Panel A shows an isolated Coarse vertex, see panels A, B, C, E, F, I, J and L in Figure A.5, the following shapes may be distinguished: a rectangular pyramid inside the one formed with this Coarse vertex as an apex and either a Fine 4-cluster, or a pair of Fine 2-clusters. The latter may have a triangular prism formed by 6 Fine vertices adjacent to it. Near fully Coarse edges, see panels D, E, G, H, I, K, L, M, N and O in Figure A.5, the following shapes may be distinguished: (1) a triangular prism inside a triangular wedge formed by a Coarse edge and either a Fine 4-cluster, or a pair of Fine 2-clusters (panels B and C respectively); (2) a tetrahedron inside the one formed by a Coarse edge and a Fine 2-cluster (panel D); (3) an irregular shape inside the one formed by a pair of Coarse edges and a Fine 2-cluster (panel B). Panel D shows a fully Coarse face, see panels K and O in Figure A.5, the following shapes may be distinguished: an irregular shape inside the one formed by a Coarse face and a Fine 2-cluster.

not contain this information).

A.4.6 Interpolation on Simple Shapes

The interpolation is performed on the shapes a resolution 3-edge decomposes into. In practice, the problem is solved in the following order: for a known decomposition pattern we calculate the interpolation weights for each shape involved, starting with simpler ones. The algorithm quits as soon as all the interpolation weights are positive

and less than one, i.e. the point is inside the given shape.

The simplest shape is a tetrahedron, for which there is only one second order accurate interpolation scheme. It is encountered in many possible configurations, certain central hexahedra decompose into a set of tetrahedra (see panels F, G, J, L and N in Figure A.5).

Another simple shape is a triangular wedge prism (see panels E in Figure A.5 and C, B in Figure A.7) or a triangular prism (see panel A in Figure A.7). Interpolation approach is similar to that for a resolution 2-edge. Triangular interpolation is used in the plane perpendicular to wedge's side edges, while values in intersection points are obtained using linear interpolation along these edges.

The next shape is a trapezoidal (see panels D, H, I and M in Figure A.5) or a rectangular pyramid (see panel A in Figure A.7). Interpolation is effectively a linear interpolation performed on an apex and projection of a given point along line *apex-point* onto a base. The value in a projection point is obtained using either bilinear interpolation if a given point projects onto central part of a base, or a triangular interpolation if it projects closer to trapezoid's legs.

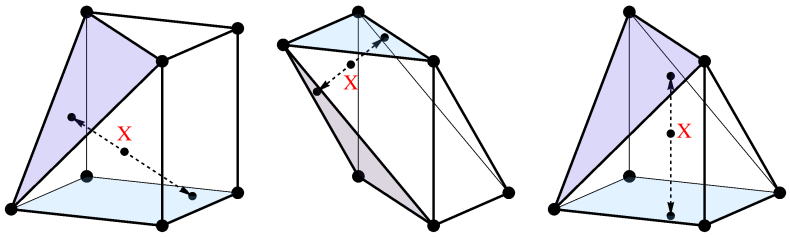

Figure A.8: An example of interpolation procedure using a ray tracing. Direction of the ray (dashed line) is chosen to be the longest diagonal of the central hexahedron for the irregular shapes in the tessellations A, B in Figure A.5 and a perpendicular to a 4-cluster for all the other irregular shapes (see panels A in Figure A.5 and B and D in Figure A.7). Shaded faces are those intersected by the ray, interpolation performed on them is either triangular, or bilinear. Linear interpolation is used along the ray to obtain a value in the point **X**.

For the remaining shapes the approach is the following. The value in a given point

X is obtained via linear interpolation on points, resulting from intersection of a ray of a certain direction going through **X** with faces of a shape. On these faces either triangular, or bilinear interpolation is used. Direction of a ray is chosen to be the longest diagonal of the central hexahedron for the irregular shapes in the tessellations A and B in Figure A.5 and perpendicular to the plane of a 4-cluster for all the other irregular shapes (see irregular shapes B and D in Figure A.7). Examples of such interpolation on irregular shapes is shown in Figure A.8.

A.5 Algorithm with Ghost Cells

Implementation of the algorithm for distributed grids deserves a closer attention. It should be noted that finding an interpolation stencil and weights is a separate problem from applying them to obtain the interpolated values. The former may be performed on any processor, provided the geometry of the grid, i.e. AMR tree needed for "find" procedure from Section A, is known everywhere, Obtaining interpolated values, however, requires access to the actual data sampled at cell centers. This requires MPI communications between processors. Of course, performing data exchanges on each call of interpolation subroutine isn't a viable option. Instead, each block in the grid stores a sufficient amount of data in its ghost cells, i.e. cells that are immediately outside the block. These cells are filled via MPI data exchanges as infrequently as possible to preserve a code's efficiency.

There are several important properties of our interpolation algorithm regarding the role of ghost cells. First, a single layer of ghost cells is sufficient to perform interpolation. This ensures applicability of the algorithm to a wider range of grids. Second, it is only possible to apply an interpolation stencil that contains cells of different resolution levels using ghost cells of a Finer block. The reason is that ghost cells of a Coarser block cover multiple Finer cells and thus aren't able to store all data necessary for interpolation. This property yields a criterion of "assigning" points to be "hosted" by blocks based on whether it is possible to complete interpolation using

ghost cells of this block. If there are several such blocks then the one that contains the point in its interior is said to host the point or, if none of candidates contains the point, the closest is chosen.

The criterion above results in a somewhat counter-intuitive situation, when the point physically resides in one, Coarser, block, but is hosted by another, Finer, block. Nevertheless, which is yet another important property, such assignment of points to host blocks results in a *unique* decomposition of the domain. This particular property plays a crucial role in the field line tracing as discussed in Chapter VI.

BIBLIOGRAPHY

BIBLIOGRAPHY

Agueda, N., D. Lario, R. Vainio, B. Sanahuja, E. Kilpua, and S. Pohjolainen (2009), Modeling solar near-relativistic electron events. Insights into solar injection and interplanetary transport conditions, *A&A*, *507*, 981–993, doi:10.1051/0004-6361/200912224.

Aguilar, M., et al. (2015), Precision measurement of the proton flux in primary cosmic rays from rigidity 1 gv to 1.8 tv with the alpha magnetic spectrometer on the international space station, *Phys. Rev. Lett.*, *114*, 171,103, doi: 10.1103/PhysRevLett.114.171103.

Alazraki, G., and P. Couturier (1971), Solar Wind Acceleration Caused by the Gradient of Alfvén Wave Pressure, *Astron. & Astrophys.*, *13*, 380.

Alfvén, H. (1942), Existence of Electromagnetic-Hydrodynamic Waves, *Nature*, *150*, 405–406, doi:10.1038/150405d0.

Antiochos, S. K., C. R. DeVore, and J. A. Klimchuk (1999), A Model for Solar Coronal Mass Ejections, *ApJ*, *510*, 485–493, doi:10.1086/306563.

Arge, C. N., and V. J. Pizzo (2000), Improvement in the prediction of solar wind conditions using near-real time solar magnetic field updates, *J. Geophys. Res.*, *105*, 10,465–10,480, doi:10.1029/1999JA000262.

Arge, C. N., D. Odstrcil, V. J. Pizzo, and L. R. Mayer (2003), Improved Method for Specifying Solar Wind Speed Near the Sun, in *Solar Wind Ten*, *American Institute of Physics Conference Series*, vol. 679, edited by M. Velli, R. Bruno, F. Malara, and B. Bucci, pp. 190–193, doi:10.1063/1.1618574.

Axford, W. I., E. Leer, and G. Skadron (1977), The acceleration of cosmic rays by shock waves, *International Cosmic Ray Conference*, *11*, 132–137.

Ball, L., and D. B. Melrose (2001), Shock Drift Acceleration of Electrons, *Publications of the Astronomical Society of Australia*, *18*, 361–373, doi:10.1071/AS01047.

Barnes, A. (1966), Collisionless Damping of Hydromagnetic Waves, *Physics of Fluids*, *9*, 1483–1495, doi:10.1063/1.1761882.

Barnes, A. (1968), Collisionless Heating of the Solar-Wind Plasma. I. Theory of the Heating of Collisionless Plasma by Hydromagnetic Waves, *ApJ*, *154*, 751, doi: 10.1086/149794.

Belcher, J. W., and L. Davis, Jr. (1971), Large-amplitude Alfvén waves in the interplanetary medium, 2, *J. Geophys. Res.*, *76*, 3534, doi:10.1029/JA076i016p03534.

Belcher, J. W., L. Davis, Jr., and E. J. Smith (1969), Large-amplitude Alfvén waves in the interplanetary medium: Mariner 5, *J. Geophys. Res.*, *74*, 2302, doi:10.1029/JA074i009p02302.

Bell, A. R. (1978a), The acceleration of cosmic rays in shock fronts. I, *MNRAS*, *182*, 147–156, doi:10.1093/mnras/182.2.147.

Bell, A. R. (1978b), The acceleration of cosmic rays in shock fronts. II, *MNRAS*, *182*, 443–455, doi:10.1093/mnras/182.3.443.

Berger, M. J., and P. Colella (1989), Local adaptive mesh refinement for shock hydrodynamics, *Journal of Computational Physics*, *82*, 64–84, doi:10.1016/0021-9991(89)90035-1.

Blandford, R. D., and J. P. Ostriker (1978), Particle acceleration by astrophysical shocks, *ApJ*, *221*, L29–L32, doi:10.1086/182658.

Boris, J. P. (1970), Relativistic plasma simulation-optimization of a hybrid code, *Proceeding of Fourth Conference on Numerical Simulations of Plasmas*.

Borovikov, D., I. V. Sokolov, and G. Tóth (2015), An efficient second-order accurate and continuous interpolation for block-adaptive grids, *J. Comput. Physics*, *297*, 599–610, doi:10.1016/j.jcp.2015.05.038.

Brueckner, G. E., et al. (1995), The Large Angle Spectroscopic Coronagraph (LASCO), *Sol. Phys.*, *162*, 357–402, doi:10.1007/BF00733434.

Cane, H. V., R. A. Mewaldt, C. M. S. Cohen, and T. T. von Rosenvinge (2006), Role of flares and shocks in determining solar energetic particle abundances, *Journal of Geophysical Research (Space Physics)*, *111*, A06S90, doi:10.1029/2005JA011071.

Cliver, E. W. (2006), The 1859 space weather event: Then and now, *Adv. Space Res.*, *38*(2), 119–129.

Cliver, E. W. (2009), History of research on solar energetic particle (SEP) events: the evolving paradigm, in *Universal Heliophysical Processes*, *IAU Symposium*, vol. 257, edited by N. Gopalswamy and D. F. Webb, pp. 401–412, doi:10.1017/S1743921309029639.

Cliver, E. W., S. W. Kahler, and D. V. Reames (2004), Coronal Shocks and Solar Energetic Proton Events, *ApJ*, *605*, 902–910, doi:10.1086/382651.

Cohen, C. M. S., R. A. Mewaldt, R. A. Leske, A. C. Cummings, E. C. Stone, M. E. Wiedenbeck, E. R. Christian, and T. T. von Rosenvinge (1999), New observations of heavy-ion-rich solar particle events from ACE, *Geophys. Res. Lett.*, *26*, 2697–2700, doi:10.1029/1999GL900560.

Cohen, C. M. S., G. M. Mason, R. A. Mewaldt, A. C. Cummings, A. W. Labrador, R. A. Leske, E. C. Stone, M. E. Wiedenbeck, and T. T. von Rosenvinge (2008), Examination of the last large solar energetic particle events of solar cycle 23, *AIP Conference Proceedings*, *1039*(1), 118–123, doi:10.1063/1.2982432.

Cohen, O., I. V. Sokolov, I. I. Roussev, and T. I. Gombosi (2008), Validation of a synoptic solar wind model, *J. Geophys. Res.*, *113*(A12), A03,104, doi:10.1029/2007JA012797.

Cohen, O., et al. (2007a), A Semiempirical Magnetohydrodynamical Model of the Solar Wind, *ApJ*, *654*, L163–L166, doi:10.1086/511154.

Cohen, O., et al. (2007b), A semiempirical magnetohydrodynamical model of the solar wind, *Astrophys. J. Lett.*, *654*, L163–L166, doi:10.1086/511154.

Coleman, P. J., Jr. (1966), Variations in the interplanetary magnetic field: Mariner 2: 1. Observed properties, *J. Geophys. Res.*, *71*, 5509–5531, doi:10.1029/JZ071i023p05509.

Coleman, P. J., Jr. (1967), Wave-like phenomena in the interplanetary plasma: Mariner 2, *Planet. Space Sci.*, *15*, 953–973, doi:10.1016/0032-0633(67)90166-3.

Coleman, P. J., Jr. (1968), Turbulence, Viscosity, and Dissipation in the Solar-Wind Plasma, *ApJ*, *153*, 371, doi:10.1086/149674.

Craig, I. J. D., and Y. E. Litvinenko (2002), Particle Acceleration Scalings Based on Exact Analytic Models for Magnetic Reconnection, *ApJ*, *570*, 387–394, doi:10.1086/339578.

Cranmer, S. R. (2010), An Efficient Approximation of the Coronal Heating Rate for use in Global Sun-Heliosphere Simulations, *ApJ*, *710*, 676–688, doi:10.1088/0004-637X/710/1/676.

Dahlin, J. T., J. F. Drake, and M. Swisdak (2014), The mechanisms of electron heating and acceleration during magnetic reconnection, *Physics of Plasmas*, *21*(9), 092304, doi:10.1063/1.4894484.

de Hoffmann, F., and E. Teller (1950), Magneto-Hydrodynamic Shocks, *Physical Review*, *80*, 692–703, doi:10.1103/PhysRev.80.692.

DeVore, C. (1991), Flux-corrected transport techniques for multidimensional compressible magnetohydrodynamics, *Journal of Computational Physics*, *92*(1), 142 – 160, doi:http://dx.doi.org/10.1016/0021-9991(91)90295-V.

Dewar, R. L. (1970), Interaction between Hydromagnetic Waves and a Time-Dependent, Inhomogeneous Medium, *Physics of Fluids*, *13*, 2710–2720, doi:10.1063/1.1692854.

Dmitruk, P., W. H. Matthaeus, L. J. Milano, S. Oughton, G. P. Zank, and D. J. Mullan (2002), Coronal Heating Distribution Due to Low-Frequency, Wave-driven Turbulence, *ApJ*, *575*, 571–577, doi:10.1086/341188.

Downs, C., I. I. Roussev, B. van der Holst, N. Lugaz, I. V. Sokolov, and T. I. Gombosi (2010), Toward a Realistic Thermodynamic Magnetohydrodynamic Model of the Global Solar Corona, *ApJ*, *712*, 1219–1231, doi:10.1088/0004-637X/712/2/1219.

Drake, J. F., M. Swisdak, H. Che, and M. A. Shay (2006a), Electron acceleration from contracting magnetic islands during reconnection, *Nature*, *443*, 553–556, doi:10.1038/nature05116.

Drake, J. F., M. Swisdak, K. M. Schoeffler, B. N. Rogers, and S. Kobayashi (2006b), Formation of secondary islands during magnetic reconnection, *Geophys. Res. Lett.*, *33*, L13105, doi:10.1029/2006GL025957.

Drake, J. F., M. Swisdak, and R. Fermo (2013), The Power-law Spectra of Energetic Particles during Multi-island Magnetic Reconnection, *ApJ*, *763*, L5, doi:10.1088/2041-8205/763/1/L5.

Earl, J. A. (1974), The diffusive idealization of charged-particle transport in random magnetic fields, *ApJ*, *193*, 231–242, doi:10.1086/153152.

Earl, J. A. (1976), The effect of adiabatic focusing upon charged-particle propagation in random magnetic fields, *ApJ*, *205*, 900–919, doi:10.1086/154346.

Egedal, J., W. Daughton, and A. Le (2012), Large-scale electron acceleration by parallel electric fields during magnetic reconnection, *Nature Physics*, *8*, 321–324, doi:10.1038/nphys2249.

Elsässer, W. M. (1950), The Hydromagnetic Equations, *Physical Review*, *79*, 183–183, doi:10.1103/PhysRev.79.183.

Evans, R. M., M. Opher, and T. I. Gombosi (2011), Learning from the Outer Heliosphere: Interplanetary Coronal Mass Ejection Sheath Flows and the Ejecta Orientation in the Lower Corona, *ApJ*, *728*, 41, doi:10.1088/0004-637X/728/1/41.

Fan, Y., and S. E. Gibson (2004), Numerical simulations of three-dimensional coronal magnetic fields resulting from the emergence of twisted magnetic flux tubes, *The Astrophysical Journal*, *609*(2), 1123.

Fermi, E. (1949), On the Origin of the Cosmic Radiation, *Physical Review*, *75*, 1169–1174, doi:10.1103/PhysRev.75.1169.

Fermo, R. L., J. F. Drake, and M. Swisdak (2010), A statistical model of magnetic islands in a current layer, *Physics of Plasmas*, *17*(1), 010702, doi:10.1063/1.3286437.

Forbes, T. G. (1986), Fast-shock formation in line-tied magnetic reconnection models of solar flares, *Astrophys. J.*, *305*, 553–563, doi:10.1086/164268.

Forbush, S. E. (1946), Three Unusual Cosmic-Ray Increases Possibly Due to Charged Particles from the Sun, *Physical Review*, *70*, 771–772, doi:10.1103/PhysRev.70.771.

Giacalone, J. (2005), The Efficient Acceleration of Thermal Protons by Perpendicular Shocks, *Ap. J. Letters*, *628*, L37–L40, doi:10.1086/432510.

Gibson, S. E., and B. C. Low (1998), A Time-Dependent Three-Dimensional Magnetohydrodynamic Model of the Coronal Mass Ejection, *Astrophys. J.*, *493*, 460–473, doi:10.1086/305107.

Ginzburg, V. L., and A. A. Rukhadze (1975), Waves in magnetoactive plasma /2nd revised edition/, *Moscow Izdatel Nauka*.

Gombosi, T. I., et al. (2004), Solution-Adaptive Magnetohydrodynamics for Space Plasmas: Sun-to-Earth Simulations, *Computing in Science and Engg.*, *6*(2), 14–35, doi:10.1109/MCISE.2004.1267603.

Gopalswamy, N., A. Lara, M. L. Kaiser, and J.-L. Bougeret (2001), Near-Sun and near-Earth manifestations of solar eruptions, *J. Geophys. Res.*, *106*, 25,261–25,278, doi:10.1029/2000JA004025.

Gopalswamy, N., H. Xie, S. Yashiro, S. Akiyama, P. Mäkelä, and I. G. Usoskin (2012), Properties of Ground Level Enhancement Events and the Associated Solar Eruptions During Solar Cycle 23, *Space Sci. Rev.*, *171*, 23–60, doi:10.1007/s11214-012-9890-4.

Gopalswamy, N., H. Xie, S. Akiyama, P. A. Mäkelä, and S. Yashiro (2014), Major solar eruptions and high-energy particle events during solar cycle 24, *Earth, Planets, and Space*, *66*, 104, doi:10.1186/1880-5981-66-104.

Gosling, J. T. (1993), The solar flare myth, *J. Geophys. Res.*, *98*, 18,937–18,950, doi:10.1029/93JA01896.

Grad, H., and H. Rubin (1958), Hydromagnetic Equilibria and Force-Free Fields, in *Proceedings of the 2nd UN Conference on the Peaceful Uses of Atomic Energy*, vol. 31, pp. 190–197.

Green, J. L., and S. Boardsen (2006), Duration and extent of the great auroral storm of 1859, *Adv. Space Res.*, *38*(2), 130–135.

Green, J. L., S. Boardsen, S. Odenwald, J. Humble, and K. A. Pazamickas (2006), Eyewitness reports of the great auroral storm of 1859, *Adv. Space Res.*, *38*(2), 145–154.

Gressl, C., A. M. Veronig, M. Temmer, D. Odstrčil, J. A. Linker, Z. Mikić, and P. Riley (2014), Comparative Study of MHD Modeling of the Background Solar Wind, *Sol. Phys.*, *289*, 1783–1801, doi:10.1007/s11207-013-0421-6.

Groth, C. P. T., D. L. De Zeeuw, T. I. Gombosi, and K. G. Powell (2000), Global three-dimensional MHD simulation of a space weather event: CME formation, interplanetary propagation, and interaction with the magnetosphere, *J. Geophys. Res.*, *105*, 25,053–25,078, doi:10.1029/2000JA900093.

Guidoni, S. E., C. R. DeVore, J. T. Karpen, and B. J. Lynch (2016), Magnetic-island Contraction and Particle Acceleration in Simulated Eruptive Solar Flares, *ApJ*, *820*, 60, doi:10.3847/0004-637X/820/1/60.

Guo, F., and J. Giacalone (2012), Particle Acceleration at a Flare Termination Shock: Effect of Large-scale Magnetic Turbulence, *ApJ*, *753*, 28, doi:10.1088/0004-637X/753/1/28.

Heath, D. F., A. J. Krueger, and P. J. Crutzen (1977), Solar proton event: influence on stratospheric ozone, *Science*, *197*(4306), 886–9.

Heinemann, M., and S. Olbert (1980), Non-WKB Alfven waves in the solar wind, *J. Geophys. Res.*, *85*, 1311–1327, doi:10.1029/JA085iA03p01311.

Hellweg, C. E., and C. Baumstark-Khan (2007), Getting ready for the manned mission to Mars: The astronauts' risk from space radiation, *Naturwissenschaften*, *94*(7), 517–526, doi:10.1007/s00114-006-0204-0.

Hollweg, J. V. (1986), Transition region, corona, and solar wind in coronal holes, *J. Geophys. Res.*, *91*, 4111–4125, doi:10.1029/JA091iA04p04111.

Holman, G. D., L. Sui, R. A. Schwartz, and A. G. Emslie (2003), Electron Bremsstrahlung Hard X-Ray Spectra, Electron Distributions, and Energetics in the 2002 July 23 Solar Flare, *ApJ*, *595*, L97–L101, doi:10.1086/378488.

Holman, G. D., M. J. Aschwanden, H. Aurass, M. Battaglia, P. C. Grigis, E. P. Kontar, W. Liu, P. Saint-Hilaire, and V. V. Zharkova (2011), Implications of X-ray Observations for Electron Acceleration and Propagation in Solar Flares, *Space Sci. Rev.*, *159*, 107–166, doi:10.1007/s11214-010-9680-9.

Hu, Y. Q., S. R. Habbal, Y. Chen, and X. Li (2003), Are coronal holes the only source of fast solar wind at solar minimum?, *Journal of Geophysical Research (Space Physics)*, *108*, 1377, doi:10.1029/2002JA009776.

Hudson, H., and J. Ryan (1995), High-Energy Particles In Solar Flares, *ARA&A*, *33*, 239–282, doi:10.1146/annurev.aa.33.090195.001323.

Ichimaru, S. (1973), *Basic principles of plasma physics, a statistical approach.*

Isenberg, P. A. (1997), A hemispherical model of anisotropic interstellar pickup ions, *J. Geophys. Res.*, *102*, 4719–4724, doi:10.1029/96JA03671.

Jackson, J. D. (1999), *Classical electrodynamics*, 3rd ed. ed., Wiley, New York, NY.

Jacobs, C., I. I. Roussev, N. Lugaz, and S. Poedts (2009), The Internal Structure of Coronal Mass Ejections: Are all Regular Magnetic Clouds Flux Ropes?, *ApJ*, *695*, L171–L175, doi:10.1088/0004-637X/695/2/L171.

Jacques, S. A. (1977), Momentum and energy transport by waves in the solar atmosphere and solar wind, *ApJ*, *215*, 942–951, doi:10.1086/155430.

Jacques, S. A. (1978), Solar wind models with Alfven waves, *ApJ*, *226*, 632–649, doi:10.1086/156647.

Jäkel, O. (2004), Radiation hazard during a manned mission to Mars, *Zeitschrift fur medizinische Physik*, *14*(4), 267–272.

Jian, L. K., P. J. MacNeice, A. Taktakishvili, D. Odstrcil, B. Jackson, H.-S. Yu, P. Riley, I. V. Sokolov, and R. M. Evans (2015), Validation for solar wind prediction at Earth: Comparison of coronal and heliospheric models installed at the CCMC, *Space Weather*, *13*, 316–338, doi:10.1002/2015SW001174.

Jin, M., W. B. Manchester, B. van der Holst, R. Oran, I. Sokolov, G. Toth, Y. Liu, X. D. Sun, and T. I. Gombosi (2013), Numerical Simulations of Coronal Mass Ejection on 2011 March 7: One-temperature and Two-temperature Model Comparison, *ApJ*, *773*, 50, doi:10.1088/0004-637X/773/1/50.

Jin, M., W. B. Manchester, B. van der Holst, I. Sokolov, G. Toth, R. E. Mullinix, A. Taktakishvili, A. Chulaki, and T. I. Gombosi (2016), Data Constrained Coronal Mass Ejections in A Global Magnetohydrodynamics Model, *ArXiv e-prints*.

Jin, M., W. B. Manchester, B. van der Holst, I. Sokolov, G. Tóth, R. E. Mullinix, A. Taktakishvili, A. Chulaki, and T. I. Gombosi (2017a), Data-constrained coronal mass ejections in a global magnetohydrodynamics model, *Astrophys. J.*, *834*(2), 173, doi:10.3847/1538-4357/834/2/173.

Jin, M., W. B. Manchester, B. van der Holst, I. Sokolov, G. Tóth, A. Vourlidas, C. A. de Koning, and T. I. Gombosi (2017b), Chromosphere to 1 AU simulation of the 2011 March 7th event: A comprehensive study of coronal mass ejection propagation, *Astrophys. J.*, *834*(2), 172, doi:10.3847/1538-4357/834/2/172.

Jokipii, J. R. (1966), Cosmic-Ray Propagation. I. Charged Particles in a Random Magnetic Field, *ApJ*, *146*, 480, doi:10.1086/148912.

Kahler, S. (1994), Injection profiles of solar energetic particles as functions of coronal mass ejection heights, *ApJ*, *428*, 837–842, doi:10.1086/174292.

Kahler, S. W., E. Hildner, and M. A. I. Van Hollebeke (1978), Prompt solar proton events and coronal mass ejections, *Sol. Phys.*, *57*, 429–443, doi:10.1007/BF00160116.

Kahler, S. W., E. W. Cliver, A. J. Tylka, and W. F. Dietrich (2012), A Comparison of Ground Level Event e/p and Fe/O Ratios with Associated Solar Flare and CME Characteristics, *Space Sci. Rev.*, *171*, 121–139, doi:10.1007/s11214-011-9768-x.

Karpen, J. T., S. K. Antiochos, and C. R. DeVore (2012), The Mechanisms for the Onset and Explosive Eruption of Coronal Mass Ejections and Eruptive Flares, *ApJ*, *760*, 81, doi:10.1088/0004-637X/760/1/81.

Kontar, E. P., et al. (2011), Deducing Electron Properties from Hard X-ray Observations, *Space Sci. Rev.*, *159*, 301–355, doi:10.1007/s11214-011-9804-x.

Kóta, J., and J. R. Jokipii (1997), Energy changes of particles moving along field line, in *Proc. 25th International Cosmic Ray Conference*, vol. 1, pp. 213–216.

Kóta, J., and J. R. Jokipii (2004), Cosmic ray acceleration and transport around the termination shock, *AIP Conference Proceedings*, *719*(1), 272–278, doi: http://dx.doi.org/10.1063/1.1809528.

Kóta, J., W. B. Manchester, J. R. Jokipii, D. L. de Zeeuw, and T. I. Gombosi (2005a), Simulation of SEP Acceleration and Transport at CME-driven Shocks, in *The Physics of Collisionless Shocks: 4th Annual IGPP International Astrophysics Conference*, *American Institute of Physics Conference Series*, vol. 781, edited by G. Li, G. P. Zank, and C. T. Russell, pp. 201–206, doi:10.1063/1.2032697.

Kóta, J., W. B. Manchester, J. R. Jokipii, D. L. de Zeeuw, and T. I. Gombosi (2005b), Simulation of sep acceleration and transport at cmedriven shocks, *AIP Conference Proceedings*, *781*, 201–206.

Kozarev, K. A., R. M. Evans, N. A. Schwadron, M. A. Dayeh, M. Opher, K. E. Korreck, and B. van der Holst (2013), Global Numerical Modeling of Energetic Proton Acceleration in a Coronal Mass Ejection Traveling through the Solar Corona, *Astrophys. J*, *778*, 43, doi:10.1088/0004-637X/778/1/43.

Krymsky, G. F. (1977), A regular mechanism for the acceleration of charged particles on the front of a shock wave, *Akademiia Nauk SSSR Doklady*, *234*, 1306–1308.

Landau, L. D., and E. M. Lifshitz (1959), *Fluid mechanics*.

Landau, L. D., and E. M. Lifshitz (1960), *Electrodynamics of continuous media*, Pergamon Press: Oxford.

Landau, L. D., and E. M. Lifshitz (1969), *Mechanics*.

Landi, E., P. R. Young, K. P. Dere, G. Del Zanna, and H. E. Mason (2013), CHIANTI - An Atomic Database for Emission Lines. XIII. Soft X-Ray Improvements and Other Changes, *ApJ*, *763*, 86, doi:10.1088/0004-637X/763/2/86.

Lee, M. A. (1982), Coupled hydromagnetic wave excitation and ion acceleration upstream of the earth's bow shock, *J. Geophys. Res.*, *87*, 5063–5080, doi: 10.1029/JA087iA07p05063.

Lee, M. A. (1983), Coupled Hydro-Magnetic Wave Excitation and Ion Acceleration at Interplanetary Traveling Shocks, *J. Geophys. Res.*, *88*, 6,109–6,119.

Lee, M. A. (1997), Particle Acceleration and Transport at CME-Driven Shocks, in Coronal Mass Ejections (eds N. Crooker, J. A. Joselyn and J. Feynman), *Washington DC American Geophysical Union Geophysical Monograph Series*, *99*, 227–234, doi:10.1029/GM099p0227.

Leroy, B. (1980), Propagation of waves in an atmosphere in the presence of a magnetic field. II - The reflection of Alfven waves, *A&A*, *91*, 136–146.

Li, G., G. P. Zank, and W. K. M. Rice (2003), Energetic Particle Acceleration and Transport at Coronal Mass Ejection-Driven Shocks, *J. Geophys. Res.*, *108(A2)*, 10–21.

Linker, J., T. Torok, C. Downs, R. Lionello, V. Titov, R. M. Caplan, Z. Mikić, and P. Riley (2016), MHD simulation of the Bastille day event, in *American Institute of Physics Conference Series*, *American Institute of Physics Conference Series*, vol. 1720, p. 020002, doi:10.1063/1.4943803.

Lionello, R., J. A. Linker, and Z. Mikić (2001), Including the Transition Region in Models of the Large-Scale Solar Corona, *ApJ*, *546*, 542–551, doi:10.1086/318254.

Lionello, R., J. A. Linker, and Z. Mikić (2009), Multispectral Emission of the Sun During the First Whole Sun Month: Magnetohydrodynamic Simulations, *ApJ*, *690*, 902–912, doi:10.1088/0004-637X/690/1/902.

Lionello, R., M. Velli, C. Downs, J. A. Linker, and Z. Mikić (2014a), Application of a Solar Wind Model Driven by Turbulence Dissipation to a 2D Magnetic Field Configuration, *ApJ*, *796*, 111, doi:10.1088/0004-637X/796/2/111.

Lionello, R., M. Velli, C. Downs, J. A. Linker, Z. Mikić, and A. Verdini (2014b), Validating a Time-dependent Turbulence-driven Model of the Solar Wind, *ApJ*, *784*, 120, doi:10.1088/0004-637X/784/2/120.

Low, B. C. (1982), Self-similar magnetohydrodynamics. I - The gamma = 4/3 polytrope and the coronal transient, *ApJ*, *254*, 796–805, doi:10.1086/159790.

Lugaz, N., W. B. Manchester, IV, and T. I. Gombosi (2005), Numerical simulation of the interaction of two coronal mass ejections from sun to earth, *Astrophys. J.*, *634*, 651–662, doi:10.1086/491782.

Lugaz, N., W. B. Manchester, IV, I. I. Roussev, G. Tóth, and T. I. Gombosi (2007a), Numerical Investigation of the Homologous Coronal Mass Ejection Events from Active Region 9236, *ApJ*, *659*, 788–800, doi:10.1086/512005.

Lugaz, N., W. B. Manchester, IV, I. I. Roussev, G. Tóth, and T. I. Gombosi (2007b), Numerical Investigation of the Homologous Coronal Mass Ejection Events from Active Region 9236, *Astrophys. J.*, *659*, 788–800, doi:10.1086/512005.

MacNeice, P. (2009), Validation of community models: 2. Development of a baseline using the Wang-Sheeley-Arge model, *Space Weather*, *7*, S12002, doi: 10.1029/2009SW000489.

Makhmutov, V., G. Bazilevskaya, Y. Stozhkov, N. Svirzhevsky, and A. Svirzhevskaya (2009), Ionisation state of the Earth's stratosphere during powerful solar proton events, in *Proc. 31st International Cosmic Ray Conference*, Łódź, Poland.

Manchester, W. B., T. I. Gombosi, I. Roussev, D. L. De Zeeuw, I. V. Sokolov, K. G. Powell, G. Tóth, and M. Opher (2004a), Three-dimensional MHD simulation of a flux rope driven CME, *J. Geophys. Res.*, *109(A18)*, 1,102–1,119, doi: 10.1029/2002JA009672.

Manchester, W. B., T. I. Gombosi, I. Roussev, A. Ridley, D. L. De Zeeuw, I. V. Sokolov, K. G. Powell, and G. Tóth (2004b), Modeling a space weather event from the Sun to the Earth: CME generation and interplanetary propagation, *J. Geophys. Res.*, *109(A18)*, 2,107–2,122, doi:10.1029/2003JA010150.

Manchester, W. B., T. I. Gombosi, D. L. De Zeeuw, I. V. Sokolov, I. I. Roussev, K. G. Powell, J. Kóta, G. Tóth, and T. H. Zurbuchen (2005), Coronal mass ejection shock and sheath structures relevant to particle acceleration, *AStrophys. J.*, *622*, 1225–1239.

Manchester, W. B., A. J. Ridley, T. I. Gombosi, and D. L. DeZeeuw (2006), Modeling the Sun-to-Earth propagation of a very fast CME, *Advances in Space Research*, *38*, 253–262, doi:10.1016/j.asr.2005.09.044.

Manchester, W. B., IV, A. Vourlidas, G. Tóth, N. Lugaz, I. I. Roussev, I. V. Sokolov, T. I. Gombosi, D. L. De Zeeuw, and M. Opher (2008), Three-dimensional MHD Simulation of the 2003 October 28 Coronal Mass Ejection: Comparison with LASCO Coronagraph Observations, *ApJ*, *684*, 1448-1460, doi:10.1086/590231.

Manchester, W. B., IV, B. van der Holst, G. Tóth, and T. I. Gombosi (2012), The Coupled Evolution of Electrons and Ions in Coronal Mass Ejection-driven shocks, *ApJ*, *756*, 81, doi:10.1088/0004-637X/756/1/81.

Manchester, W. B., IV, B. van der Holst, and B. Lavraud (2014), Flux rope evolution in interplanetary coronal mass ejections: the 13 May 2005 event, *Plasma Physics and Controlled Fusion*, *56*(6), 064006, doi:10.1088/0741-3335/56/6/064006.

Mann, G., A. Warmuth, and H. Aurass (2009), Generation of highly energetic electrons at reconnection outflow shocks during solar flares, *Astron. & Astrophys.*, *494*, 669–675, doi:10.1051/0004-6361:200810099.

Matsumoto, T., and T. K. Suzuki (2012), Connecting the Sun and the Solar Wind: The First 2.5-dimensional Self-consistent MHD Simulation under the Alfvén Wave Scenario, *ApJ*, *749*, 8, doi:10.1088/0004-637X/749/1/8.

Matthaeus, W. H., G. P. Zank, S. Oughton, D. J. Mullan, and P. Dmitruk (1999), Coronal Heating by Magnetohydrodynamic Turbulence Driven by Reflected Low-Frequency Waves, *ApJ*, *523*, L93–L96, doi:10.1086/312259.

Mays, M. L., et al. (2015), Ensemble Modeling of CMEs Using the WSA-ENLIL+Cone Model, *Sol. Phys.*, *290*, 1775–1814, doi:10.1007/s11207-015-0692-1.

Mazur, J. E., G. M. Mason, M. D. Looper, R. A. Leske, and R. A. Mewaldt (1999), Charge states of solar energetic particles using the geomagnetic cutoff technique: SAMPEX measurements in the 6 November 1997 solar particle event, *Geophys. Res. Lett.*, *26*, 173–176, doi:10.1029/1998GL900075.

Meyer, P., E. N. Parker, and J. A. Simpson (1956), Solar Cosmic Rays of February, 1956 and Their Propagation through Interplanetary Space, *Physical Review*, *104*, 768–783, doi:10.1103/PhysRev.104.768.

Michalek, G. (2006), An Asymmetric Cone Model for Halo Coronal Mass Ejections, *Sol. Phys.*, *237*, 101–118, doi:10.1007/s11207-006-0075-8.

Mikić, Z., J. Linker, R. Lionello, P. Riley, and V. Titov (2007), Predicting the structure of the solar corona for the total solar eclipse of march 29, 2006, *Solar and stellar physics through eclipses, ASP Conf. Ser.*, *370*, 299–307.

Moran, P. J., and D. Ellsworth (2011), Visualization of AMR Data With Multi-Level Dual-Mesh Interpolation., *IEEE Trans. Vis. Comput. Graph.*, *17*(12), 1862–1871.

Morris, D. (2007), *From the Flight Deck: Plane Talk and Sky Science*, ECW Press, Toronto, Ontario, Canada.

Ng, C. K., D. V. Reames, and A. J. Tylka (1999), Effect of proton-amplified waves on the evolution of solar energetic particle composition in gradual events, *Geophys. Res. Lett.*, *26*, 2145–2148, doi:10.1029/1999GL900459.

Ng, C. K., D. V. Reames, and A. J. Tylka (2003), Modeling Shock-accelerated Solar Energetic Particles Coupled to Interplanetary Alfvén Waves, *ApJ*, *591*, 461–485, doi:10.1086/375293.

Norquist, D. C., and W. C. Meeks (2010), A comparative verification of forecasts from two operational solar wind models, *Space Weather*, *8*, S12005, doi:10.1029/2010SW000598.

Northrop, T. G. (1963), Adiabatic Charged-Particle Motion, *Reviews of Geophysics and Space Physics*, *1*, 283–304, doi:10.1029/RG001i003p00283.

Oka, M., M. Fujimoto, I. Shinohara, and T. D. Phan (2010), Island surfing mechanism of electron acceleration during magnetic reconnection, *Journal of Geophysical Research (Space Physics)*, *115*, A08223, doi:10.1029/2010JA015392.

Oran, R., B. van der Holst, E. Landi, M. Jin, I. V. Sokolov, and T. I. Gombosi (2013), A Global Wave-driven Magnetohydrodynamic Solar Model with a Unified Treatment of Open and Closed Magnetic Field Topologies, *ApJ*, *778*, 176, doi: 10.1088/0004-637X/778/2/176.

Owens, M. J., H. E. Spence, S. McGregor, W. Hughes, J. M. Quinn, C. N. Arge, P. Riley, J. Linker, and D. Odstrčil (2008), Metrics for solar wind prediction models: Comparison of empirical, hybrid and physics-based schemes with 8-years of l1 observations, *Space Weather*, *6*, doi:10.1029/2007SW000380.

Parker, E. N. (1958), Dynamics of the Interplanetary Gas and Magnetic Fields., *Astroph. J.*, *128*, 664–676.

Parker, E. N. (1965), The passage of energetic charged particles through interplanetary space, *Planet. Space Sci.*, *13*, 9–49, doi:10.1016/0032-0633(65)90131-5.

Petrosian, V. (2016), Particle Acceleration in Solar Flares and Associated CME Shocks, *ApJ*, *830*, 28, doi:10.3847/0004-637X/830/1/28.

Plunkett, S. P., B. J. Thompson, R. A. Howard, D. J. Michels, O. C. St. Cyr, S. J. Tappin, R. Schwenn, and P. L. Lamy (1998), LASCO observations of an Earth-directed coronal mass ejection on May 12, 1997, *Geophys. Res. Lett.*, *25*, 2477–2480, doi:10.1029/98GL50307.

Powell, K., D. De Zeeuw, I. V. Sokolov, G. Tóth, T. Gombosi, and Q. Stout (2005), Parallel, AMR MHD for Global Space Weather Simulations, in *Adaptive Mesh Refinement - Theory and Applications*, *Lecture Notes in Computational Science and Engineering*, vol. 41, edited by T. Plewa, T. Linde, and V. Gregory Weirs, pp. 473–490, Springer Berlin Heidelberg, doi:10.1007/3-540-27039-6-36.

Powell, K. G., P. L. Roe, T. J. Linde, T. I. Gombosi, and D. L. De Zeeuw (1999), A Solution-Adaptive Upwind Scheme for Ideal Magnetohydrodynamics, *Journal of Computational Physics*, *154*, 284–309, doi:10.1006/jcph.1999.6299.

Powell, K. G., T. I. Gombosi, D. L. De Zeeuw, A. J. Ridley, I. V. Sokolov, Q. F. Stout, and G. Tóth (2003), Parallel, Adaptive-Mesh-Refinement MHD for Global Space-Weather Simulations, *AIP Conference Proceedings*, *679*(1), 807–814, doi: 10.1063/1.1618714.

Reames, D. V. (1999), Particle Acceleration at the Sun and in the Heliosphere, *Space Sci. Rev.*, *90*, 413–491.

Reames, D. V. (2002), Magnetic Topology of Impulsive and Gradual Solar Energetic Particle Events, *ApJ*, *571*, L63–L66, doi:10.1086/341149.

Reames, D. V., C. K. Ng, and D. Berdichevsky (2001), Angular Distributions of Solar Energetic Particles, *ApJ*, *550*, 1064–1074, doi:10.1086/319810.

Reiss, M. A., M. Temmer, A. M. Veronig, L. Nikolic, S. Vennerstrom, F. Schöngassner, and S. J. Hofmeister (2016), Verification of high-speed solar wind stream forecasts using operational solar wind models, *Space Weather*, *14*, 495–510, doi: 10.1002/2016SW001390.

Rice, W. K. M., G. P. Zank, and G. Li (2003), Particle acceleration and coronal mass ejection driven shocks: Shocks of arbitrary strength, *Journal of Geophysical Research (Space Physics)*, *108*, 1369, doi:10.1029/2002JA009756.

Riley, P. (2012), On the probability of occurrence of extreme space weather events, *Space Weather*, *10*, 02012, doi:10.1029/2011SW000734.

Riley, P., J. A. Linker, Z. Mikić, R. Lionello, S. A. Ledvina, and J. G. Luhmann (2006), A Comparison between Global Solar Magnetohydrodynamic and Potential Field Source Surface Model Results, *ApJ*, *653*, 1510–1516, doi:10.1086/508565.

Roussev, I. I., and I. V. Sokolov (2006), Models of Solar Eruptions: Recent Advances from Theory and Simulations, in Solar Eruptions and Energetic Particles (eds N. Gopalswamy, R. Mewaldt and J. Torsti), *Washington DC American Geophysical Union Geophysical Monograph Series*, *165*.

Roussev, I. I., T. G. Forbes, T. I. Gombosi, I. V. Sokolov, D. L. DeZeeuw, and J. Birn (2003a), A Three-dimensional Flux Rope Model for Coronal Mass Ejections Based on a Loss of Equilibrium, *ApJ*, *588*, L45–L48, doi:10.1086/375442.

Roussev, I. I., T. I. Gombosi, I. V. Sokolov, M. Velli, W. Manchester, IV, D. L. DeZeeuw, P. Liewer, G. Tóth, and J. Luhmann (2003b), A Three-dimensional Model of the Solar Wind Incorporating Solar Magnetogram Observations, *ApJ*, *595*, L57–L61, doi:10.1086/378878.

Roussev, I. I., I. V. Sokolov, T. G. Forbes, T. I. Gombosi, M. A. Lee, and J. I. Sakai (2004), A Numerical Model of a Coronal Mass Ejection: Shock Development with Implications for the Acceleration of GeV Protons, *ApJ*, *605*, L73–L76, doi: 10.1086/392504.

Roussev, I. I., N. Lugaz, and I. V. Sokolov (2007), New Physical Insight on the Changes in Magnetic Topology during Coronal Mass Ejections: Case Studies for the 2002 April 21 and August 24 Events, *ApJ*, *668*, L87–L90, doi:10.1086/522588.

Ruffolo, D. (1995), Effect of adiabatic deceleration on the focused transport of solar cosmic rays, *Astrophys. J.*, *442*, 861–874, doi:10.1086/175489.

Ruffolo, D., T. Khumlumlert, and W. Youngdee (1998), Deconvolution of interplanetary transport of solar energetic particles, *J. Geophys. Res.*, *103*, 20,591–20,602, doi:10.1029/98JA01290.

Schwadron, N. A., et al. (2010), Earth-Moon-Mars Radiation Environment Module framework, *Space Weather*, *8*, S00E02, doi:10.1029/2009SW000523.

Schwadron, N. A., et al. (2014), Synthesis of 3-D Coronal-Solar Wind Energetic Particle Acceleration Modules, *Space Weather*, *12*, 323–328, doi:10.1002/2014SW001086.

Schwadron, N. A., et al. (2015), Particle Acceleration at Low Coronal Compression Regions and Shocks, *Astrophys J.*, *810*, 97, doi:10.1088/0004-637X/810/2/97.

Sedov, L. I. (1959), *Similarity and Dimensional Methods in Mechanics*.

Shafranov, V. D. (1966), Plasma Equilibrium in a Magnetic Field, *Rev. Plasma Phys.*, *2*, 103.

Shea, M. A., and D. F. Smart (1990), A summary of major solar proton events, *Solar Physics*, *127*(2), 297–320, doi:10.1007/BF00152170.

Shea, M. A., and D. F. Smart (1994), Significant proton events of solar cycle 22 and a comparison with events of previous solar cycles, *Advances in Space Research*, *14*, 631–638, doi:10.1016/0273-1177(94)90518-5.

Shea, M. A., and D. F. Smart (2006), Compendium of the eight articles on the "Carrington Event" attributed to or written by Elias Loomis in the American Journal of Science, 1859-1861, *Adv. Space Res.*, *38*(2), 313–385.

Shea, M. A., and D. F. Smart (2012), Space Weather and the Ground-Level Solar Proton Events of the 23rd Solar Cycle, *Space Sci. Rev.*, *171*, 161–188, doi:10.1007/s11214-012-9923-z.

Shea, M. A., D. Smart, K. G. McCracken, G. A. M. Dreschhoff, and H. Spence (2006), Solar proton events for 450 years: The Carrington event in perspective, *Adv. Space Res.*, *38*(2), 232–238.

Sheeley, N. R., Jr., H. P. Warren, and Y.-M. Wang (2004), The Origin of Postflare Loops, *ApJ*, *616*, 1224–1231, doi:10.1086/425126.

Skilling, J. (1971), Cosmic Rays in the Galaxy: Convection or Diffusion?, *ApJ*, *170*, 265, doi:10.1086/151210.

Sokolov, I. V., and I. I. Roussev (2008), MHD turbulence model for global simulations of the solar wind and SEP acceleration, in *American Institute of Physics Conference Series*, *American Institute of Physics Conference Series*, vol. 1039, edited by G. Li, Q. Hu, O. Verkhoglyadova, G. P. Zank, R. P. Lin, and J. Luhmann, pp. 93–98, doi:10.1063/1.2982491.

Sokolov, I. V., I. I. Roussev, T. I. Gombosi, M. A. Lee, J. Kóta, T. G. Forbes, W. B. Manchester, and J. I. Sakai (2004), A New Field Line Advection Model for Solar Particle Acceleration, *ApJ*, *616*, L171–L174, doi:10.1086/426812.

Sokolov, I. V., I. I. Roussev, L. A. Fisk, M. A. Lee, T. I. Gombosi, and J. I. Sakai (2006), Diffusive Shock Acceleration Theory Revisited, *Astrophys. J. Lett.*, *642*, L81–L84, doi:10.1086/504406.

Sokolov, I. V., I. I. Roussev, M. Skender, T. I. Gombosi, and A. V. Usmanov (2009), Transport Equation for MHD Turbulence: Application to Particle Acceleration at Interplanetary Shocks, *ApJ*, *696*, 261–267, doi:10.1088/0004-637X/696/1/261.

Sokolov, I. V., B. van der Holst, R. Oran, C. Downs, I. I. Roussev, M. Jin, W. B. Manchester, IV, R. M. Evans, and T. I. Gombosi (2013), Magnetohydrodynamic Waves and Coronal Heating: Unifying Empirical and MHD Turbulence Models, *ApJ*, *764*, 23, doi:10.1088/0004-637X/764/1/23.

Sokolov, I. V., B. van der Holst, W. B. Manchester, D. C. S. Ozturk, J. Szente, A. Taktakishvili, G. Tóth, M. Jin, and T. I. Gombosi (2016), Threaded-Field-Lines Model for the Low Solar Corona Powered by the Alfven Wave Turbulence, *ArXiv e-prints*.

Somov, B. V., and S. A. Bogachev (2003), The Betatron Effect in Collapsing Magnetic Traps, *Astronomy Letters*, *29*, 621–628, doi:10.1134/1.1607500.

Spitzer, L., and R. Härm (1953), Transport Phenomena in a Completely Ionized Gas, *Physical Review*, *89*, 977–981, doi:10.1103/PhysRev.89.977.

Suzuki, T. K., and S.-i. Inutsuka (2005), Making the Corona and the Fast Solar Wind: A Self-consistent Simulation for the Low-Frequency Alfvén Waves from the Photosphere to 0.3 AU, *ApJ*, *632*, L49–L52, doi:10.1086/497536.

Tenishev, V., M. Combi, I. V. Sokolov, I. I. Roussev, and T. I. Gombosi (2005), Numerical Studies of the Solar Energetic Particle Transport and Acceleration, *AIAA-2005-4928*.

Tenishev, V., M. Combi, and B. Davidsson (2008), A Global Kinetic Model for Cometary Comae: The Evolution of the Coma of the Rosetta Target Comet Churyumov-Gerasimenko throughout the Mission, *ApJ*, *685*, 659-677, doi: 10.1086/590376.

Tenishev, V., M. R. Combi, B. D. Teolis, and J. H. Waite (2010), An approach to numerical simulation of the gas distribution in the atmosphere of Enceladus, *Journal of Geophysical Research (Space Physics)*, *115*, A09302, doi:10.1029/2009JA015223.

Tenishev, V., M. Rubin, O. J. Tucker, M. R. Combi, and M. Sarantos (2013), Kinetic modeling of sodium in the lunar exosphere, *Icarus*, *226*, 1538–1549, doi: 10.1016/j.icarus.2013.08.021.

Titov, V. S., and P. Démoulin (1999), Basic Topology of Twisted Magnetic Configurations in Solar Flares, *Astron. & Astrophys.*, *351*, 707–720.

Titov, V. S., Z. Mikic, J. A. Linker, and R. Lionello (2008), 1997 May 12 Coronal Mass Ejection Event. I. A Simplified Model of the Preeruptive Magnetic Structure, *ApJ*, *675*, 1614-1628, doi:10.1086/527280.

Titov, V. S., T. Török, Z. Mikic, and J. A. Linker (2014), A Method for Embedding Circular Force-free Flux Ropes in Potential Magnetic Fields, *ApJ*, *790*, 163, doi:10.1088/0004-637X/790/2/163.

Török, T., and B. Kliem (2005), Confined and Ejective Eruptions of Kink-unstable Flux Ropes, *ApJ*, *630*, L97–L100, doi:10.1086/462412.

Tóth, G., D. L. De Zeeuw, T. I. Gombosi, W. B. Manchester, A. J. Ridley, I. V. Sokolov, and I. I. Roussev (2007), Sun-to-thermosphere simulation of the 28–30 october 2003 storm with the space weather modeling framework, *Space Weather*, *5*(6), n/a–n/a, doi:10.1029/2006SW000272, s06003.

Tóth, G., et al. (2005a), A Physics-Based Software Framework for Sun-Earth Connection Modeling, in *Multiscale Coupling of Sun-Earth Processes*, edited by A. T. Y. Liu, Y. Kamide, and G. Consolini, p. 383.

Tóth, G., et al. (2005b), Space Weather Modeling Framework: A new tool for the space science community, *Journal of Geophysical Research (Space Physics)*, *110*(A9), A12226, doi:10.1029/2005JA011126.

Tóth, G., et al. (2012), Adaptive numerical algorithms in space weather modeling, *Journal of Computational Physics*, *231*, 870–903, doi:10.1016/j.jcp.2011.02.006.

Tylka, A. J. (2001), New insights on solar energetic particles from Wind and ACE, *J. Geophys. Res.*, *106*, 25,333–25,352, doi:10.1029/2000JA004028.

Tylka, A. J., D. V. Reames, and C. K. Ng (1999), Observations of systematic temporal evolution in elemental composition during gradual solar energetic particle events, *Geophys. Res. Lett.*, *26*, 2141–2144, doi:10.1029/1999GL900458.

Tylka, A. J., C. M. S. Cohen, W. F. Dietrich, M. A. Lee, C. G. Maclennan, R. A. Mewaldt, C. K. Ng, and D. V. Reames (2005), Shock Geometry, Seed Populations, and the Origin of Variable Elemental Composition at High Energies in Large Gradual Solar Particle Events, *Astrophys. J.*, *625*, 474–495, doi:10.1086/429384.

Usmanov, A. V., M. L. Goldstein, B. P. Besser, and J. M. Fritzer (2000), A global MHD solar wind model with WKB Alfvén waves: Comparison with Ulysses data, *J. Geophys. Res.*, *105*, 12,675–12,696, doi:10.1029/1999JA000233.

van der Holst, B., I. V. Sokolov, X. Meng, M. Jin, W. B. Manchester, IV, G. Tóth, and T. I. Gombosi (2014), Alfvén Wave Solar Model (AWSoM): Coronal Heating, *Astrophys J.*, *782*, 81, doi:10.1088/0004-637X/782/2/81.

Vásquez, A. M., R. A. Frazin, K. Hayashi, I. V. Sokolov, O. Cohen, W. B. Manchester, IV, and F. Kamalabadi (2008), Validation of Two MHD Models of the Solar Corona with Rotational Tomography, *ApJ*, *682*, 1328-1337, doi:10.1086/589682.

Verdini, A., and M. Velli (2007), Alfvén Waves and Turbulence in the Solar Atmosphere and Solar Wind, *ApJ*, *662*, 669–676, doi:10.1086/510710.

Verdini, A., M. Velli, W. H. Matthaeus, S. Oughton, and P. Dmitruk (2010), A Turbulence-Driven Model for Heating and Acceleration of the Fast Wind in Coronal Holes, *ApJ*, *708*, L116–L120, doi:10.1088/2041-8205/708/2/L116.

Vilmer, N., A. L. MacKinnon, and G. J. Hurford (2011), Properties of Energetic Ions in the Solar Atmosphere from γ-Ray and Neutron Observations, *Space Sci. Rev.*, *159*, 167–224, doi:10.1007/s11214-010-9728-x.

Vršnak, B., M. Temmer, T. Žic, A. Taktakishvili, M. Dumbović, C. Möstl, A. M. Veronig, M. L. Mays, and D. Odstrčil (2014), Heliospheric Propagation of Coronal Mass Ejections: Comparison of Numerical WSA-ENLIL+Cone Model and Analytical Drag-based Model, *ApJS*, *213*, 21, doi:10.1088/0067-0049/213/2/21.

Wang, Y.-M., and N. R. Sheeley, Jr. (1990), Solar wind speed and coronal flux-tube expansion, *ApJ*, *355*, 726–732, doi:10.1086/168805.

Wang, Y.-M., and N. R. Sheeley, Jr. (1992), On potential field models of the solar corona, *ApJ*, *392*, 310–319, doi:10.1086/171430.

Wang, Y.-M., and N. R. Sheeley, Jr. (1995), Solar Implications of ULYSSES Interplanetary Field Measurements, *ApJ*, *447*, L143, doi:10.1086/309578.

Weber, G., O. Kreylos, T. J. Ligocki, J. M. Shalf, H. Hagen, B. Hamann, and K. I. Joy (2001a), Extraction of crack-free isosurfaces for adaptive mesh refinement data, in *Data Visualization 2001 - Proceedings of Joint Eurographics/IEEE TCVG Symposium on Visualization*, edited by D. S. Ebert, J. M. Favre, and R. Peikert, pp. 25–34, Eurographics Association, IEEE, Springer Verlag.

Weber, G. H., O. Kreylos, T. J. Ligocki, J. M. Shalf, H. Hagen, B. Hamann, K. I. Joy, and K. liu Ma (2001b), High-quality volume rendering of adaptive mesh refinement data, in *In Proceedings of Vision, Modeling, and Visualization 2001*, pp. 121–128, Press.

White, S. M., et al. (2011), The Relationship Between Solar Radio and Hard X-ray Emission, *Space Sci. Rev.*, *159*, 225–261, doi:10.1007/s11214-010-9708-1.

Wild, J. P., S. F. Smerd, and A. A. Weiss (1963), Solar Bursts, *ARA&A*, *1*, 291, doi:10.1146/annurev.aa.01.090163.001451.

Workman, J. C., E. G. Blackman, and C. Ren (2011), Simulations reveal fast mode shocks in magnetic reconnection outflows, *Physics of Plasmas*, *18*(9), 092902, doi:10.1063/1.3631795.

Zank, G. P., W. K. M. Rice, and C. C. Wu (2000), Particle acceleration and coronal mass ejection driven shocks: A theoretical model, *J. Geophys. Res.*, *105*, 25,079–25,096, doi:10.1029/1999JA000455.

Zel'dovich, Y. B., and Y. P. Raizer (1967), *Physics of shock waves and high-temperature hydrodynamic phenomena*.

Zhao, X. P., S. P. Plunkett, and W. Liu (2002), Determination of geometrical and kinematical properties of halo coronal mass ejections using the cone model, *Journal of Geophysical Research (Space Physics)*, *107*, 1223, doi:10.1029/2001JA009143.